Structured-photon-enabled quantum-secured communication and spatio-temporal characterization of terahertz pulses

by

Jiapeng Zhao

Submitted in Partial Fulfillment of the

Requirements for the Degree

Doctor of Philosophy

Supervised by

Professor Robert W. Boyd

The Institute of Optics

Arts, Sciences and Engineering

Edmund A. Hajim School of Engineering and Applied Sciences

University of Rochester

Rochester, New York

2021

To my family and my friends, good times last forever.

Table of Contents

Biographical Sketch

Jiapeng Zhao was born in Sanmenxia, Henan, China. He finished early education in Zhengzhou No.1 high school in 2010, and started his college life in Huazhong University of Science and Technology. After graduating with a Bachelor degree in Optoelectronic Information Engineering, he started Master program in Optics at the University of Rochester in 2014. With a Master of Science degree in Optics in 2015, he started Ph.D. program in Optics at the University of Rochester under the supervision of Professor Robert W. Boyd. His research topics include in quantum communication, terahertz sensing and nonlinear optics.

Publications

The following journal publications were a result of work conducted during doctoral study:

1. Yiyu Zhou, Jiapeng Zhao, Boris Braverman, Kai Pang, Runzhou Zhang, Alan E Willner, Zhimin Shi, and Robert W Boyd. Multiprobe time reversal for high-fidelity vortex-mode-division multiplexing over a turbulent free-space link. *Physical Review Applied*, 15(3):034011, 2021

2. Yiyu Zhou, Boris Braverman, Alexander Fyffe, Runzhou Zhang, Jiapeng Zhao, Alan E Willner, Zhimin Shi, and Robert W Boyd. High-fidelity spatial mode transmission through a 1-km-long multimode fiber via vectorial time reversal. *Nature communications*, 12(1):1–7, 2021

3. **Jiapeng Zhao**, Jianming Dai, Boris Braverman, Xi-Cheng Zhang, and Robert W Boyd. Single-pixel temporal imaging. *under review, arXiv preprint arXiv:2009.13693*, 2020

4. **Jiapeng Zhao**, Yiyu Zhou, Boris Braverman, Cong Liu, Kai Pang, Nicholas K Steinhoff, Glenn A Tyler, Alan E Willner, and Robert W Boyd. Performance of real-time adaptive optics compensation in a turbulent channel with high-dimensional spatial-mode encoding. *Optics Express*, 28(10):15376–15391, 2020

5. Fumin Wang, Pei Zeng, **Jiapeng Zhao**, Boris Braverman, Yiyu Zhou, Mohammad Mirhosseini, Xiaoli Wang, Hong Gao, Fuli Li, Robert W

Boyd, et al. High-dimensional quantum key distribution based on mutually partially unbiased bases. *Physical Review A*, 101(3):032340, 2020

6. **Jiapeng Zhao**, Mohammad Mirhosseini, Boris Braverman, Yiyu Zhou, Seyed Mohammad Hashemi Rafsanjani, Yongxiong Ren, Nicholas K Steinhoff, Glenn A Tyler, Alan E Willner, and Robert W Boyd. Performance analysis of d-dimensional quantum cryptography under state-dependent diffraction. *Physical Review A*, 100(3):032319, 2019

7. **Jiapeng Zhao**, E Yiwen, Kaia Williams, Xi-Cheng Zhang, and Robert W Boyd. Spatial sampling of terahertz fields with sub-wavelength accuracy via probe-beam encoding. *Light: Science & Applications*, 8(1):1–8, 2019

8. Yiyu Zhou, Mohammad Mirhosseini, Stone Oliver, Jiapeng Zhao, Seyed Mohammad Hashemi Rafsanjani, Martin PJ Lavery, Alan E Willner, and Robert W Boyd. Using all transverse degrees of freedom in quantum communications based on a generic mode sorter. *Optics Express*, 27(7):10383–10394, 2019

9. Cong Liu, Kai Pang, Zhe Zhao, Peicheng Liao, Runzhou Zhang, Haoqian Song, Yinwen Cao, Jing Du, Long Li, Hao Song, Yongxiong Ren, Guodong Xie, Yifan Zhao, Jiapeng Zhao, Seyed M. H. Rafsanjani, Ari N. Willner, Jeffrey H. Shapiro, Robert W. Boyd, Moshe Tur, and Alan E. Willner. Single-end adaptive optics compensation for emulated

turbulence in a bi-directional 10-Mbit/s per channel free-space quantum communication link using orbital-angular-momentum encoding. *Research*, 2019:8326701, 2019

10. Cong Liu, Yongxiong Ren, **Jiapeng Zhao**, Mohammad Mirhosseini, Seyed Mohammad Hashemi Rafsanjani, Guodong Xie, Kai Pang, Haoqian Song, Zhe Zhao, Zhe Wang, et al. Switchable detector array scheme to reduce the effect of single-photon detector's deadtime in a multi-bit/photon quantum link. *Opitcs Communications*, 441:132–137, 2019

11. Yiyu Zhou, **Jiapeng Zhao**, Zhimin Shi, Seyed Mohammad Hashemi Rafsanjani, Mohammad Mirhosseini, Ziyi Zhu, Alan E Willner, and Robert W Boyd. Hermite–gaussian mode sorter. *Optics Letters*, 43(21):5263–5266, 2018

12. Dongzhi Fu, Yiyu Zhou, Rui Qi, Stone Oliver, Yunlong Wang, Seyed Mohammad Hashemi Rafsanjani, **Jiapeng Zhao**, Mohammad Mirhosseini, Zhimin Shi, Pei Zhang, et al. Realization of a scalable laguerre–gaussian mode sorter based on a robust radial mode sorter. *Optics Express*, 26(25):33057–33065, 2018

13. Kai Pang, Cong Liu, Guodong Xie, Yongxiong Ren, Zhe Zhao, Runzhou Zhang, Yinwen Cao, **Jiapeng Zhao**, Haoqian Song, Hao Song, et al. Demonstration of a 10 mbit/s quantum communication link by encoding data on two laguerre–gaussian modes with different radial indices. *Optics Letters*, 43(22):5639–5642, 2018

14. Yiyu Zhou, Mohammad Mirhosseini, Dongzhi Fu, **Jiapeng Zhao**, Seyed Mohammad Hashemi Rafsanjani, Alan E Willner, and Robert W Boyd. Sorting photons by radial quantum number. *Physical Review Letters*, 119(26):263602, 2017

15. Yongxiong Ren, Cong Liu, Kai Pang, Jiapeng Zhao, Yinwen Cao, Guodong Xie, Long Li, Peicheng Liao, Zhe Zhao, Moshe Tur, Robert W. Boyd, and Alan E. Willner. Spatially multiplexed orbital-angular-momentum-encoded single photon and classical channels in a free-space optical communication link. *Optics Letters*, 42(23):4881–4884, 2017

16. Lu Gao, Seyed Mohammad Hashemi Rafsanjani, Yiyu Zhou, Zhe Yang, Omar S Magaña-Loaiza, Mohammad Mirhosseini, **Jiapeng Zhao**, Boshen Gao, and Robert W Boyd. Distributed angular double-slit interference with pseudo-thermal light. *Applied Physics Letters*, 110(7):071107, 2017

The following conference publications were a result of work conducted during doctoral study:

1. **Jiapeng Zhao**, E Yiwen, Kaia Williams, X-C Zhang, and Robert W Boyd. Spatial sampling of terahertz fields with subwavelength accuracy via probe beam encoding. In *Terahertz, RF, Millimeter, and Submillimeter-Wave Technology and Applications XIII*, volume 11279, page 112790I. International Society for Optics and Photonics, 2020

2. **Jiapeng Zhao**, Yiyu Zhou, Boris Braverman, Cong Liu, Kai Pang, Nicholas K Steinhoff, Glenn A Tyler, Alan E Willner, and Robert Boyd.

Investigate the performance of real-time adaptive optics correction in a turbulent high-dimensional quantum communication channel. In *Free-Space Laser Communications XXXII*, volume 11272, page 112721C. International Society for Optics and Photonics, 2020

3. Yiyu Zhou, Boris Braverman, Alexander Fyffe, Runzhou Zhang, **Jiapeng Zhao**, Alan E Willner, Zhimin Shi, and Robert W Boyd. Vectorial phase conjugation for high-fidelity mode transmission through multimode fiber. In *Photonic Networks and Devices*, pages NeW2B–5. Optical Society of America, 2020

4. Cong Liu, Kai Pang, **Jiapeng Zhao**, Long Li, Yifan Zhao, Jing Du, Yongxiong Ren, Guodong Xie, Zhe Zhao, Haoqian Song, et al. Demonstration of single-end adaptive optics compensation for emulated turbulence in a bi-directional 10-mbits/s per channel free-space quantum communication link using orbital-angular-momentum encoding. In *CLEO: QELS_Fundamental Science*, pages JTh5B–2. Optical Society of America, 2018

5. Yiyu Zhou, Mohammad Mirhosseini, Dongzhi Fu, **Jiapeng Zhao**, Seyed Mohammad Hashemi Rafsanjani, Alan E Willner, and Robert W Boyd. Sorting laguerre-gaussian modes by radial quantum number. In *CLEO: Applications and Technology*, pages JTh2A–4. Optical Society of America, 2018

6. **Jiapeng Zhao**, Mohammad Mirhosseini, Yiyu Zhou, Seyed Moham-

mad Hashemi Rafsanjani, Yongxiong Ren, Nicholas K Steinhoff, Glen A Tyler, Alan E Willner, and Robert W Boyd. Performance analysis of d-dimensional quantum cryptography with mode-dependent diffraction. In *CLEO: Science and Innovations*, pages JTh2A–19. Optical Society of America, 2018

7. Kai Pang, Cong Liu, Guodong Xie, Yongxiong Ren, Zhe Zhao, Runzhou Zhang, Yinwen Cao, **Jiapeng Zhao**, Long Li, Haoqian Song, et al. Experimental demonstration of a 10-mbit/s quantum link using data encoding on orthogonal laguerre-gaussian modes. In *CLEO: QELS_Fundamental Science*, pages FTu3G–4. Optical Society of America, 2018

8. Cong Liu, Kai Pang, Hao Song, Guodong Xie, **Jiapeng Zhao**, Yongxiong Ren, Haoqian Song, Zhe Zhao, Runzhou Zhang, Long Li, et al. Experimental demonstration of a 20-mbit/s per channel free-space bi-directional quantum communication link using orbital-angular-momentum encoding and multi-port mode converters. In *CLEO: Applications and Technology*, pages JTh2A–15. Optical Society of America, 2018

9. Cong Liu, Kai Pang, Yongxiong Ren, **Jiapeng Zhao**, Guodong Xie, Yinwen Cao, Hao Song, Zhe Zhao, Haoqian Song, Long Li, et al. Demonstration of adaptive optics compensation for emulated atmospheric turbulence in a two-orbital-angular-momentum encoded free-space quantum link at 10 mbits/s. In *CLEO: QELS_Fundamental*

Science, pages FW4F–5. Optical Society of America, 2018

10. Yongxiong Ren, Cong Liu, Kai Pang, **Jiapeng Zhao**, Yinwen Cao, Guodong Xie, Long Li, Zhe Zhao, Zhe Wang, Moshe Tur, et al. Experimental demonstration of an orbital-angular-momentum encoded quantum communication link co-propagating with a classical channel. In *CLEO: Science and Innovations*, pages SW4I–4. Optical Society of America, 2017

11. Cong Liu, Yongxiong Ren, **Jiapeng Zhao**, Seyed Mohammad Hashemi Rafsanjani, Guodong Xie, Kai Pang, Haoqian Song, Zhe Zhao, Zhe Wang, Long Li, et al. Reduced effect of single-photon-detector dead-time using a switchable detector array in an orbital-angular-momentum (oam) encoded quantum system. In *CLEO: QELS_Fundamental Science*, pages FF1E–4. Optical Society of America, 2017

12. Lu Gao, **Jiapeng Zhao**, Omar S Magaña-Loaiza, Seyed Mohammad Hashemi Rafsanjani, Mohammad Mirhosseini, Yiyu Zhou, and RW Boyd. Nonlocal angular double-slit ghost diffraction with thermal light. In *Laser Science*, pages JTh2A–14. Optical Society of America, 2016

Acknowledgments

At the very beginning, I would like express my grateful appreciation to my advisor, Professor Robert W. Boyd. Doing research in Bob's group has become an indelible and unique experience in my life. Bob's passion and curiosity for physics encourage me to keep an open mind in research and comprehensively absorb knowledge from different directions. I have enjoyed my Ph.D. research life with Bob and his group of talented researchers.

I would like thank Professor Xi-Cheng Zhang for guiding me in the terahertz research through the collaboration between two groups in the past few years. I would also like to thank Professor Xi-Cheng Zhang, Professor John Nichol and Professor Qiang Lin for agreeing to serve on my committee, and for the valuable discussion and suggestions on my dissertation. I would like to appreciate the valuable collaboration with Professor Alan E. Willner at the University of Southern California, Dr. Nicholas K. Steinhoff and Dr. Glenn A. Tyler at the Optical Sciences Company, Professor Pei Zhang at Xi'an Jiaotong University, Dr. Jianming Dai at Tianjin University, as well as Dr. Zhimin Shi at Facebook Reality Lab. In addition, I would like to thank many professors who I have learned from, including Professor Miguel Alonso, Professor Carlos Stroud, Professor James Fienup, Professor John Howell, Professor Chunlei Guo, Professor Nick Vamivakas, Professor Joseph Eberly, Professor Dale Buralli, Professor Svetlana Lukishova and Professor Taco Visser.

I appreciate the help from institute staff who make my research life much easier. I would like to thank Lori Russell, Per Adamson, Maria Schnitzler, Kai Davies, Kari Kafka, Adrienne Snopkowski, Gina Kern, Meir Brea and Jim Mitchell for their generous help in the past years.

I would like to thank my talented friends and colleagues whom I learned a lot from, including Mohammad Mirhosseini, Boris Braverman, M. Zahirul Alam, Saumya Choudhary, Nick Black, Jerry Kuper, Omar S. Magana-Loaiza, Boshen Gao, Seyed Mohammad Hashemi Rafsanjani, Changchen Chen, Saumya Choudhary, Nick Black, Jerry Kuper, E. Samuel Arroyo-Rivera, Surendar Vijayakumar, Dhanush Bhatt Dinesha, Long Nguyen, Saleem Iqbal, Yiqian Gan, Zhe Yang, Shuai Sun, Fumin Wang, Dongzhi Fu, Qi Jin, Kai Williams, Kareem Jamaal Garriga Francis, Mervin Lim Pac Chong, Yuqi Cao, Steven Fu, Fang Ling, Jiacheng Zhao, Liangyu Qiu, Dan Yu, Anthony Yee, Robert Chou, Tianyi Yang, Meiting Song, Sultan Abdul Wadood, Ran Wei, Di Xu, Wenxiang Hu, Yongxiong Ren, Cong Liu, Kai Pang, and Runzhou Zhang. I especially want to appreciate Yiyu Zhou and Yang Zhao for their friendship and help during the hardest time of my Ph.D. research, as well as the generous help from Yiwen E when I firstly start working in the

THz community.

Finally, I would like to express my grateful appreciation to my parents and my fiancee Ruiting. I cannot finish this journey without their sacrifice and accompany.

Abstract

My Ph.D. research mainly focuses on two distinctive aspects of light: the secure communications enabled by the quantum nature of light, and the computational spatio-temporal characterization of terahertz pulses. In the first topic, my study aims to enhance the secure key rate in free-space quantum key distribution with orbital-angular-momentum (OAM) encoding. In the second topic, I focus on developing generic characterization methods to efficiently measure the spatio-temporal structure of terahertz (THz) pulses.

In the first chapter, we give a brief review on the Shannon information theory, principles of QKD and the development of OAM QKD in the past decade. Major challenges in this research area will be addressed as well. In the second chapter, we focus on the disclosure of optimal information carrier in OAM QKD, which aims to improve the transmission efficiency and robustness against atmospheric turbulence. In chapter three, we discuss the security loophole in OAM QKD when the dimensionality of the encoding space and communication distance are large, and provide our solution to mitigate it. In chapter four, we present our study of the mitigation of atmospheric turbulence in free-space OAM QKD through the use of adaptive optics, aiming to improve the fidelity of transmitted quantum states. Two different communication links are studied under different conditions. Based on our observation, a prototype AO system designed exclusively for OAM QKD is proposed. A summary and the outlook of free-space OAM QKD will be present in chapter five.

We turn to discuss the computational characterization of THz pulses in the remaining chapters. A brief introduction of THz techniques and the concepts of single-pixel imaging as well as compressive sensing be presented in chapter six. In the seventh chapter, we focus on the spatial measurement of THz fields. By developing the concept of probe-beam encoding, a simplified system with an improved flexibility and stability is demonstrated using computational algorithms. In chapter eight, we propose a new concept of ultrafast sensing: temporal single-pixel imaging, and demonstrate its effectiveness for both the THz and optical bands. In chapter 9, we summarize our development in THz sensing and propose a possible direction to achieve single-pixel hyperspectral imaging.

Contributors and Funding Sources

The thesis committee examining this dissertation is comprised of Professor Robert W. Boyd and Professor Xi-Cheng Zhang from the Institute of Optics, as well as Professor John Nichol from the department of Physics and Astronomy. The committee is chaired by Professor Qiang Lin from the department of Electrical and Computer Engineering at the University of Rochester. The research performed during my time as doctoral student is a result of many collaborations within Professor Boyd's research group, as well as outside of it.

My Ph.D. program is solely funded by the US Office of Naval Research (ONR).

Chapter one provides the background of the first half of the thesis and thus no original research is included.

The content of chapter two is the simulation work and has not been published in public. The work is lead by Jiapeng Zhao with the help from Dr. Glenn A. Tyler and Dr. Nicholas K. Steinhoff at the Optical Sciences Company. The research is supported by an ONR program led by Professor

Robert W. Boyd.

The content of chapter three mainly comes from the peer-reviewed publication in Physical Review A [6]. The theoretical work is led by Jiapeng Zhao with the help from Mohammad Mirhosseini, Dr. Glenn A. Tyler and Dr. Nicholas K. Steinhoff at the Optical Sciences Company. The experimental work is led by Jiapeng Zhao with the help from Yiyu Zhou. Yongxiong Ren and Cong Liu at the University of Southern California provide essential experimental suggestions. The work is supervised by Seyed Mohammad Hashemi Rafsanjani, Professor Alan E. Willner and Professor Robert W. Boyd, and is funded by one ONR program.

The content of chapter four mainly comes from the peer-reviewed publication in Optics Express [4]. The theoretical model and data analysis is led by Jiapeng Zhao with the help from Boris Braverman, Nicholas K. Steinhoff and Glenn A. Tyler. The schematic design is led by Jiapeng Zhao with suggestions from Zhimin Shi. The experimental work is led by Jiapeng Zhao with the help from Yiyu Zhou. Kai Pang and Cong Liu at the University of Southern California provide essential experimental suggestions. The work is supervised by Professor Alan E. Willner and Professor Robert W. Boyd, and is funded by one ONR program.

The content of chapter five is the summary of previous three chapters.

The content of chapter six is the background review of the second half of this dissertation.

The content of chapter seven comes from the peer-reviewed publication in

Light: Science and Applications [7]. The theoretical model and data analysis is led by Jiapeng Zhao with the help from Yiwen E. The experimental work is led by Jiapeng Zhao with the help from Yiwen E and Kai Williams. The work is supervised by Professor Xi-Cheng Zhang and Professor Robert W. Boyd, and is funded by one ONR program.

The content of chapter eight comes from the publication which is still under review [3]. The theoretical model and data analysis is led by Jiapeng Zhao with the help from Boris Braverman. The experimental work is led by Jiapeng Zhao with the help from Jianming Dai. The work is supervised by Professor Xi-Cheng Zhang and Professor Robert W. Boyd, and is funded by one ONR program.

List of Tables

List of Figures

Chapter 1

Introduction to high-dimensional OAM quantum communication

1.1 Orbital angular momentum states

The relation between spin angular momentum and polarization has been studied for more than one hundred years [29]. As a comparison, it was not clear that how orbital angular momentum (OAM) is related to the light field until the breakthrough work done by Allen *et al.* in 1992. They explicitly showed that a light field with an azimuthal phase structure of $\exp(i\ell\theta)$, for example Laguerre-Gaussian (LG) modes, carries $\ell\hbar$ units of OAM, where θ is the azimuthal coordinate and ℓ is an integer denoting the OAM quantum number. Due to the phase singularity on the optical axis, this distinctive azimuthal phase structure also leads to a topological charge equal to ℓ [30]. Therefore, OAM states, the light fields carrying OAM, are sometime known as vortex states. The possible applications of OAM states have been studied in both classical and quantum regimes for years [15, 16, 31, 32, 33, 34, 35, 36, 37, 38, 39, 40, 41, 42, 43, 44]. Before we start discussing the applications of OAM states in quantum key distribution, it is convenient to introduce some basic properties of OAM states.

Under the paraxial approximation, a generic classical description of a scalar light field $u(r, \theta, z)$ carrying OAM can be written in the following form:

$$u(r, \theta, z) = A(r, z) \exp(i\ell\theta) \exp(i\phi(r, z)), \tag{1.1}$$

where r is the radial coordinate and z is the longitudinal coordinate. $A(r, z)$ is the slowly varying amplitude distribution of the light field with rotational symmetry, and $\exp(i\phi(r, z))$ represents the radial and longitudinal phase. One can easily verify the orthogonality of these OAM carriers by calculating the inner product of two light fields $u_1(r, \theta, z)$ and $u_2(r, \theta, z)$:

$$\begin{aligned}
&\langle u_1(r, \theta, z), u_2(r, \theta, z)\rangle \\
&\qquad = \int_0^\infty \int_0^{2\pi} u_1^*(r, \theta, z) u_2(r, \theta, z) dr d\theta \\
&\qquad = \int_0^\infty \int_0^{2\pi} A_1^*(r, z) \exp(i\ell_1\theta) \exp(-i\phi_1(r, z)) \times \\
&\qquad\quad A_2(r, z) \exp(-i\ell_2\theta) \exp(i\phi_2(r, z)) dr d\theta \\
&\qquad = \delta_{\ell_1\ell_2},
\end{aligned} \tag{1.2}$$

where $\delta_{\ell_1\ell_2}$ is the Kronecker delta. Therefore, OAM states are inherently orthogonal regardless of the amplitude distribution $A(r, z)$ and the phase structure $\exp(i\phi(r, z))$. Hence, different choices of $A(r, z)$ and $\exp(i\phi(r, z))$

will yield various sets of modes carrying OAM, which will be discussed in details in chapter 2.

1.2 Shannon information theory

Due to the internal orthogonality of OAM carriers, these vortex states naturally span an infinitely large Hilbert space, which is ideal for information encoding. To clearly illustrate how to use OAM states to encode information, we firstly start with a brief introduction of basic concepts in Shannon information theory and quantum cryptography.

Modern information theory was formally established by Claude Shannon in his paper "A mathematical theory of communication" [45]. A generic communication system consists of three parts: the transmitter (traditionally named Alice), a physical channel which the information is transmitted, and the receiver (traditionally named Bob). An eavesdropper who tries to attack the communication system and steal information is also assumed with a code name Eve. A simple schematic of this communication system is shown in Figure 1.1.

To perform a successful communication, Alice has to first encode information onto a physical particle. This process is endowing symbols with abstract meanings which have been preassigned. A natural and concrete example is language. People use characters, sounds and tones as symbols to represent different meaning in information exchanging scenarios such as conversations

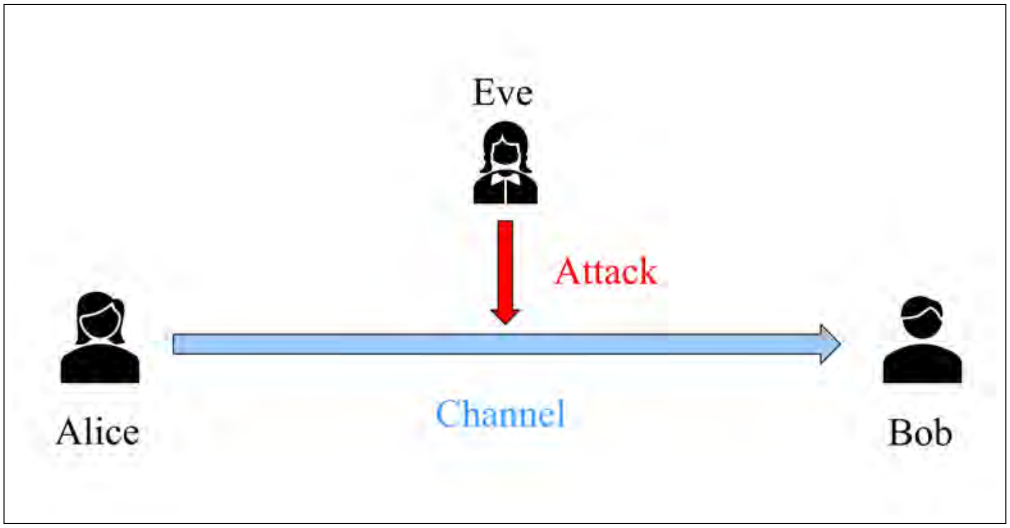

Figure 1.1: Schematic of a typical communication system proposed by Shannon.

and letters. In the communication system proposed by Shannon, Alice and Bob select a list of symbols to use and assign different meanings to each symbol. As an analog of language, this list is called the alphabet X. If we define the probability of finding a specific symbol $x \in X$ in a particle encoded by X is $p(x)$, the Shannon information $H(X)$ carried by this particle is:

$$H(X) = \sum p(x)\log_b(1/p(x)) = -\sum p(x)\log_b(p(x)), \tag{1.3}$$

where b is the base of logarithmic function and determined by the unit of the information. For example, we choose $b = 2$ when we measure the information in bits. It is worth noting that the Shannon information $H(X)$ is also known as Shannon entropy due to the analogy to the entropy in thermodynamics. If all N symbols have the same probability $p(x) = 1/N$, Eq. (1.3) will reduce to a much simplified form:

$$H(X) = \sum p(x)\log_b(1/p(x)) = \log_2(N). \tag{1.4}$$

Here we have taken $b = 2$ to quantify the information in bits.

With Eq. (1.3), if we assume the alphabet used by Alice is A, we can quantify the information encoded on a particle by Alice as $H(A)$. However, the amount of information that Bob can measure $H(B)$ would not be identical to $H(A)$ unless the channel and measurement are ideal, i.e. the channel and measurement are free of loss and error. Note that the loss and error can be either induced by Eve or by the imperfect system. If the carrier is lost, $H(B)$ will be null since no physical particle is successfully transmitted. If the error exists either in encoding, transmission or decoding phase, the desired information will be misrepresented. For simplicity, we assume that Alice prepares a symbol a where $a \in A$, and Bob measures a symbol b where $b \in B$. Based on Eq. (1.3), the information obtained by Bob from his measurement can be quantified as:

$$H(B|A = a) = -\sum_b p(b|a)\log_2(p(b|a)), \tag{1.5}$$

where $p(b|a)$ is the conditional probability. Then the average or expected information obtained by Bob can be found as:

$$H(B|A) = \sum_a H(B|A=a) = -\sum_{a,b} p(a)p(b|a)\log_2(p(b|a)). \tag{1.6}$$

When $b \neq a$, $H(B|A)$ denotes the error information which should be eliminated. Therefore, the mutual information, or more specifically Shannon mutual information, shared by Alice and Bob per particle after the communication is defined as the difference between the ideal information obtained by Bob and the error information:

$$\begin{aligned} I_{A,B} &\equiv H(B) - H(B|A) \\ &= -\sum p(b)\log_2(p(b)) + \sum_{a,b} p(a)p(b|a)\log_2(p(b|a)). \end{aligned} \tag{1.7}$$

In real experiments, $p(b)$ is usually unknown and $p(b|a)$ is directly measured. Considering the preknowledge of $p(a)$, it is always convenient to replace $p(b)$ with the relation:

$$p(b) = \sum_a p(b|a)p(a). \tag{1.8}$$

Thus, we can find the relation between mutual information $I_{A,B}$ and measurable conditional probability $p(b|a)$ by substituting Eq. (1.8) into Eq. (1.7):

$$\begin{aligned}
I_{A,B} &= -\sum p(b)\log_2(p(b)) + \sum_{a,b} p(a)p(b|a)\log_2(p(b|a)) \\
&= -\sum_{a,b} p(b|a)p(a)\log_2(\sum_{a_1} p(b|a_1)p(a_1)) + \\
&\sum_{a,b} p(a)p(b|a)\log_2(p(b|a)) \\
&= \sum_{a,b} p(a)p(b|a)\log_2(\frac{p(b|a)}{\sum_{a_1} p(b|a_1)p(a_1)})
\end{aligned} \tag{1.9}$$

Again, if the system is free from error and loss, Eq. (1.9) can be reduced to Eq. (1.4). Note that, even though Shannon mutual information is considered 'classical', the quantum mutual information, i.e. the von Neumann information, will be the same as Shannon mutual information when the density matrix under study is decomposed into its eigenstates.

In a generic communication scenario, the error rate for each symbol, i.e. $p(b|a)$ for each $\{a, b\} \in \{A, B\}$, is not of our interest, and hence we can simply use error rate Q denoting the total error rate for all misrepresented symbols. As a natural consequence, it is also convenient to define fidelity F, which denotes the probability that the measured symbol is identical to the prepared one, as:

$$F \equiv 1 - Q. \tag{1.10}$$

Assuming that no symbol-dependent error and loss are present, we can simplify Eq. (1.9) by substituting Q into it:

$$
\begin{aligned}
I_{A,B} &= \sum_{a,b} p(a)p(b|a)\log_2\left(\frac{p(b|a)}{\sum_{a_1} p(b|a_1)p(a_1)}\right) \\
&= \log_2 N + Q\log_2\frac{Q}{N-1} + (1-Q)\log_2(1-Q) \\
&= H(B) - H(Q),
\end{aligned}
\tag{1.11}
$$

where $H(Q)$ is the Shannon entropy of error rate Q. Eq. (11) is a more widely used equation than Eq. (1.9), and we will use it in the following chapters to calculate the secure information in quantum cryptography. It is worth addressing, once more, that Eq. (11) is only valid on the condition that symbol-dependent error and loss can be ignored. In the third chapter, we will show that this condition does not hold for OAM-based quantum cryptography in a realistic channel when the encoding dimensionality is large and the communication distance is long.

1.3 Quantum key distribution

As depicted in Fig. 1.1, the communication channel can be attacked by an eavesdropper Eve, and as a consequence, one challenge in classical communication is protecting the information against eavesdropping. The standard approach is encrypting the information with a set of secure, unique but random keys shared only between Alice and Bob. By implementing this method, the information transmitted in the channel becomes meaningless to Eve unless she can decrypt these symbols with correct keys. Thus, the security in the communication relies on the generation of secure keys. In the traditional communication, the security of keys relies on the computational complexity, which is simple to understand: the longer the key is, it is harder for Eve to decipher. In the past century, this strategy worked well until the concept of quantum computing being announced by Richard Feynman in 1982 [46]. Deciphering a long string of keys, which can take a unreasonably long time on a classical computer, becomes unchallenging to a quantum computer due to the superposition nature of quantum states. Hence, the traditional encryption strategy will provide no protection to communication systems in the future. Luckily, along with the birth of quantum computer, quantum cryptography comes into the sight of public. Quantum key distribution (QKD) is considered to be one of the most promising and practical applications of quantum cryptography [47, 48, 49]. It uses the quantum nature of light to distribute secure keys between Alice and Bob, which would be used to further encrypt desired information for communication purpose.

1.3.1 Difference between classical information and quantum information

In classical communication, a particle, i.e. a photon in optical communication, is only encoded with one symbol. For simplicity, we assign bit 0 to the photon in state $|0\rangle$ and bit 1 to the photon in state $|1\rangle$. Both states are orthogonal and presented in Dirac notation. Thus, one single measurement can determine the state of this photon, either in state $|0\rangle$ or $|1\rangle$.

However, in quantum world, we can prepare the photon in a superposition state of the two:

$$|\phi\rangle = c_1 |0\rangle + c_2 |1\rangle , \tag{1.12}$$

where c_1 and c_2 are normalized complex coefficients satisfying the relation: $|c_1|^2 + |c_2|^2 = 1$. $|\phi\rangle$ represents a quantum bit in quantum information theory, which is usually known as qubit. These qubits carry richer information than classical bits, which can be revealed only if the appropriate quantum measurement strategy is chosen.

When Bob follow the same strategy as in the classical communication, i.e. measures such a qubit using either $|0\rangle$ or $|1\rangle$, he cannot reveal the full information encoded on this photon. His outcomes would be probabilistic with a probability $|c_1|^2$ of finding $|0\rangle$ and a probability $|c_2|^2$ of finding $|1\rangle$, and the phase information has lost. We will rigorously show this as below.

This measurement procedure, i.e. projecting the unknown state onto basis states, is called projective measurement. The rigorous description of projective measurement starts with a projective operator $\hat{P}$:

$$\hat{P} = \sum_{n}^{N} \lambda_n |\psi_n\rangle \langle\psi_n| , \tag{1.13}$$

where λ_n is the eigenvalue and $|\psi_n\rangle$ are orthogonal eigenstates forming a N-dimensional Hilbert space. In the example given above, $|\psi_n\rangle$ are $|0\rangle$ and $|1\rangle$. The operator $|\psi_n\rangle \langle\psi_n|$ is called projector $\hat{p}$, which projects the measurable state onto the basis state. Hence, the expectation value of projecting the state $|\phi\rangle$ onto state $|0\rangle$ can be found as:

$$p(0) = \mathrm{Tr}(\hat{\rho}\hat{p}_0) = \sum_{n=0,1} \langle n|\phi\rangle \langle \phi|0\rangle \langle 0|n\rangle = |c_1|^2, \tag{1.14}$$

where $\hat{\rho}$ is the density matrix and Tr represents trace operation. Since the trace of a matrix is invariant under unitary transformation, the resulting expression is independent of the basis choice.

The projective measurement mentioned above is in principle identical to classical measurement: project one unknown state onto orthogonal basis states $|0\rangle$ or $|1\rangle$. The problem is obvious if we expand $\hat{\rho}$:

$$\begin{aligned} \hat{\rho} &= |\phi\rangle \langle\phi| \\ &= |c_1|^2 |0\rangle \langle 0| + c_1^* c_2 |1\rangle \langle 0| + c_1 c_2^* |0\rangle \langle 1| + |c_2|^2 |1\rangle \langle 1| . \end{aligned} \tag{1.15}$$

Since each projector is Hermitian, one cannot distinguish $\hat{\rho}$ from a mixed state $\hat{\rho}_m$:

$$\hat{\rho}_m = |c_1|^2 |0\rangle \langle 0| + |c_2|^2 |1\rangle \langle 1| . \tag{1.16}$$

Thus, the coherence in the quantum state $\hat{\rho}$ cannot be measured by these classical-like projective measurement strategy, leading to the loss of information.

If $|c_1|^2 = |c_2|^2$, Bob can project his state $|\phi\rangle$ onto the orthogonal basis:

$$|\phi_\pm\rangle = c_1 |0\rangle \pm c_2 |1\rangle). \tag{1.17}$$

By following the calculation shown in Eq. (1.14), we can find that $p(|\phi_+\rangle) = 1$ and $p(|\phi_-\rangle) = 0$. Thus, this measurement can directly identify $|\phi\rangle$ without losing any information.

Instead, for a generic case where $|c_1|^2 \neq |c_2|^2$, we can still measure the phase information by projecting the state $|\phi\rangle$ onto other sets of orthogonal basis. Here are two examples:

$$|\phi_\pm\rangle = \frac{1}{\sqrt{2}}(|0\rangle \pm |1\rangle), \tag{1.18}$$

$$|\psi_\pm\rangle = \frac{1}{\sqrt{2}}(|0\rangle \pm i\,|1\rangle). \tag{1.19}$$

Following the trace calculation in Eq.(1.14), we can find:

$$p(|\phi_\pm\rangle) = \mathrm{Tr}(\hat{\rho}\hat{p}_{|\phi_\pm\rangle}) = \frac{1}{2} \pm \mathrm{Re}[c_1 c_2^*] \tag{1.20}$$

$$p(|\psi_\pm\rangle) = \mathrm{Tr}(\hat{\rho}\hat{p}_{|\psi_\pm\rangle}) = \frac{1}{2} \pm \mathrm{Im}[c_1 c_2^*] \tag{1.21}$$

Thus, one can find the real and imaginary part of $c_1 c_2^*$ from the calculation above. In general, by projecting the state $|\phi\rangle$ onto the superposition state of $|0\rangle$ and $|1\rangle$, we can extract more information than the classical strategy.

	H/V basis		D/A basis	
symbol	0	1	0	1
state	$\|H\rangle$	$\|V\rangle$	$\|D\rangle$	$\|A\rangle$

Table 1.1: Encoding binary symbols on polarization states following BB84 protocol.

1.3.2 Basic concepts of QKD and mutually unbiased bases

QKD was firstly proposed by Bennett and Brassard in 1984, and their protocol is named as BB84 [50]. For simplicity, only the BB84 protocol will be discussed in this dissertation. In this scheme, Alice assigns symbols to several sets (at least two) of orthogonal basis which are mutually unbiased. She randomly choose one basis to encode her photons and then transmit the prepared photons to Bob. At the receiver side, Bob also randomly choose his measurement basis to measure those photons. Once these two legitimate parties have a long string of measurement results, they announce their choice of bases of each measurement and discard those events where the measurement bases are not identical to the prepared bases. After this sifting process, Alice and Bob will announce one section of their sifted key to estimate the error rate. This error rate will be used to perform error correction and privacy amplification to get the final secure keys.

One simple example of using polarization encoding is shown in table 1. The definition of $|D\rangle$ and $|A\rangle$ states, in terms of $|H\rangle$ and $|V\rangle$ states, are:

$$|D\rangle = \frac{1}{\sqrt{2}}(|H\rangle + |V\rangle), \tag{1.22}$$

$$|A\rangle = \frac{1}{\sqrt{2}}(|H\rangle - |V\rangle). \tag{1.23}$$

Thus, we can find that the square of the magnitude of the inner product between any state in H/V basis and any state in D/A basis is 1/2. Since the inner product is independent of choice of states, we call these two bases are mutually unbiased bases (MUBs).

The security of QKD relies on the use of MUBs due to the non-cloning nature of single photons [51]. When Eve intercepts a photon sent by Alice, she can either prepare a new one based on her measurement result and sent it to Bob, or just transmit it. Obviously only the former choice can acquire information. However, when Eve measures this photon, she has to randomly choose her basis due to the lack of preknowledge of Alice's basis choice. Once the wrong basis is selected, as we discussed in section 1.3.1, her projective measurement will degrade to a classical-like measurement strategy. In this case, with a 50% probability as shown above, her measurement will inevitably project the photon onto a state in the other basis. For example, if she measure a photon in $|H\rangle$ using D/A basis, she will project that photon either in $|D\rangle$ or $|A\rangle$ with the same probability equal to 50%. Therefore, as we have shown before, Eve's measurement will result in the loss of information so that she cannot get access to the full information prepared by Alice. In additional, when she sends a new photon based on her measurement result to Bob, her action will lead to an additional error at Bob's side. Once the error exceeding the upper bound of the error rate, this abnormal error rate will be found by Alice and Bob in the error estimation phase, which reveals the existence of Eve. If Eve only measures a small portion of photons, the error rate can be lower than the error rate threshold. But that part of information will also be erased out by Alice and Bob in error correction and privacy amplification phases. Thus, Eve's attack either gets no information shared by Alice and Bob, or exposes the existence of her attack.

1.3.3 Secure key rate and error threshold for a d-dimensional QKD system

In the example discussed in the last section, we only show the simplest QKD system with a 2-dimensional encoding Hilbert space, i.e. binary encoding. In real applications, a high dimensional encoding system with a d-dimensional encoding Hilbert space is more favorable, and we will show its advantages in this section.

The most important parameter in QKD is the secure key rate, which is defined as the secure information shared by Alice and Bob per second [52]:

$$r \propto \eta \mu r_{\infty}, \tag{1.24}$$

where η is transmission efficiency of the communication link and μ is the photon rate. r_∞ stands for the secret key fraction for an infinitely-long key, which indicates the amount of secure information encoded per photon. It is worth noting that for a high-dimensional QKD system with $d > 2$, one can use at most $d-1$ MUBs to provide more protection. However, since the improvement is relatively subtle and finding a set of $d-1$ MUBs for an arbitrary d is still under research, we only discuss the 2-MUBs QKD in this dissertation. In the 2-MUBs case, r_∞ can be found as [53, 54]:

$$r_\infty = H(B) - H(Q) - H_E(Q), \tag{1.25}$$

where $H(B) - H(Q)$ is just Eq. (1.11) with $N = d$. $H_E(Q)$ denotes the potential information leaked to Eve based on the error rate induced by her attack. Thus, the critical part in security analysis is finding the upper limit of $H_E(Q)$. To guarantee the security, we have to contribute all errors to Eve's attack, leading to an expression of $H_E(Q)$[53, 54]:

$$H_E(Q) = -Q\log_2\frac{Q}{d-1} - (1-Q)\log_2(1-Q), \tag{1.26}$$

which is the same as the information induced by pure error $H(Q)$. By substituting Eq. (1.11) and Eq. (1.26) into Eq. (1.25), we can find the final form of secure key fraction of a d-dimensional QKD system [48, 49, 53, 54, 55]:

$$\begin{aligned} r_\infty &= H(B) - H(Q) - H_E(Q) \\ &= \log_2 d + 2[Q\log_2\frac{Q}{d-1} + (1-Q)\log_2(1-Q)]. \end{aligned} \tag{1.27}$$

d	2	3	4	5	7	11
Q_{max}	11.00%	15.95%	18.93%	20.99 %	23.72%	26.82 %

Table 1.2: Error rate threshold Q_{max} for a d-dimensional QKD system as a function of dimension d.

Since a negative r_∞ has no physical meaning, we can find the upper bound of error rate Q as a function of dimension d by setting $r_\infty = 0$. Some examples are shown in Table 1.2. Obviously, a larger d will lead to a higher error threshold, which indicates a better robustness against eavesdropping and system imperfections. Meanwhile, as shown in Figure 1.2, for a given error rate, a higher encoding Hilbert space will yield a larger secure key fraction r_∞, resulting in a higher photon efficiency. Thus, high-dimension QKD systems are more desirable than the simple binary encoding in real applications.

1.4 Development of OAM QKD

As what we discuss in chapter 1.1, OAM states, denoted by its OAM quantum number ℓ, are orthogonal regardless of its radial amplitude and phase distributions. For simplicity, we will use Dirac notation $|\ell\rangle$ to denote OAM state with OAM quantum number equal to ℓ. Unlike the binary encoding space spanned by the polarization degree of freedom, the Hilbert space spanned by OAM states is infinitely large, which is ideal for high-dimensional information encoding. Thus, OAM becomes a promising candidate for high-dimensional QKD, and the development of OAM QKD has been almost two decades.

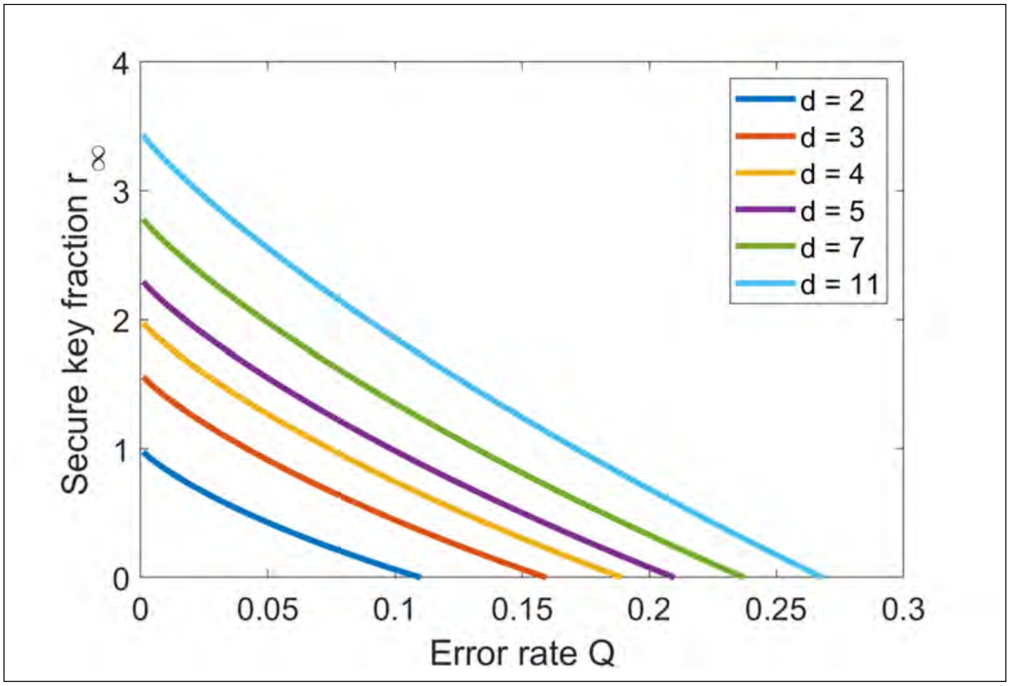

Figure 1.2: Secure key fraction r_∞ as a function of error rate Q for different encoding dimension d.

The first announcement of implementing OAM states into quantum information field was proposed by Molina-Terriza *et al.* in 2001 [56]. They showed that these vortex states $|\ell\rangle$ can be well engineered qudits for high-dimensional quantum information systems. After this work, numerous studies were developed to achieve high-dimensional QKD.

Even though the first OAM-based high-dimensional entanglement source, with $d = 3$, was developed by Vaziri *et al.* in 2002 [31], the most widely used source for OAM QKD is attenuated coherent state with decoy states [48, 49, 57]. To prepare OAM states with arbitrary ℓ, one needs to use computer-generated digital hologram to add helical phase front to the fundamental Gaussian state. This process is usually achieved by using phase only liquid crystal on silicon-spatial light modulators (LCOS-SLM) with a slow modulation rate, which is usually about 60 Hz. In 2013, Mirhosseini *et al.* developed a method of encoding phase and amplitude structures onto photons with digital micromirror devices (DMDs) [58]. These amplitude-only spatial light modulators are faster (up to 20 kHz) and more economical than LCOS-SLMs, which provides a more realistic way to encode OAM states on photons. A faster photon rate can be achieved by multiplexing the outputs of several static spiral phase plates or DMDs.

Efficiently measuring OAM states had been a critical issue in OAM community since early 90s. Traditional projective measurements via forked diffraction gratings can measure only one OAM state $|\ell\rangle$ at a time [31, 32, 33, 34]. If a large encoding space is implemented, such a procedure will require lots of photons to raster scan the OAM spectrum. Thus, this approach is not only inefficient, but also impractical for QKD. The first lossless OAM sorting technique was demonstrated in 2002 by Leach *et al.* at the University of Glasgow [59]. They implement a ℓ-dependent interferometer to sort even and odd OAM states. By cascading multiple interferometers, four OAM states are efficiently separated and measured. The effectiveness of such an OAM state sorter has been used in some proof-of-principle OAM QKD experiments with up to four OAM states [40]. Unfortunately, due to the challenges in cascading multiple OAM interferometers, this method has not proved to be effective for any larger encoding space. A more effective and efficient approach was initially proposed by Berkhout *et al.* in 2010 and significantly improved by Mirhosseini *et al.* in 2013 [60, 61]. The idea is transforming the ℓ-dependent azimuthal structure into ℓ-dependent transverse position. Such a transformation is achieved by using Cartesian to log-polar transformation, which is accomplished by two phase plates. After the transformation, each OAM state $|\ell\rangle$ will acquire a ℓ-dependent tilt phase. By performing the Fourier transform, different OAM states will be projected to a different transverse locations, and then be collected separately by an array of fibers. The crosstalk is about 80% in the original design [62], and then be further enhanced to 92% by copying the beam in the Fourier plane, which is achieved through adding two additional phase plates [61]. The crosstalk can be further reduced to a lower level by adding more copies, which enables an efficient and effective sorting of OAM states and its MUB angular (ANG) basis suitable for high-dimensional OAM QKD. A more compact design, which only consists of two phase plates, is demonstrated in 2017, showing a more robust and concise OAM sorter [63].

By combining the techniques mentioned above, the first high-dimensional OAM QKD with $d = 7$ was demonstrated by Mirhosseini *et al.* in 2015 [52]. By encoding information in the OAM and ANG bases, a channel capacity of 2.05 bits per sifted photon is achieved in a 2-m long link. A simple demonstration of the robustness against intercept-and-resend attack is performed showing the advantage of high-dimensional encoding. A fiber-based OAM QKD system has been demonstrated as well in 2019 [40]. A 4-dimensional

OAM encoding space is implemented in a 1.2-km-long fiber communication link. Thus, the proof-of-principle demonstration of high-dimensional OAM QKD has been illustrated, and the urgent goal in the OAM QKD community is trying to achieve high-dimensional QKD in a long-distance communication link.

While efficient and high-fidelity fibers for high-order spatial modes are under investigation [40, 41, 42, 43, 44], OAM QKD in free-space links remains desirable due to the greater flexibility in applications, larger mode volume and the lower loss. Thus, the first half of this dissertation will focus on the high-dimensional OAM QKD in a long-distance free-space communication link. The first urgent task is finding the optimal information carrier in a given communication link. As what we discuss in section 1.1, the choice of the amplitude distribution $A(r, z)$ and the phase structure $\exp(i\phi(r, z))$ will not hurt the orthogonality of OAM states. Thus, by finding the optimal $A(r, z)$ and $\exp(i\phi(r, z))$, one can optimize both the transmission efficiency and the robustness against atmospheric turbulence of the OAM carrier. The second part will focus on the investigation of security problems in a long-distance free-space OAM QKD system when a large encoding space is implemented. The existence of state-dependent diffraction in OAM states will lead to state-dependent efficiency and phase. Even though this effect is not evident when either the encoding space is small or communication distance is short, a security problem which cannot be ignored will rise up when a real long-distance OAM QKD system with a large encoding space is under consideration. The last part will focus on the mitigation of atmospheric turbulence in free-space OAM QKD using adaptive optics, which has been a long-standing problem for both classical and quantum free-space OAM communication.

Chapter 2

Finding the optimal information carrier in a turbulent channel

An efficient communication in a given free-space link usually requires the development of a specific communication mode. Even though the study of OAM communication mode in vacuum has been investigated [64], the chocie of the optimal OAM carrier in a turbulent channel is still unknown. Therefore, a systematic comparison of different OAM carriers, in terms of the transmission efficiency and the robustness against atmospheric turbulence, in a turbulent channel is necessary, and we will develop a numerical simulation to perform a comprehensive study on this topic in this chapter.

2.1 Candidate OAM carrier

As what we discuss in Section 1.1, the orthogonality of OAM states does not rely on the amplitude distribution $A(r, z)$ and the phase structure $\exp(i\phi(r, z))$. Therefore, we can optimize the performance, in terms of transmission efficiency and the robustness against atmospheric turbulence, of an OAM carrier in a given free-space link by finding the best combination of $A(r, z)$ and $\exp(i\phi(r, z))$.

The simplest light field carrying OAM is the one with a top-hat amplitude, i.e. a uniform amplitude and phase distribution with a circular beam shape:

$$u(r,\theta,z) = \begin{cases} \exp(i\ell\theta)\exp(ikz) & \text{for} \quad |r| \leq R \\ 0 & \text{for} \quad |r| > R \end{cases}, \tag{2.1}$$

where R is the radius of the field. This set of states is named as Pure Vortex (PV) states.

In the case that the field is prepared with a square amplitude distribution, we name these fields as Plane Wave (PW) states. The mathematical description can be found as:

$$u(x,y,z) = \begin{cases} \exp(i\ell\theta)\exp(ikz) & \text{for} \quad |x|\&|y| \leq L \\ 0 & \text{for} \quad |x|\&|y| > L \end{cases}. \tag{2.2}$$

Here, for simplicity, we use Cartesian coordinates to give a concise form of PW states.

A more complex but well-known set of states carrying OAM is LG states, which has been mentioned in Section 1.1. This set of states is the eigenstate of a circularly symmetric cavity, and is described by two indices: OAM quantum number ℓ and radial quantum number p:

$$\begin{aligned} u(r,\theta,z) =& C_{\ell p}^{LG}\frac{\omega_0}{\omega(z)}(\frac{\sqrt{2}r}{\omega(z)})^{|\ell|}\exp(-\frac{r^2}{\omega^2(z)})L_p^{\ell}(\frac{2r^2}{\omega^2(z)})\times \\ & \exp(ik\frac{r^2}{2R(z)})\exp(i\ell\theta)\exp(i\psi(z)), \end{aligned} \tag{2.3}$$

where L_p^{ℓ} stands for the generalized Laguerre polynomials, and $C_{\ell p}^{LG}$ is the normalization constant. $R(z)$ is the radius of the wavefront curvature, which is defined as $R(z) = z + z_R^2/z$. $\omega(z) = \omega_0\sqrt{1+(z/z_R)^2}$ is the beam radius at location z while ω_0 is the waist radius and $z_R = \pi\omega_0^2/\lambda$ is the Rayleigh range. The z-dependent phase term $\exp(i\psi(z)$ is Gouy phase, which can be written as:

$$\exp(i\psi(z)) = (N+1)\arctan(z/z_R), \tag{2.4}$$

where $N = |\ell| + 2p$ is the mode number.

For now, we already have three candidates carrying OAM. However, as one see, all three states are not designed for free-space communication, which entails the necessity of OAM communication modes to optimize the transmission efficiency. A rigorous development of a communication mode for an arbitrary communication volume was developed in 2000 by David Miller [65]. However, no development of OAM communication mode was specified until 2011 by Glenn Tyler [64]. Since these OAM communication modes are designed to minimize the loss, they are named to be minimum energy loss (MEL) states. Now we will show the process of finding the optimal state for OAM communication in vaccum. If we assume that the input field $u(r,\theta)$

carries ℓ amount of OAM, the input field at Alice can be written as:

$$u(r_A, \theta) = A_\ell(r_A)\exp(i\ell\theta). \tag{2.5}$$

Then after propagating a distance z, the received field before Bob's aperture $u(r_B, \theta, z)$ can be written as:

$$\begin{aligned} u(r_B, \theta, z) =& \frac{2\pi}{i\lambda z}\exp(ikz)\exp(\frac{i\pi r_B^2}{\lambda z})\exp(i\ell\theta)i^{-\ell}\times \\ & \int_{\mu R_1}^{R_1} r_A A_\ell(r_A))\exp(\frac{i\pi r_A^2}{\lambda z})J_\ell(\frac{2\pi r_A r_B}{\lambda z})dr_A, \end{aligned} \tag{2.6}$$

where J_ℓ is the Bessel function of the first kind. R_1 is the radius of the transmitting aperture while μR_1 is the radius of the obstruction at the center. As one can see from Eq. (2.6), the only azimuthal phase term $\exp(i\ell\theta)$ is identical to the input field in Eq. (2.5). Therefore, the propagation of OAM carrier mode in vacuum does not lead to any modal coupling, which is the fundation of OAM free-space communication.

Now we use normalized coordinates α and ρ to denote the transmitting and receiving aperture coordinates r_A and r_B respectively:

$$\begin{aligned} r_A &= R_1\alpha, \\ r_B &= R_2\rho. \end{aligned} \tag{2.7}$$

By substitute Eq. (2.7) into Eq. (2.6), we can calculate the intensity distribution at Bob:

$$I(R_2\rho,\theta) = 4(\frac{\pi R_1^2}{\lambda z})^2 |\int_{\mu}^{1} \alpha A(R_1\alpha)\exp(\frac{i\pi R_1^2\alpha^2}{\lambda z})J_\ell(\frac{2\pi R_1 R_2 \alpha\rho}{\lambda z})d\alpha|^2. \quad (2.8)$$

Therefore, the intensity distribution of the received states is independent of θ, and $I(R_2\rho,\theta)$ can be reduced to $I(R_2\rho)$.

Now we introduce a quantity called Fresnel number product N_f:

$$N_f = \frac{\pi R_1 R_2}{4\lambda z}, \quad (2.9)$$

which quantifies now many spatial modes can be supported for a given link when the spatial location encoding is used. Thus, the Fresnel number product reflects the information capacity of a link. A larger Fresnel number will yield a larger information capacity. For simplicity, we will call it Fresnel number in this dissertation. By using Eqs. (2.8) and (2.9), we can find the received power P_B with obscuration radius νR_2:

$$
\begin{aligned}
P_B =& \int_{\nu R_2}^{R_2} \int_0^{2\pi} rI(r) d\theta dr \\
=& 2\pi R_2^2 \int_{\nu}^{1} \rho I(R_2\rho) d\rho \\
=& \frac{1}{2}\pi (N_f R_1)^2 \int_{\nu}^{1} \rho d\rho \times \\
& |\int_{\mu}^{1} \alpha A(R_1\alpha) \exp(\frac{i\pi R_1^2 \alpha^2}{\lambda z}) J_\ell(N_f \alpha\rho/2) d\alpha|^2 \\
=& \frac{1}{2}\pi (N_f R_1)^2 \int_{\mu}^{1} d\alpha\alpha A(R_1\alpha) \exp(\frac{i\pi R_1^2 \alpha^2}{\lambda z}) \times \\
& \int_{\mu}^{1} d\beta\beta A(R_1\beta) \exp(\frac{i\pi R_1^2 \beta^2}{\lambda z}) \int_{\nu}^{1} d\rho\rho J_\ell(N_f \alpha\rho/2) J_\ell(N_f \beta\rho/2).
\end{aligned}
\tag{2.10}
$$

Before going forward, it is necessary to find the power in the input field to calculate the transmission efficiency. We can simply integrate the input field within the transmitting aperture:

$$
\begin{aligned}
P_A =& \int_{\mu R_1}^{R_1} \int_0^{2\pi} r_A u(r_A, \theta) u^*(r_A, \theta) d\theta dr_A \\
=& 2\pi R_1^2 \int_{\mu}^{1} d\alpha\alpha A_\ell(R_1\alpha) A_\ell^*(R_1\alpha) \\
=& 2\pi R_1^2 \int_{\mu}^{1} d\alpha\alpha [A_\ell(R_1\alpha) \exp(\frac{i\pi R_1^2 \alpha^2}{\lambda z})][A_\ell(R_1\alpha) \exp(\frac{i\pi R_1^2 \alpha^2}{\lambda z})]^*,
\end{aligned}
\tag{2.11}
$$

By comparing Eqs. (2.10) and (2.11), it is convenient to define a quantity $G_\ell(\alpha)$:

$$
G_\ell(\alpha) = \sqrt{2\pi R_1^2 \alpha} A_\ell(R_1\alpha) \exp(\frac{i\pi R_1^2 \alpha^2}{\lambda z}). \tag{2.12}
$$

By substituting Eq. (2.12) into (2.11), the power prepared by Alice is:

$$P_A = \int_{\mu}^{1} d\alpha G_\ell(\alpha) G_\ell^*(\alpha). \tag{2.13}$$

When we substitute Eq. (2.12) into (2.10), the power received by Bob is:

$$P_B = \int_{\mu}^{1} d\alpha G_\ell(\alpha) \int_{\mu}^{1} G_\ell^*(\alpha) K_\ell(\alpha, \beta), \tag{2.14}$$

where $K_\ell(\alpha, \beta)$ is defined as:

$$K_\ell(\alpha, \beta) = \frac{1}{4} N_f^2 \sqrt{\alpha\beta} \int_{\nu}^{1} d\rho\rho J_\ell(N_f \alpha\rho/2) J_\ell(N_f \beta\rho/2) \tag{2.15}$$

Now we can see that Eq. (2.13) is just an inner product of the field $G_\ell(\alpha)$ while Eq. (2.14) is the expectation value of operator $K_\ell(\alpha, \beta)$ under the field $G_\ell(\alpha)$. Therefore, it is convenient to use Dirac notation to simplify Eqs. (2.13) and (2.14):

$$P_A = \langle G_\ell | G_\ell \rangle , \tag{2.16}$$

$$P_B = \langle G_\ell | K_\ell | G_\ell \rangle . \tag{2.17}$$

Based on these two equations, the optimal OAM carrier is the field that solves the following constrained optimization problem: maximize P_B for a given P_A. This problem can be solved by using a Lagrange multiplier, i.e. introducing an additional scalar variable η: maximize the quantity $\widetilde{P}$. The definition of $\widetilde{P}$:

$$\widetilde{P} = \langle G_\ell | \, K_\ell \, | G_\ell \rangle - \eta[\langle G_\ell | G_\ell \rangle - P_A]. \tag{2.18}$$

By differentiating $\widetilde{P}$ with respect to the bra vector $\langle G_\ell|$, we will have:

$$\frac{\partial \widetilde{P}}{\partial \langle G_\ell|} = K_\ell \, | G_\ell \rangle - \eta \, | G_\ell \rangle \, . \tag{2.19}$$

Through setting the differential above to 0, we can find that the optimal field $|G_\ell\rangle$ satisfy an eigenvalue equation:

$$K_\ell \, | G_\ell \rangle = \eta \, | G_\ell \rangle \, , \tag{2.20}$$

If we further multiply $\langle G_\ell|$ on both sides and perform some simple math, we will find the physical meaning of the eigenvalue η is the transmission efficiency of the eigenvector G_ℓ:

$$\eta = \frac{\langle G_\ell | \, K_\ell \, | G_\ell \rangle}{\langle G_\ell | G_\ell \rangle} = \frac{P_B}{P_A}. \tag{2.21}$$

Note that, operator K_ℓ is only dependent on the Fresnel number N_f and OAM quantum number ℓ. Therefore, once we know the Fresnel number N_f and the OAM field $|\ell\rangle$ under consideration, it is possible to find the operator K_ℓ and then the corresponding eigenvector and eigenvalue. As we mentioned before, since these eigenvectors minimize the loss in a given link, we call them

MEL states. However, considering that the MEL states highly depend on N_f and ℓ, we still need to find each specific field G_ℓ and η for each combination of N_f and ℓ. Luckily, a numerical solution package has been developed by Glenn Tyler and his colleagues at the Optical Science Company [64, 66, 67, 68], and we can simply prepare these states by implementing this package.

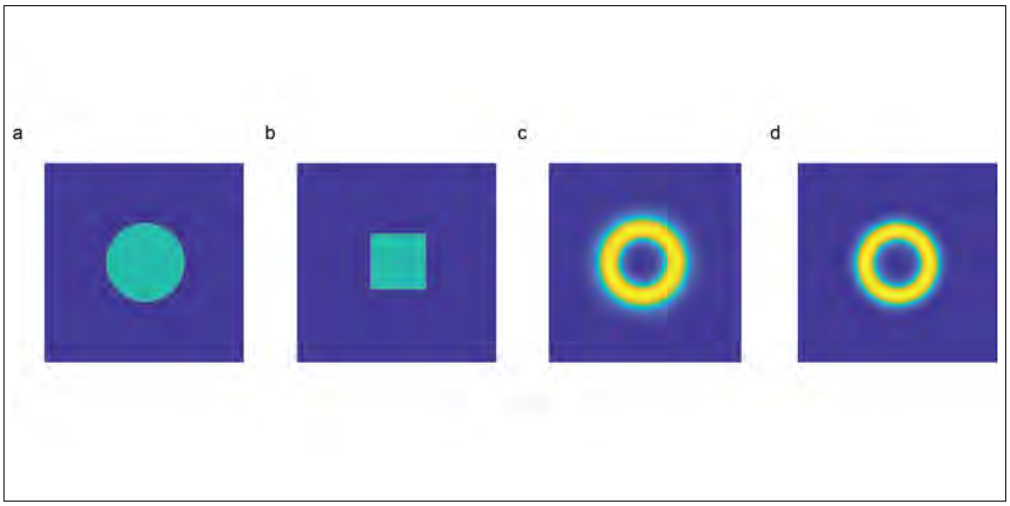

Figure 2.1: Intensity distribution of different OAM carriers with $\ell = 3$. (a): Pure Vortex (PV) state. (b): Plane Wave (PW) state. (c): Laguerre Gaussian (LG) state. (d): Minimum energy loss (MEL) state.

To directly show the difference between all the candidates, we plot the intensity distribution of them with $\ell = 3$ and $N_f = 4.8$ in Figure 2.1. It is easy to identify PV and PW states from the other two states due to the uniform intensity distribution and the shape. LG state and MEL state are similar to each other at the first glance. This comes from the fact that when N_f becomes very large, the communication link can be considered as a symmetric cavity, and hence the eigenstate of such a link will be the eigenstate of a circularly symmetric cavity. i.e. the LG state [65, 64]. When N_f is not very large, for example what we show in Figure 2.1, if we carefully compare these two states, we will find that the edge of MEL state is cut off leading to discontinuous field distribution, while the edge of LG state is still smooth.

2.2 Brief introduction to atmospheric turbulence

As what we show in the last section, there are several candidates available for OAM communication, and one of them, i.e. the MEL state, is the specifically designed communication mode for OAM communication. It seems that no further comparison and study are required since MEL state has the optimal transmission efficiency in vacuum. However, due to existence of atmospheric turbulence in most realistic free-space communication links, there is no evidence showing the use of MEL states is still advantageous. Therefore, we have to take the effect of turbulence into consideration. Before we proceed further, it is convenient to briefly introduce the theory of atmospheric turbulence in this section.

Classical studies of turbulence, a phenomenon that can be found in many fluids, were mainly focused on the fluctuations in the velocity field of a viscous fluid [69]. In atmospheric turbulence, the random fluctuations in the refractive index of the atmosphere is the result of random fluctuations in the wind velocity in the presence of moisture and temperature gradients [69]. Early studies by Kolmogorov suggest for optical wave propagation, refractive index fluctuation is mainly caused by the fluctuation in temperature. Thus, variations caused by the fluctuation in humidity and pressure are ignored in the following discussion. From Kolmogorov's theory, there is a subclass of atmosphere which has statistical consistency and can be treated with a statistical model [70]. We call these small groups of atmosphere as *turbules*. The length scale of turbules is usually defined by the inner scale l_0 and outer scale L_0. A typical number of l_0 for a near-ground channel is on the order of 1 to 10 mm while the outer scale L_0 usually grows linearly with the order of the height above the ground.

Based on Kolmogorov's theory, the wind velocity distribution $D_v(r_1, r_2)$ is defined as [69]:

$$D_v(r_1, r_2) = \langle |v(r_1) - v(r_2)|^2 \rangle, \tag{2.22}$$

where $v(r_1)$ and $v(r_2)$ are the wind velocity at position 1 and 2 respectively. When $l_0 \ll |r_1 - r_2| \ll L_0$, the wind velocity distribution will follow the universal 2/3 power law [69]:

$$D_v(r_1, r_2) = C_V^2 |r_1 - r_2|^{2/3}, \tag{2.23}$$

where C_V^2 is the velocity structure constant of atmospheric turbulence.

By extending Kolmogorov's theory to the temperature fluctuation, we can find the temperature distribution $D_T(r_1, r_2)$ has the same power law relation when $l_0 \ll |r_1 - r_2| \ll L_0$ [69]:

$$D_T(r_1, r_2) \equiv \langle |T(r_1) - T(r_2)|^2 \rangle = C_T^2 |r_1 - r_2|^{2/3}, \tag{2.24}$$

where $T(r_1)$ and $T(r_2)$ are the temperature at position 1 and 2 respectively, and C_T^2 is the temperature structure constant of atmospheric turbulence.

Based on what we mention before, we attribute the fluctuation in refractive index to the variation in temperature. Therefore, resulting from the velocity and temperature fluctuation described above, one can find that the refractive index structure function exhibits the same behavior when $l_0 \ll |r_1 - r_2| \ll L_0$:

$$D_n(r_1, r_2) \equiv \langle |B(r_1) - B(r_2)|^2 \rangle = C_n^2(z) |r_1 - r_2|^{2/3}, \tag{2.25}$$

where $B(r_1)$ and $B(r_2)$ are the covariance function of refractive index distribution $n(r)$ at position 1 and 2 respectively. $C_n^2(z)$ is the refractive index structure constant of atmospheric turbulence. For simplicity, we usually call it *structure parameter* or *structure number.* $C_n^2(z)$ characterizes the strength of atmospheric turbulence. Usually, when $C_n^2(z)$ is on the order of $10^{-17} m^{-2/3}$ or less, the turbulence is considered as weak turbulence, while when $C_n^2(z)$ is on the order of $10^{-13} m^{-2/3}$ or more, the turbulence is strong. However, since $C_n^2(z)$ only depends on weather, we will show that this is not a rigorous condition to justify whether the optical system suffers from strong or weak turbulence. Another quantity, which depends on both weather and optical system, will be introduced later to provide a more accurate description of the level of turbulence.

Based on Eq. (2.25), we can get the associated power spectral density $\Phi_n(\kappa)$ for refractive index fluctuations:

$$\Phi_n(\kappa) = 0.033 C_n^2(z)\kappa^{-11/3}, 1/L_0 \ll |r_1 - r_2| \ll 1/l_0. \tag{2.26}$$

This is the famous Kolmogorov power law spectrum, which provides a simple statistical description of the behavior of atmospheric turbulence. It is worth noting that this spectrum is only valid when the condition $1/L_0 \ll |r_1 - r_2| \ll 1/l_0$ is satisfied. To justify the spectrum for wave numbers from zero spatial frequency, it is ordinarily assumed that the outer scale is infinite. However, it is obvious that such an assumption will not be valid for most realistic scenarios. Therefore, we will introduce von Karman spectrum model as the replacement, which is valid for all wave numbers:

$$\Phi_n(\kappa) = \begin{cases} 0.033 C_n^2(z)\frac{1}{(\kappa^2+\kappa_0^2)^{11/6}} & \text{for} \quad 0 \le \kappa \ll 1/l_0 \\ 0.033 C_n^2(z)\frac{\exp(-\kappa^2/\kappa_m^2)}{(\kappa^2+\kappa_0^2)^{11/6}} & \text{for} \quad 0 \le \kappa \ll \infty \end{cases}, \tag{2.27}$$

where $\kappa_0 = 1/L_0$ and $\kappa_m = 5.92/l_0$. The upper expression in Eq. (2.27) is the original von Karman model while the lower one is the modified von Karman model which takes both outer and inner scale effects into consideration. In most cases, both spectrum have similar performance so that people simply call them von Karman spectrum model. In our case, we use the upper expression in Eq. (2.27) as the spectrum model to simulate turbulence. It is worth noting that, when $\kappa_0 \ll \kappa \ll \kappa_m$, both expressions in Eq. (2.27) will reduce to the Kolmogorov model in Eq. (2.26).

As what we discuss before, $C_n^2(z)$ is the parameter to describe the level of turbulence, and hence the fluctuation in the refractive of index. Therefore, one can also quantify the fluctuation in phase at Bob using $C_n^2(z)$. It was demonstrated by Fried that, under Kolmogorov model, the turbulence-induced phase distribution D_ϕ has the form [71]:

$$D_\phi = 6.88(\frac{|r_1 - r_2|}{r_0})^{5/3}, \tag{2.28}$$

where r_0 is the Fried parameter which describes the effective coherence length of the turbule. r_0 can be calculated from $C_n^2(z)$ using the following relation:

$$r_0 = [0.42k^2 \int_0^L C_n^2(z)dz]^{-3/5} = (0.42k^2 C_n^2 L)^{-3/5}, \tag{2.29}$$

where L is the length of the channel, i.e. the communication distance. Here we have assumed that the structure number C_n^2 is a constant, which is usually valid when the altitude difference of the channel is negligible.

If we assume that the light field has a diameter of D, it is convenient to use such a quantity D/r_0 to quantify the strength of turbulence. Comparing the the structure number C_n^2, D/r_0 has two advantages: 1). it includes both effects of the optical system and weather. This indicates that, when we discuss the turbulence effect on a specific communication system, it is more accurate to use D/r_0 to quantify the influence. 2). this quantity has a more intuitive physics understanding. The quantity $(D/r_0)^2$ ordinarily describe how many independent small turbules (each turbule itself is coherent) inside the cross section of the beam. Therefore, one can easily speculate that a small D/r_0 ($D/r_0 \ll 1$) indicates a weak turbulence and vice versa. Hence, in the rest of this dissertation, we prefer using D/r_0 to quantify the level of turbulence.

Apart from the random phase, turbulence will distort the amplitude as well. The amplitude fluctuation is usually characterized by the quantity scintillation σ_η^2:

$$\sigma_\eta^2 = 0.31 k^{7/6} C_n^2 L^{11/6}. \tag{2.30}$$

Based on what we discuss above, one can clearly see that turbulence can distort both the amplitude and phase structure of the optical beam. Therefore, it is necessary to study the influence of turbulence on OAM states to achieve realistic free-space OAM communication. Luckily, numerous studies have been done in the past two decades [72, 73, 74, 75, 76, 77, 78, 79, 80, 81]. However, each research simply studies the performance of one or two specific modes, and a comprehensive comparison between multiple candidates is lacking.

2.2.1 Thin phase approximation

Early study of the propagation of light beams through turbulence arose in the astronomy community. To study the effects of turbulence on the image of astronomical objects, people usually assumes that the turbulence is a thin phase screen which adds a random phase distribution to the beam. The assumption is valid since the thickest turbulence locates close to the telescope.

In free-space communication, this assumption will be not accurate since the beam will keep propagating through a turbulent channel. However, the thin phase approximation is still a good model to describe weak turbulence and will be the cornerstone for simulating thick turbulence.

A representation of a simple system based on thin phase approximation is illustrated in Figure 2.2(a), and four random thin phase screens following the von Karman spectrum are shown in Figure 2.2(c). Similar to the astronomy case, we attribute all the turbulence to a thin random phase screen locating close to the receiving aperture. It is worth noting that the structure number C_n^2 is not a proper quantity to rigorously describe the level of turbulence for thi, and the Fried parameter r_0 of this phase screen will be the same as the measured r_0 of the turbulent channel.

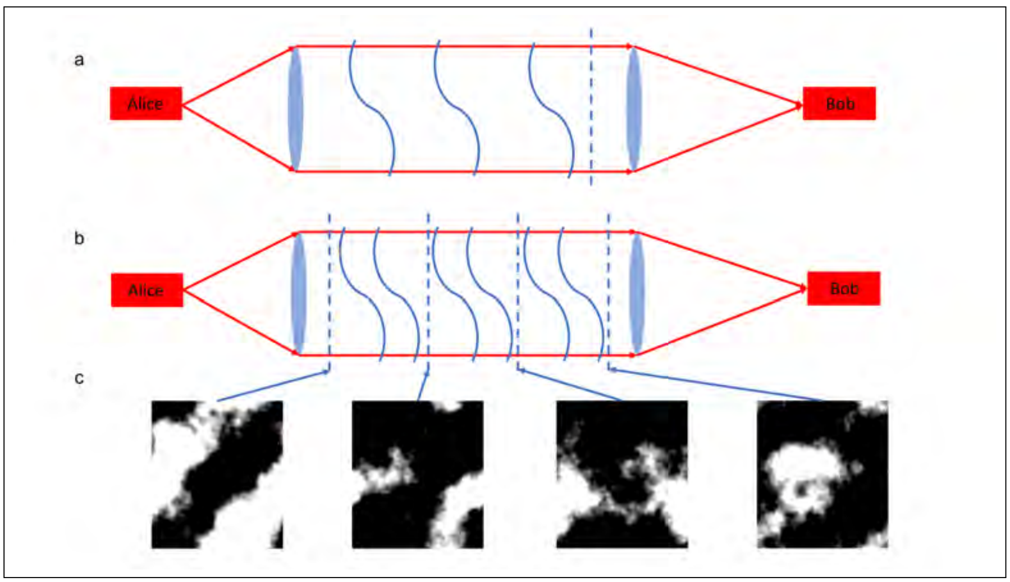

Figure 2.2: (a): A turbulent channel based on thin phase approximation. (b): Use thin phase approximation to simulate a turbulent channel under thick turbulence. (c): Prepared random thin phase screens using von Karman spectrum.

2.2.2 Simulating thick turbulence using the thin phase approximation

The thin phase approximation model presented above allows a simple description of turbulence. However, in realistic scenarios, such approximation usually fails due to the complicated nature of turbulence. Luckily, thin phase approximation can be an useful tool to simulate thick turbulence. A complicated real communication channel under thick turbulence will become tractable by decomposing the channel into multiple thin phase screens.

A simple example is shown in Figure 2.2(b). The goal is building a model to represent a communication channel under thick turbulence. The first step is decomposing the turbulent channel into four thin phase screens and three segments of vacuum. Since all the turbulence effects are carried by phase screens, the behavior of light propagating between two screens are simply determined by the diffraction in vacuum. Then the task is determining the Fried parameter of each screen and the separation between two screens. The constrain that the entire system should have the same parameter and communication distance as what we measured in lab. For simplicity, we can either set all phase screens to have the same Fried parameter, or to be equally separated. In our case, all phase screens have the same Fried parameter and the separations are free. The relation between the Fried parameter of the entire link and the Fried parameter of each screen can be found as:

$$r_{0,\text{total}} = [\sum_{i=1}^{N} r_{0,i}^{-5/3}]^{-3/5}, \tag{2.31}$$

where $r_{0,i}$ represents the Fried parameter of the ith screen. Based on the equation above and the same optimization logic in Ref. [78], we could determine the separations d_i between thin phase screens for a given $r_{0,\text{total}}$.

2.3 Simulating OAM communication with different carriers in a thick turbulence

Based on what we introduce in last two sections, we can develop a numerical simulation code to quantitatively compare the performance of different OAM carriers in a given turbulent communication link. Here we mainly focus on two aspects: the average transmission efficiency η and the secure key fraction r_∞.

The average transmission efficiency η is defined as the average of the transmission efficiency η_ℓ of each OAM state:

$$\eta = \frac{\sum \eta_\ell}{d} = \frac{\sum P_{B,\ell}/P_{A,\ell}}{d}, \tag{2.32}$$

where d is the dimension of the encoding space. $P_{B,\ell}$ stands for the received power of OAM state ℓ while $P_{A,\ell}$ is the launched power of OAM state ℓ. The calculation of secure key fraction r_∞ follows the Eq. (1.27). Here we use the quantity fidelity F in the calculation, which is defined as: $F = 1 - Q$ and represents the probability that the received state is identical to the launched state. Since r_∞ only depends on the fidelity F for a given encoding dimension d, r_∞ indicates the robustness of each set of mode against atmospheric turbulence. A better robustness will yield a higher fidelity F, which further leads to a higher secure key fraction r_∞.

The simulation starts with the selection of a communication link under investigation. Based on the blueprint of our cross-campus QKD link, we choose a link with a communication distance $L = 340$ m with an encoding dimension $d = 7$, i.e. OAM quantum number ℓ from -3 to 3. The clear aperture of the Alice's launch apparatus is 2.5 cm, and the the collecting aperture size of Bob's optics is 5.4 cm. Thus, the Fresnel number N_f of the system is 4.8. D/r_0 is varied from 0.1 to 3, which covers a turbulence level from weak to strong turbulence. Based on what we describe in Section 2.2.2, we use 4 separated thin phase screens to simulate the realistic thick turbulence. The $r_{0,i}$ of each phase screen is determined by Eq. (2.31) for each realization of D/r_0, and then the separation d_i is calculated based on $r_{0,i}$.

The logic of the simulation is as follows:

1). Prepare the desired state to match the transmitter aperture size;

2). Use angular spectrum to propagate the state through the turbulent channel. For our four-pieces channel, the propagation sequentially consists of four individual angular spectrum propagation;

3). Use a finite aperture to collect the state at Alice's side. The fidelity of each state is found by calculating the inner product of the received state and the desired state which comes from the propagation through the same link without any turbulence;

4). Repeat step 1) to 3) for 100 realization of turbulent channels to calculate the average efficiency η_ℓ and fidelity F_ℓ;

5). Repeat step 1) to 4) for each OAM state within one set of mode to calculate η and F;

6). Repeat step 1) to 5) for each set of mode.

2.4 Results and conclusions

The main results of the simulation are shown in Figure 2.3. We plot the average transmission efficiency η of different OAM carriers as a function of turbulence level D/r_0 in Figure 2.3(a). MEL states have the best efficiency among all candidates at all turbulence levels. The advantage in efficiency becomes even larger when the turbulence becomes stronger. When $D/r_0 = 0.1$, i.e. weak turbulence, the transmission efficiency of MEL states is 8.83% larger than the efficiency of PW states. When $D/r_0 = 3$, i.e. strong turbulence, the advantage in efficiency becomes 19.09%. Thus, MEL states can provide the optimal efficiency even with the existence of turbulence. PV states and LG states share similar behaviors in terms of transmission efficiency, which matches the theoretical predictions reported in Ref. [73]. PW states have the worst transmission efficiency among all candidates, which originates from the square shape of the beam. Moreover, the transmission efficiency of PW states drops faster than any other candidates, which indicates a much worse efficiency under stronger turbulence.

As a contrast, PW states provide the best robustness against atmospheric turbulence as shown in Figure 2.3(b). As the turbulence level increases, the key rate of PW states drops much slower than any other candidates. When D/r_0 becomes 1, PW state becomes the only survival candidate which can provide positive secure key fraction r_∞. It is worth noting that we have ignored all data points with negative r_∞ since they lack physical meaning. Comparing to PV and LG states, the superior performance in robustness of PW states is not surprising because of the previous research shown in Ref. [75]. Moreover, PW states are even lessly degraded by turbulence comparing to MEL states (the second the best robustness), which shows that PW states are the most localized state in space among all candidates [75].

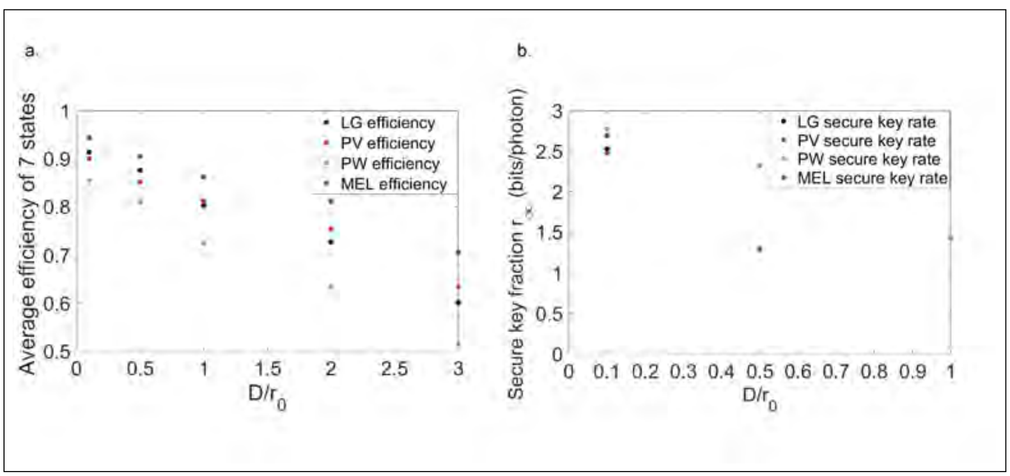

Figure 2.3: (a): Average efficiency of different OAM carriers as a function of D/r_0. (b): Secure key fraction of different OAM carriers as a function of D/r_0.

By calculating the secure key rate per transmitted photon, which is the product of η and r_∞, we can find that when $D/r_0 = 0.5$, the secure key rate of

PW states (1.88 bits/photon) is larger than MEL states (1.17 bits/photon). Since PW states will be the only choice when D/r_0 goes stronger, it seems that PW states should be optimal carrier. However, we should note that all the calculation and simulation presented above have not included any correction of atmospheric turbulence yet. In fact, in realistic scenarios associated with atmospheric turbulence, correction systems are usually necessary. One simple example would be astronomy, where adaptive optics, one solution to correct the distortions of the incoming wavefront, has been used for decades. In the meantime, some studies of the possibility of using adaptive optics to improve the performance of OAM communication in free-space links were performed recently [4, 9, 67, 68, 78, 82, 83, 84]. The enhancement of the fidelity in a distorted channel, including the channel with simulated turbulence and real turbulence, was observed in multiple researches. For example, even under thick turbulence (simulated turbulence generated by two phase-only SLMs), it is possible to double the key rate by implementing a simple adaptive optics system [78]. A more detailed discussion and research on this topic will be presented in Chapter 4. What is more, digital phase conjugation has also been implemented to improve the performance of OAM states in both multi-mode fiber and free-space links, which can provide better correction for weak turbulence [1, 2, 19]. Therefore, it is evident that the fidelity of OAM states can be improved by implementing distortion correction systems. However, the transmission efficiency η can hardly be improved once the OAM carrier is selected. As the consequence, we finally choose MEL states as the optimal information carrier because they have the best efficiency and the second to the best fidelity. It is worth noting that, even though PW states have the best robustness against turbulence, they are the second to the best choice as the information carrier due to the large disadvantage in transmission efficiency. In the rest of the dissertation, all OAM states are carried by MEL states unless the exception is announced.

Chapter 3

Security loophole in OAM QKD induced by state-dependent diffraction

In traditional protocols for QKD, the sender should be able to encode and transmit photons in two or more mutually unbiased bases, and there is no conflict between diffraction and security. However, since OAM states have a state-dependent diffraction [85], high-dimensional OAM QKD may suffer from additional security problem compared to traditional polarization or time-bin encoding. To clearly understand the role of state-dependent diffraction in high-dimensional QKD, we analyze the extent to which the performance of QKD is degraded by diffraction effects that become relevant for long propagation distances and limited sizes of apertures. In such a scenario, different OAM states experience different amounts of diffraction, leading to state-dependent loss and phase acquisition, causing an increased error rate and security loophole at the receiver. To solve this problem, we propose a pre-compensation protocol based on pre-shaping the transverse structure of quantum states. We demonstrate, both theoretically and experimentally, that when performing QKD over a link with known, state-dependent loss and phase shift, the performance of QKD will be better if we intentionally increase the loss of certain states to make the loss and phase shift of all states equal. Our results show that the pre-compensated protocol can significantly reduce the error rate induced by state-dependent diffraction and thereby improve the secure key rate of QKD systems without sacrificing the security.

3.1 Introduction to the background

As what we introduce in the first chapter, one characteristic of an OAM state is its ℓ-dependent diffraction [85]. Because of the state-dependent diffraction (SDD), OAM states with higher ℓ will have larger far-field sizes, and acquire more propagation phase (for example, the Gouy phase of Laguerre Gaussian (LG) states). Thus, in practical free-space communication links, different OAM states will suffer different amounts of loss for a given collection aperture of finite size [80, 81], leading to ℓ-dependent detection efficiency. Similar problems occur for states in the complementary angular (ANG) basis, which consist of an equal superposition of OAM states with fixed relative phase between adjacent OAM components [52, 58]. Due to the SDD, both the amplitude of each OAM state and the relative phase will be modified. Therefore, the received state will be different from the transmitted state, increasing the error rate at the receiver even in the absence of an eavesdropper. The adverse effects of SDD in both OAM and ANG bases result in QKD systems less robust against background noise, measurement errors and eavesdropping. Although OAM-based QKD systems have been demonstrated in both laboratory and outdoor environments [52, 86, 87], the influence of SDD on QKD systems has not yet been adequately addressed in previous work [5].

In our analysis, we use OAM basis and angular (ANG) basis to form the MUBs in OAM QKD. It is worth noting that even though the following discussion is based on this set of MUBs, the analysis and strategy can be applied to other basis as long as the SDD is present. The SDD results in an efficiency mismatch in OAM basis and an increased error rate in ANG basis, which leads to a lower secure key rate. These SDD-induced defects are quantitatively studied as a function of the Fresnel number product N_f in vacuum, which is defined in Eq. (2.9). To get rid of the constant factor, we use the diameters of transmitting and receiving apertures, which leads to a simplified form of N_f:

$$N_f = \frac{\pi D_A D_B}{\lambda z}, \tag{3.1}$$

where D_A and D_B are the diameters of the circular transmitting and receiving apertures respectively, λ is the wavelength of the light, and z is the propagation distance. For a given free-space link, the parameter N_f shows how strong the diffraction is. A small N_f ($N_f \ll 1$) indicates a link suffering from a strong diffraction whereas the diffraction is negligible for links with $N_f \gg 1$.

3.2 Theoretical analysis

Because of the finite sizes of D_A and D_B, higher-order OAM states, which have stronger diffraction, will experience greater loss and acquire more propagation phase. Since our OAM carrier is MEL state, to determine the channel transmission efficiency of a specific OAM state, we define a propagation operator $\hat{F}$ that transfers the OAM eigenstate prepared by Alice $|\ell\rangle_A$ to the state received by Bob $|\ell\rangle_B$ (which is also an OAM eigenstate but has a different radial amplitude distribution) as:

$$|\ell\rangle_B = \hat{F}|\ell\rangle_A. \tag{3.2}$$

The operator $\hat{F}$ includes the effects of propagation in vacuum and the finite apertures at both transmitter and receiver sides. Therefore, we do not include any turbulence effects into our analysis. Note that $\hat{F}$ only results in different amounts of loss and phase, but does not introduce any crosstalk between different OAM $|\ell\rangle$ states. Thus, this is not a unitary transformation, and if we define the efficiency η_ℓ as $\eta_\ell = \langle\ell|\ell\rangle_B/\langle\ell|\ell\rangle_A$, we obtain the following eigenvalue relation:

$$\hat{K}_\ell|\ell\rangle_A = \eta_\ell|\ell\rangle_A, \tag{3.3}$$

where $\hat{K}_\ell = \hat{F}^\dagger\hat{F}$, and the theoretical transmission efficiency of $|\ell\rangle_A$ in vacuum is represented by η_ℓ which is a function of both OAM quantum number ℓ and Fresnel number product N_f [64]. The details of this part can be found in Chapter 2.1.

In OAM-based QKD, the complementary ANG basis is the Fourier conjugate of the OAM basis. The ANG state of index j is defined as [52, 58]:

$$|j\rangle = \frac{1}{\sqrt{d}} \sum_{\ell=-L}^{L} |\ell\rangle e^{-i2\pi j\ell/d}, \tag{3.4}$$

where d is the dimension of the Hilbert space and L is the maximum OAM quantum number in use, which satisfies the relation: $2L + 1 = d$. The ANG basis and OAM basis form two mutually unbiased bases (MUBs), and the use of two or more sets of MUBs guarantees the unconditional security of QKD [48, 88].

In practice, as we mentioned above, different OAM states will suffer different amounts of diffraction, as do the OAM components of an ANG state. As shown in Figure 3.1, for a low Fresnel number product ($N_f \ll 1$), there are huge efficiency differences between lower-order and higher-order OAM states. This difference results in a nonuniform probability of detecting the OAM states. The ANG basis for Bob will thus be modified as:

$$\begin{aligned} |j\rangle_B = \frac{1}{\sqrt{\eta_j}} \hat{F} |j\rangle_A &= \sum_{p=0}^{d-1} \sqrt{P_{j,p}} |j+p\rangle_A \\ &= \sum_{\ell=-L}^{L} \sqrt{P_\ell} |\ell\rangle_A e^{-i\ell(2\pi j/d - \psi(z))}, \end{aligned} \tag{3.5}$$

where $1/\sqrt{\eta_j}$ is the normalization constant given by $\eta_j = \sum_\ell^d \eta_\ell / d$, which describes the transmission efficiency of ANG states. The state $|j\rangle_A$ is the

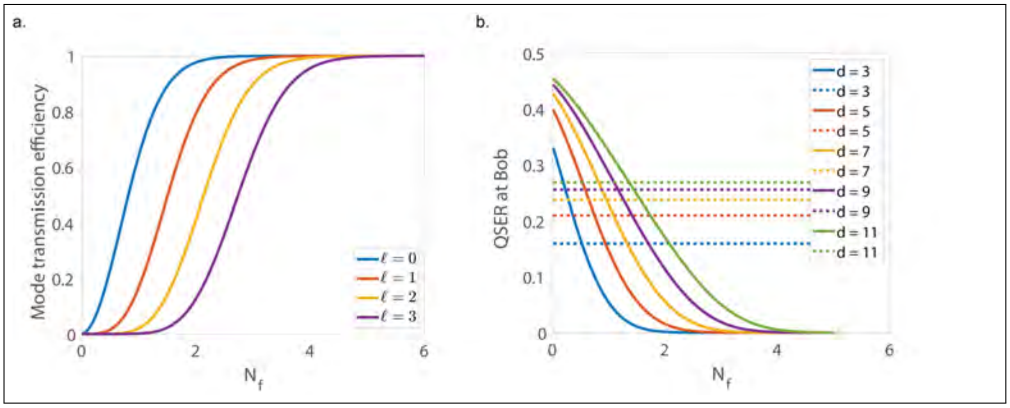

Figure 3.1: (a). The theoretical transmission efficiency η_ℓ of different OAM states as a function of Fresnel number product N_f in a $d = 7$ quantum system. (b) the QSER at Bob as a function of Fresnel number product N_f. QSER is defined as the probability of detecting a photon in a state other than the launched state. The solid lines show the QSER induced by the effects of SDD. The dashed lines show the maximum value of the QSER for which a secure channel can be obtained in the limit where the effects from SDD are negligible ($N_f \gg 1$). When the QSER goes above the corresponding upper bounds, the communication system is not secure and the secure data rate goes to zero.

ANG state j prepared by Alice, which has the same form as Eq.(3). The state $|j\rangle_B$ is the ANG state received by Bob after being modified by SDD. The quantity $P_{j,p}$ characterizes the crosstalk between ANG states, and is equal to the probability of finding the ANG state $|j+p\rangle_A$ prepared by Alice in the ANG state $|j\rangle_B$ received by Bob which has been modified by SDD. The quantity P_ℓ, which can be calculated from transmission efficiency η_ℓ, is the probability of finding the OAM component $|\ell\rangle$ in the modified ANG state $|j\rangle_B$. The quantities $\sqrt{P_{j,p}}$ and $\sqrt{P_\ell/d}$ are related by a discrete Fourier transform. This can be shown by calculating the following inner products based on Eq. (3.5):

$$\begin{aligned} {}_A\langle j+p|j\rangle_B &= \sqrt{P_{j,p}} \\ &= {}_A\langle j+p| \sum_{\ell=-L}^{L} \sqrt{P_\ell}|\ell\rangle_A e^{-i\ell(2\pi j/d-\psi(z))}. \end{aligned} \tag{3.6}$$

Therefore, we can find the following relation:

$$\begin{aligned} \sqrt{P_{j,p}} &= \sum_{m=-L}^{L} \sqrt{\frac{1}{d}} {}_A\langle m| e^{i2\pi(j+p)m/d} \\ &\times \sum_{\ell=-L}^{L} \sqrt{P_\ell}|\ell\rangle_A e^{-i\ell(2\pi j/d-\psi(z))} \\ &= \sum_{\ell=-L}^{L} \sqrt{\frac{P_\ell}{d}} e^{i2\pi(j+p)\ell/d} e^{-i2\pi j\ell/d} e^{i\ell\psi(z)} \\ &= \sum_{\ell=-L}^{L} \sqrt{\frac{P_\ell}{d}} e^{i\ell 2\pi(p/d+\frac{\psi(z)}{2\pi})}. \end{aligned} \tag{3.7}$$

From Eq. (3.7) we can find the $P_{j,p}$ is independent of j and equals the Fourier transform of $\sqrt{P_\ell/d}$.

The propagation phase $\psi(z)$ in Eq. (3.5) is the phase acquired by each OAM state after propagating a distance z. One can notice that the state-dependent loss gives rise to a nonuniform probability distribution of the OAM spectrum, while the state-dependent phase terms introduce extra relative phase between the different OAM components in each ANG state. Both of these effects lead to the crosstalk in ANG basis, which will be further exacerbated in current methods for sorting ANG states [61].

One direct consequence of the increased crosstalk is an increase in the quantum symbol error rate (QSER) at Bob's side (Q_B). Here we define the QSER as the probability of detecting a photon in a state other than the launched state: $Q_B = 1 - (F_{\text{OAM}} + F_{\text{ANG}})/2$, where F_{OAM} and F_{ANG} are the fidelities of the OAM basis and ANG basis respectively. Note that, the QSER is not equal to quantum bit error rate because one error symbol can yield more than one bit error in high dimensional QKD. The QBER is equal to QSER only in two dimensional encoding since one error symbol gives one bit error. It is worth noting that we already exclude all the other errors as well. In our case, assuming there is no eavesdropping, F_{OAM} equals unity while F_{ANG} equals P_j, which means that only the ANG basis suffers an increased QSER. This is because that the SDD does not change the OAM value upon the propagation. Although each OAM state suffers different amount of loss and acquires different phase, the azimuthal phase vortex of each OAM state is maintained during propagation. Therefore, there is no spread in the OAM spectrum but only loss.

To quantitatively show how the QSER changes with diffraction, we have numerically calculated the probability distribution of η_ℓ for Fresnel number product N_f ranging from 0.01 to 5 under different quantum space dimensions in Figure 3.1(a). When N_f is close to 0, only the fundamental Gaussian state ($|\ell = 0\rangle$) can be transmitted. Therefore, the OAM spectrum at Bob will be very narrow, and the ANG spectrum will become uniform, leading to a complete loss of information. As N_f increases, the efficiency of all OAM states will be closer and finally become near 1, indicating that state-dependent loss is reduced and then negligible at high N_f regime. The QSER as a function of N_f is shown in Figure 3.1(b). For a given dimension d, small N_f can significantly increase the QSER even if there is no quantum attack. This will lead to a lower information capacity, and make the system more vulnerable to eavesdropping and quantum cloning since the upper bound for the QSER is fixed for each given dimension d [53, 55]. Moreover, for a given N_f, a higher dimensional system will suffer from more crosstalk introduced by SDD. For instance, in Figure 3.1(b), the crosstalk for $d = 11$ is three times larger than the crosstalk for $d = 7$ in a $N_f = 2$ system. In addition to the loss of information, higher error rate means that one needs to sacrifice a greater fraction of the raw key to detect the existence of eavesdroppers, because the legitimate parties cannot distinguish the errors generated by eavesdroppers' attack from other errors in the system.

The reduced information capacity can be found by calculating the mutual information between Alice and Bob under SDD. The probability of Alice sending out each symbol is still equal, but due to the state-dependent loss, the probabilities of finding each symbol at Bob's side are different. Therefore, for the photons which are registered by both parties, we have the following probabilities:

$$\begin{aligned} P(OAM_{\ell,B}) &= P_\ell, \\ P(ANG_{j,B}) &= 1/d, \\ P(OAM_{\ell,A}) &= P_\ell, \\ P(ANG_{j,A}) &= 1/d. \end{aligned} \tag{3.8}$$

$P(OAM_{\ell,B})$ represents the probability that Bob receives a photon in $|\ell\rangle$, while $P(OAM_{\ell,A}) = P_\ell$ represents the probability that Alice sends out a photon in $|\ell\rangle$. This is because those events that Alice sends out one symbol but Bob receives nothing have been discarded.

The mutual information is defined as Eq. (1.9). In this calculation, even if Alice is sending out each symbol with equal probability, the photon statistics at Bob's side are not uniformly distributed because of the state-dependent loss. Therefore, we have the following probability relations:

$$p(\ell_A, i_B) = P_\ell \delta_{i\ell}, p(j_A, k_B) = P_{j,p}/d, \tag{3.9}$$

where i and k denote the quantum index of OAM and ANG states received by Bob respectively. In real QKD, Alice has to randomly choose her basis, and thus the mutual information between Alice and Bob I_{AB} equals:

$$I_{\mathrm{AB}} = \frac{1}{2} I_{\mathrm{AB,OAM}} + \frac{1}{2} I_{\mathrm{AB,ANG}}, \tag{3.10}$$

where $I_{\mathrm{AB,OAM}}$ represents the mutual information using OAM basis while $I_{\mathrm{AB,ANG}}$ is the mutual information using ANG basis. The final form of I_{AB} can be found as :

$$I_{\mathrm{AB}} = \frac{1}{2}\sum_{p} P_{j,p} \log_2 P_{j,p} d - \frac{1}{2d}\sum_{\ell} \log_2 P_{\ell}. \tag{3.11}$$

As shown in Figure 3.2, it is not difficult to verify that I_{AB} is smaller than the ideal value $\log_2 d$. When N_f is near zero, the information encoded is almost lost, while in the high N_f region, the information capacity gets close to the ideal value. Another interesting result is that the information carried by the two bases is not equal, and that the information encoded in the OAM basis is always larger than that carried in the ANG basis because of the absence of crosstalk in the OAM basis.

Meanwhile, the nonuniform efficiencies induced by SDD in the OAM basis introduces a detection efficiency mismatch in Bob's detectors, which can be utilized by Eve to control the information received by Bob. The security of QKD in the presence of efficiency mismatch has been both theoretically and experimentally studied [89, 90, 91]. Fortunately, measurement-device-independent QKD protocols have been developed to eliminate the loopholes from side-channels including efficiency mismatch [92, 93, 94], and one can implement these protocols to remove this SDD induced security loophole. However, these strategies cannot eliminate the effect of SDD (the increased QSER) in the ANG basis. Therefore, a new protocol that can reduce the

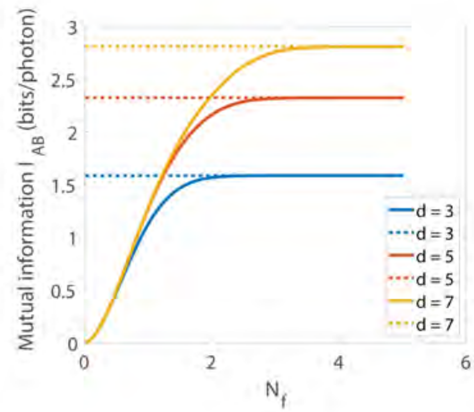

Figure 3.2: The mutual information between Alice and Bob as a function of N_f. The solid lines represent the mutual information with SDD while the dashed lines indicate the mutual information $\log_2(d)$ in the limit where SDD can be ignored ($N_f \gg 1$).

effect of SDD in both bases needs to be developed.

3.3 Waist pre-compensation protocol

From the discussion above, one can conclude that the non-uniform efficiency induced by SDD leads to a security loophole, which is caused by the increased error rates from state-dependent loss in both OAM and ANG bases, as well as state-dependent phase in the ANG basis. Therefore, to reduce the adverse effects of SDD, a uniform efficiency for all encoding states is desirable, which requires adjusting the efficiencies of low-order states to match the high-order states.

To mitigate this problem, we propose a new pre-compensation protocol to mitigate these adverse effects. Alice first selects one set of states that she is going to use for encoding, and measures the efficiency of state $|L\rangle$. To adjust the efficiencies of all low-order states to match the efficiency of $|L\rangle_A$, she can change the beam radius of each low-order state so that each state has a same divergence angle α_ℓ: $\alpha_\ell \propto (|\ell|+1)/r_{\text{rms}}(0)$, where $r_{\text{rms}}(0)$ is the root-mean-square (rms) beam radius defined by Ref.[85]. That is to say, Alice intentionally increases the loss of the low-order states to reduce the state-dependent loss. Alice then uses these specially prepared OAM states to construct the corresponding ANG basis j. After this, a uniform efficiency has been achieved for both OAM and ANG states, and both the efficiency mismatch and the increased QSER for Bob can be significantly reduced. Since the two bases are orthogonal and mutually unbiased throughout the entire propagation distance, the security analysis of this protocol is identical to the one for the BB84 protocol but with a higher uniform channel loss. We name the approach we have just described *waist pre-compensation* (WPC).

To demonstrate the effectiveness of our WPC protocol, we first use simulation results, with $N_f = 3.96$, to compare the prepared and received states with and without WPC. Figure 3.3(a) shows the simulated intensity and phase distributions of the ANG state $|j=0\rangle$ prepared by Alice in the no-compensation and WPC protocols, while the Figure 3.3(b) shows the corresponding results for the received ANG state $|j=0\rangle$. One can notice that both the intensity and phase profiles for the two protocols are very different at Alice's and Bob's sides. Diffraction distorts the intensity distribution of

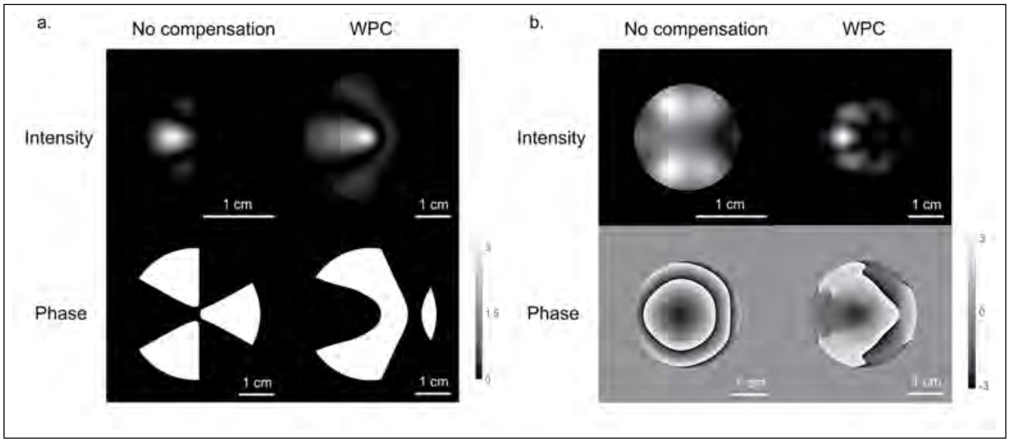

Figure 3.3: (a) and (b): Simulation results of transmitted and received $|j = 0\rangle$ states respectively, both with WPC and without compensation.

the received state in the no-compensation case; after propagating through the link, the one single main lobe on Alice's side, which indicates the angular position and the value of j, becomes two main lobes on Bob's side. Considering that the ANG quantum number j denotes the angular position, the intensity distortion in the no-compensation protocol will lead the failure of identification of the ANG state. In contrast, the intensity profile in the WPC case remains similar even after diffraction. One can still identify the ANG state by finding the angular position of the main lobe.

The simulated crosstalk matrices of no compensation protocol and WPC protocol are shown in Figure 3.4(a) and (b), respectively. It is obvious that in the no compensation case, the SDD gives a nonuniform probability distribution when we measure the ANG states in the OAM spectrum. It has a higher probability for lower order OAM states but a lower probability for the high order OAM components, and nonzero off-diagonal elements in the

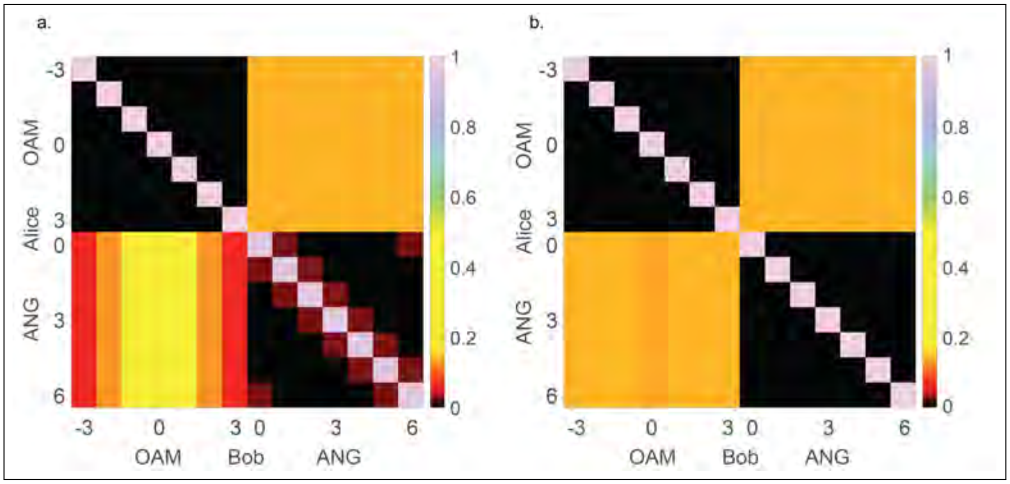

Figure 3.4: (a) and (b): crosstalk matrices of the no-compensation protocol (a) and WPC protocol (b).

ANG spectrum. The fidelity of ANG states shown in Figure 3.4(a) is 95.1% since the N_f is chosen to be 3.96. This fidelity will become worse if the N_f becomes smaller. As a contrast, with the WPC protocol, an almost uniform probability distribution can be found when ANG states are measured in OAM basis. There are no nonzero off-diagonal elements in the ANG basis as well (the fidelity of ANG states in Figure 3.4(b) is 99.99%). Therefore, the simulation results shows the ability of WPC protocol to reduce the adverse effects of SDD.

3.4 Experimental results

To experimentally verify WPC protocol, we use the configuration shown in Figure 3.5 to measure the crosstalk matrix for a Fresnel number product

$N_f = 3.96$ and dimension $d = 7$. A HeNe laser is coupled into a single-mode fiber (SMF) to generate a single spatial mode at 633 nm. The first spatial light modulator (SLM1), together with lenses 2 (L2, $f = 0.75$ m) and 3 (L3, $f = 0.5$ m), are used to generate the desired input states $|\ell\rangle_A$ and $|j\rangle_A$ [58]. Aperture 1 (A1) is used to select the first diffraction order. The distance (Z1 = 3.12 m) between transmitter's aperture (the diameter of A2 is 3.07 mm) and receiver's aperture (the diameter of A3 is 3.25 mm) constitute the link with Fresnel number product $N_f = 3.96$. Both A2 and A3 are implemented by round apertures written onto SLM1 and SLM2 respectively. The second SLM scans the OAM and ANG spectra, and projects the desired state onto the fundamental Gaussian state, which can be coupled into the second SMF. A power meter (PM) is used to measure the transmitted intensity coupled into the second SMF.

To quantitatively show the benefits of WPC protocol, we measure the conditional probability of finding each state received by Bob for each state transmitted by Alice, and display the results in a crosstalk matrix (Figure 3.5(c)). One can see that the diagonal elements, which represents the fidelity of the states, in the ANG basis are larger than the diagonal elements in Figure 3.5(b). The worst fidelity in Figure 3.5(b) is less than 70% while the average fidelity is only 85.8%. As the comparison, the worst fidelity in Figure 3.5(c) is 86.8% and the average fidelity is 93.3%. One should also note that, through the use of WPC, measuring the ANG states in the OAM basis will have a more uniform distribution, which can be found as the bottom left

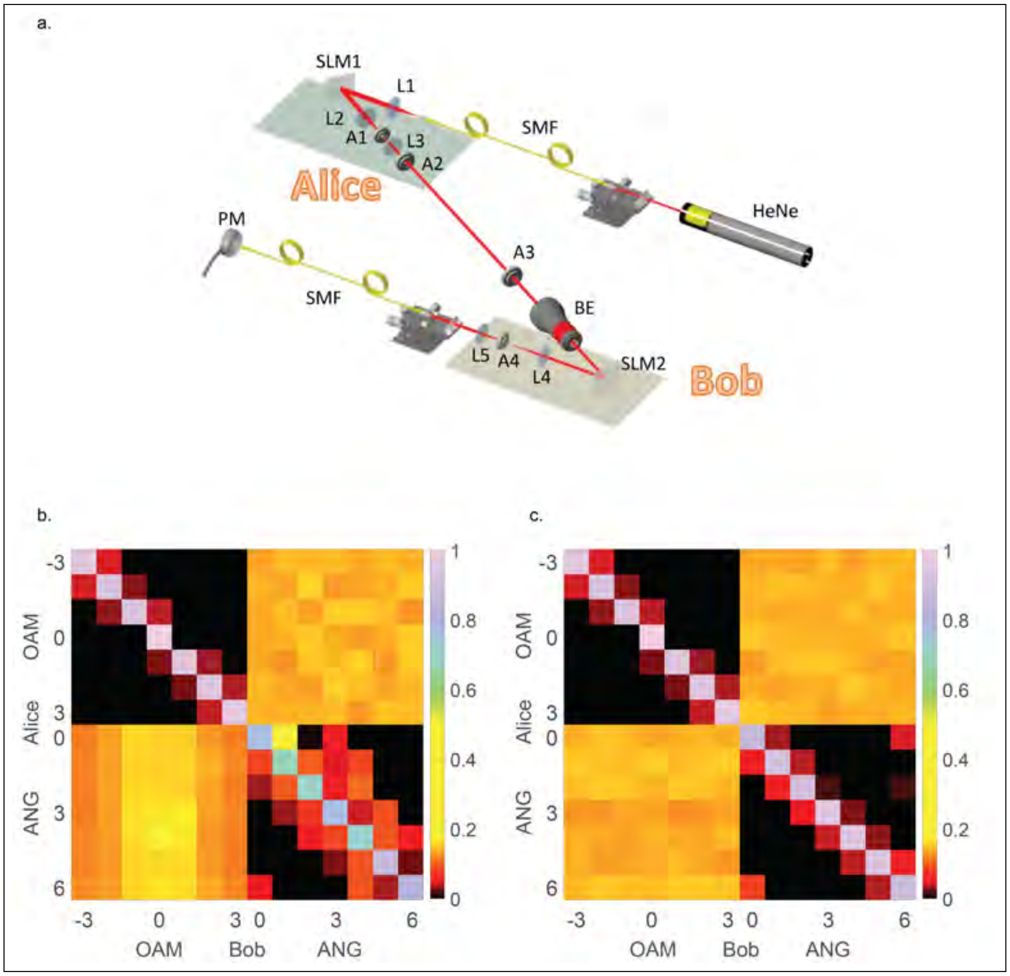

Figure 3.5: (a): The experimental setup. L1 to L5 are lenses while SLM denotes the spatial light modulator. A1-A4 are apertures, and BE is beam expander. Z1 represents the propagation distance from transmitter aperture A2 to the receiver aperture A3. (b): the measured crosstalk matrix with no pre-compensation. (c): the experimental crosstalk matrix of WPC protocol.

corners in Figure 3.5(b) and (c).

Based on the fidelity measured above, we can find that the average QSER measured in the case of no compensation is 14.2% while the average QSER with WPC is 6.7%. The mutual information with WPC protocol equals to 2.56 bits per photon, an improvement over 2.22 bits per photon in the case of no compensation. From the QSER above, we can then find the secure key fraction r_∞ using Eq. (1.11). The secure key density r_∞ is found to be 1.76 bits per received photon with WPC protocol, a significant improvement from 0.89 bits per photon in the no compensation case.

3.5 Discussion and conclusion

Although the WPC protocol will ensure the robustness of the quantum system and provide a higher information encoded per photon, it will lower the overall efficiency and may result in a lower secure key rate because of a lower average transmission efficiency [52]. However, for practical quantum encoding systems with a high dimensionality and low Fresnel number product, the crosstalk introduced by SDD can be much larger than in the ideal case. The simulated comparison of the secure key rate per transmitted photon between WPC protocol and no compensation protocol with different error rates from external errors are shown in Figure 3.6 as a function of Fresnel number product N_f. For a given system with fixed transmitting and receiving apertures, N_f is inversely proportional to the transmission distance z. Therefore, a small N_f usually indicates a larger z. Under the perfect condition where the external error rate is 0 (Figure 3.6(a)), we see that WPC protocol can significantly improve the performance of high-dimensional QKD systems in realistic links with small N_f. The advantage of WPC still exists in the presence of external errors, i.e. a noisy system (10% error rate in Figure 3.6(b)). Even though in some cases, the no compensation protocol has a better key rate when the external error rate is 10%, implementing WPC is still advantageous when the encoding space is large. This is because when the dimensionality of the encoding space is small, the SDD induced efficiency and phase mismatch between different states is negligible. Therefore, the use of WPC will have a little improvement. However, when dimensionality goes larger, which is desirable in realistic QKD systems, the advantage of WPC becomes more significant. Thus, intentionally sacrificing some efficiency for low-order states to get a lower but uniform efficiency can significantly benefit the system.

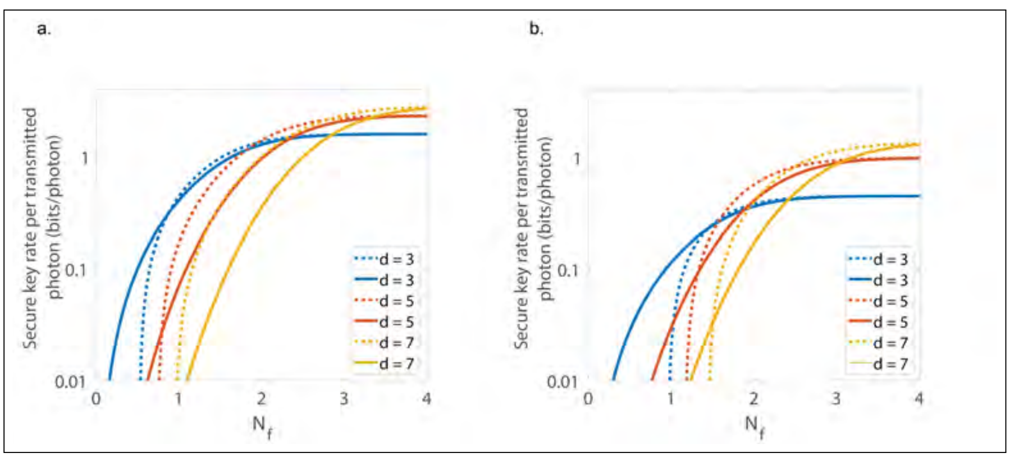

Figure 3.6: (a) and (b): Simulated secure key rate per transmitted photon as a function of Fresnel number product N_f with 0% and 10% external errors respectively. The solid lines represent the secure key rate using WPC protocol while the dashed lines represent the secure key rate with no compensation.

Another concern regarding the WPC protocol is how practical it will be in a realistic QKD scenario. As we discussed above, in most cases, the WPC protocol is superior to no compensation protocols only when N_f is limited. In realistic scenarios, most current free-space QKD systems have Fresnel number product less than 1, for example the cross-ocean link and satellite-to-ground system ($N_f = 0.23$) [95, 96]. Thus the WPC protocol could be useful in optimizing the performance of future global high-dimensional QKD systems. Furthermore, implementing WPC protocol is simple: one only needs to take the N_f of the system into consideration, and employ the optimal set of beam waists, which requires no extra apparatus.

At the end of the discussion, we need to emphasize that the entire analysis is based on the assumption of OAM encoding and circular apertures. However, SDD is expected to be a problem for any type of spatial-mode encoding, and for a given system, we can always find a set of eigenstates with uniform transmission efficiency. Therefore, our new protocol is generic for high-dimensional quantum encoding scenarios utilizing spatial degrees of freedom [8, 14]. Furthermore, all analysis exclude the effect of atmospheric turbulence. For realistic free-space QKD systems, one has to include the turbulence into consideration as well.

Chapter 4

Mitigating atmospheric turbulence in free-space OAM QKD using adaptive optics

From our discussion in Chapter 2, we have shown that atmospheric turbulence can significantly reduce the information capacity. Therefore, a turbulence correction system is always necessary in realistic free-space OAM QKD systems. However, effectively mitigating the adverse effects of atmospheric turbulence is a persistent challenge in OAM QKD systems operating over free-space communication channels. Although numerous methods have been proposed and demonstrated to reduce the defects induced by turbulence, adaptive optics (AO) is still the most promising one which can provide real-time correction without sacrificing any information capacity. Unfortunately, previous researches of using AO to improve the performance of OAM QKD mainly focus on static simulated turbulence, which are incompatible with real application scenarios. Therefore, to build a real outdoor OAM QKD link, we have to investigate the performance of OAM QKD in atmospheric turbulence (not the simulated static turbulence) with real-time AO correction. In order to provide a comprehensive study, two configurations are researched: a lab-scale link with controllable turbulence, and a 340 m long cross-campus link with dynamic atmospheric turbulence. We show that, even our AO system provides a limited correction, it is possible to mitigate the errors induced by weak turbulence and establish a secure channel. Meanwhile, our experimental results suggest that an advanced AO system with fine beam tracking, reliable beam stabilization, precise wavefront sensing, and accurate wavefront correction is necessary to adequately correct turbulence-induced error. We also propose and demonstrate different solutions to improve the performance of OAM QKD with turbulence, which could enable the possibility of OAM encoding in strong turbulence.

4.1 Introduction

Since the information is carried by the phase profile, OAM states are vulnerable to atmospheric turbulence as what we have shown in Chapter 2. Even though the behavior of OAM states in a turbulent channel has been studied both theoretically and experimentally [9, 38, 64, 73, 74, 75, 76, 77, 78, 82, 97, 98, 99, 100, 101, 102, 103, 104], realizing high-dimensional OAM-based QKD still remains challenging because of inadequate correction of realistic atmospheric turbulence.

To reduce the crosstalk induced by turbulence, most works either rely on post-selection of data or increasing the mode spacing (i.e. not using successive states for encoding) [38, 87, 98]. For a given free-space link, although these methods can reduce the QSER, they lead to a reduction of photon rate and size of encoding space. Therefore, the advantage of high-dimensional encoding on information capacity cannot be fully realized. Moreover, for an OAM encoding space with mode spacing equal to one, the OAM basis and ANG basis form the MUBs. A high-fidelity sorter for efficiently measuring these MUBs has been developed, and its effectiveness has been demonstrated in QKD systems as well [12, 52, 61]. However, its counterparts for mode spacing larger than one have not yet been demonstrated, and an inefficient measurement device may introduce additional security loopholes [105]. Therefore, an efficient approach which can both take the full advantages of high-dimensional encoding and reduce the crosstalk from atmospheric turbulence is still under investigation.

Conceptually, the simplest technique for overcoming turbulence-induced errors is to use AO to correct errors without sacrificing the benefits of using the high-dimensional encoding QKD system. However, since OAM states are very sensitive to wavefront errors, any imperfect correction may actually lead to an increase rather than a decrease in QSER, and hence the failure of QKD system. Most previous experimental works focused on correcting static turbulence simulated by single or multiple random phase screens [9, 74, 76, 77, 78, 82, 97, 99, 100, 104]. This is based on the fact that the time scale of the atmospheric turbulence, which is usually much longer than the travel time of laser pulses, can be considered as static. However, dynamically correcting realistic turbulence will lead to additional challenges which cannot be revealed in a static system. In addition, some theoretical simulations predict that a simple AO system may not be adequate for turbulence correction [67, 68, 106]. Therefore, under real dynamic turbulence, using AO systems to correct errors in OAM states remains very challenging, and the performance of AO correction in real atmospheric turbulence is still unknown and needs to be investigated.

4.2 Lab-scale link under controllable turbulence

To quantitatively investigate the performance of AO correction on an OAM QKD system, we first build a lab-scale link with a controllable source of turbulence. The experimental setup is shown in Figure 4.1. Alice prepares her states using a spatial light modulator (SLM) and a 633 nm He-Ne laser. The laser is first coupled into a single mode fiber (SMF) to generate a fundamental Gaussian state ($\ell = 0$), which is then collimated with an objective and illuminates SLM1 (SDE1024 from Cambridge Correlators Ltd). A pair of lenses ($f_1 = 0.75$ m and $f_2 = 0.5$ m) together with an iris are used to select the desired state of light, carried by the first-order diffraction from the SLM. A polarizer and a half-wave plate (HWP1) after these lenses are used to prepare four different polarization states: horizontal ($|H\rangle$), verti-

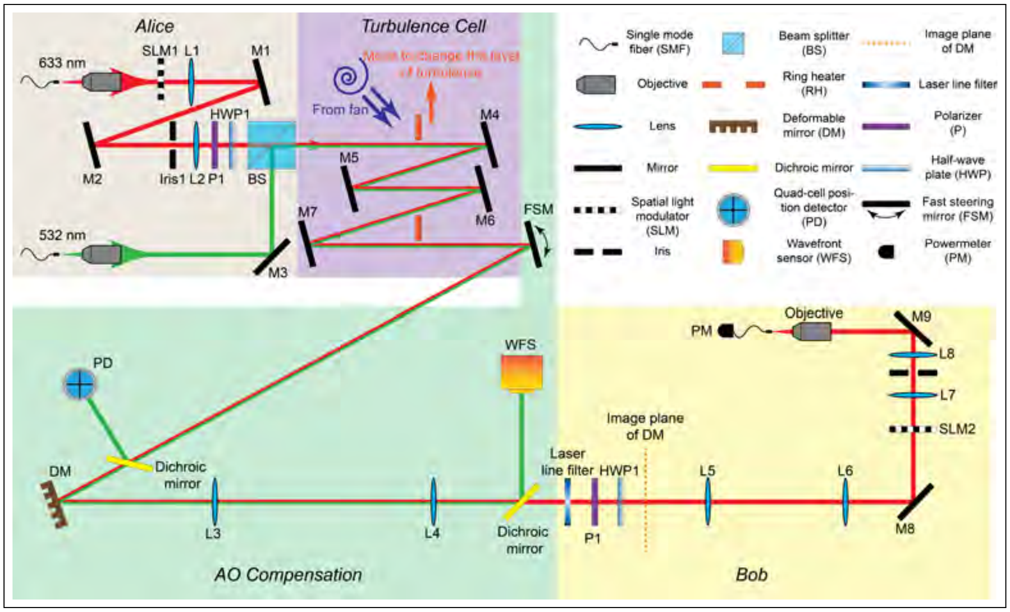

Figure 4.1: The configuration of the lab-scale link with a controllable turbulence cell. Both signal and beacon beams go through the center of the RH. The size of the signal beam is selected to cover the central part of the DM (3×3 actuators) to avoid the cutoff from the edges. The size of the beacon beam overfills the DM aperture to provide a precise estimation of turbulence across the DM. The polarization of the signal beam is controlled by a polarizer to encode information while the polarization of the beacon beam is fixed in $|H\rangle$ state.

cal ($|V\rangle$), diagonal ($|D\rangle$) and anti-diagonal ($|A\rangle$). The beacon beam, which comes from a 532 nm green laser, is collimated using an aspheric lens from a SMF. Since the atmospheric turbulence can be considered as nondispersive in visible range, the beacon beam should have similar distortion to the 633 nm beam. Therefore, using a beacon beam whose wavelength is 100 nm shorter than signal beam is acceptable [67, 107, 108, 109]. The signal beam (the beam encoded by SLM1) is combined with the beacon beam through the use of a beam splitter (BS). Afterwards, both beams propagate collinearly through the turbulent channel consisting of a turbulence cell (TC) and three mirrors. The TC is a ring heater (RH) blown on by a fan. We adjust the level of turbulence by changing three parameters: the temperature of RH, the fan speed and the number of times that the beams go through the TC. The separation between BS and RH is 1.5 m while the separations between RH and the first two mirrors (M4 and M5) are both 0.15 m. For the strongest turbulence, the beams go through the TC four times and are then reflected to the deformable mirror (DM) by a fast steering mirror (FSM, OIM5002 from Optics In Motion LLC). For the weakest turbulence, RH is moved 0.3 m away from the beams so that the beams simply bypass the RH but still experience some turbulence from the edge of RH.

The AO compensation system consists of two parts. The first part has a FSM and a quad-cell position detector (PD), and is used to correct the beam wander induced by the 2nd and 3rd Zernike polynomials (in Noll index, i.e. tip and tilt). To redirect part of the green beacon beam to PD, a 488 nm 50/50 non-polarizing BS (#48-217 from Edmund Optics) is used as a dichroic mirror, which leads to 7.40% loss in the signal beam. Since only one set of FSM and PD is involved, either x-y position or the propagation direction on the DM, i.e. the x-y momentum, can be corrected. In our configuration, the beam position on the DM is corrected but not the propagation direction. To minimize the tip-tilt error on DM induced by the FSM, the separation between FSM and PD is much larger than the separation between FSM and TC. That is to say, the FSM is in the near-field of turbulence while the PD is in the far field. The second part of the AO system consists of a Shack-Hartmann wavefront sensor (WFS, WFS20-7AR from Thorlabs) and a DM with 32 actuators (DM32-35-UM01 from Boston Micromachine). WFS is working in the high-speed mode with 23×23 microlens in use, and the measured Zernike coefficients are limited to the first 15 terms to give the best performance. The selection of this optimal specification will be discussed later. The compensation control is performed by Thorlabs AO kit software (Version 4.40). To get the optimal wavefront measurement, the beams at DM plane are imaged onto WFS plane using two Thorlabs best-form spherical singlet lenses (f_3 = 0.20 m and f_4 = 0.15 m). Before the WFS, a 605 nm dichroic mirror (#34-740 from Edmund Optics) is used to reflect the green beacon beam but transmit the red signal beam. To reduce the noise from beacon beam [15], a laser line filter (#68-943 from Edmund Optics) at 633 nm is used to filter out the residual green light. The DM plane is then imaged onto SLM2 using another imaging system, consisting of two Thorlabs best form spherical singlet lenses (f_5 = 0.2 m and f_6 = 0.2 m), to perform projective measurements [6]. To measure the polarization degree of freedom, a polarizer and a half-wave plate (HWP2) are used after the laser line filter. HWP2 is used to rotate the polarization state ($|H\rangle$, $|V\rangle$, $|D\rangle$ or $|A\rangle$, which can be used as another degree of freedom in hybrid encoding and will be discussed later) to $|H\rangle$ since liquid crystal SLM only affects horizontally polarized light.

To quantify the level of turbulence, we still use the quantity D/r_0 to describe the level of turbulence, where D is the beam diameter because the beacon Gaussian beam underfills the collection aperture [71, 110]. In our experimental setup, the OAM states with quantum number ℓ from -2 to 2 comprise our encoding space with dimension $d = 5$. The r_0 under different levels of turbulence are estimated from the beam wander at the receiver side by analyzing the centroid of the received Gaussian states [87]. This leads to an experimental D/r_0 ranging from 0.11 to 3.06, which corresponds to turbulence levels ranging from weak turbulence to strong turbulence.

We measure the crosstalk matrices between the prepared and received states under different turbulence conditions, and calculate the measured fidelity (F) as a function of turbulence strength D/r_0, which are shown in Figure 4.2. With the turbulence turned off, we measure an average fidelity $F = 93.69\%$ of the MUBs (the blue dot in Figure 4.2(c)). The fidelity of the OAM basis and ANG basis can be found in Figure 4.2(a) and (b) respectively. Each measurement takes 1.5 mins so that the total measurement time for the average fidelity of the MUBs under one specific level of turbulence is about 150 mins. The measured fidelity of the MUBs is above the fidelity threshold $F = 79.01\%$ for this $d = 5$ system, which indicates that a secure quantum channel can be established [53, 55]. As D/r_0 increases, F drops quickly due to an increase in fluctuation levels, and the fidelity in the OAM basis matches well with the theoretical prediction $F = 1 - [1 + c(D/r_0)^2]^{-1/2}$, where coefficient c is 3.404 for the no turbulence case [73]. The yellow and

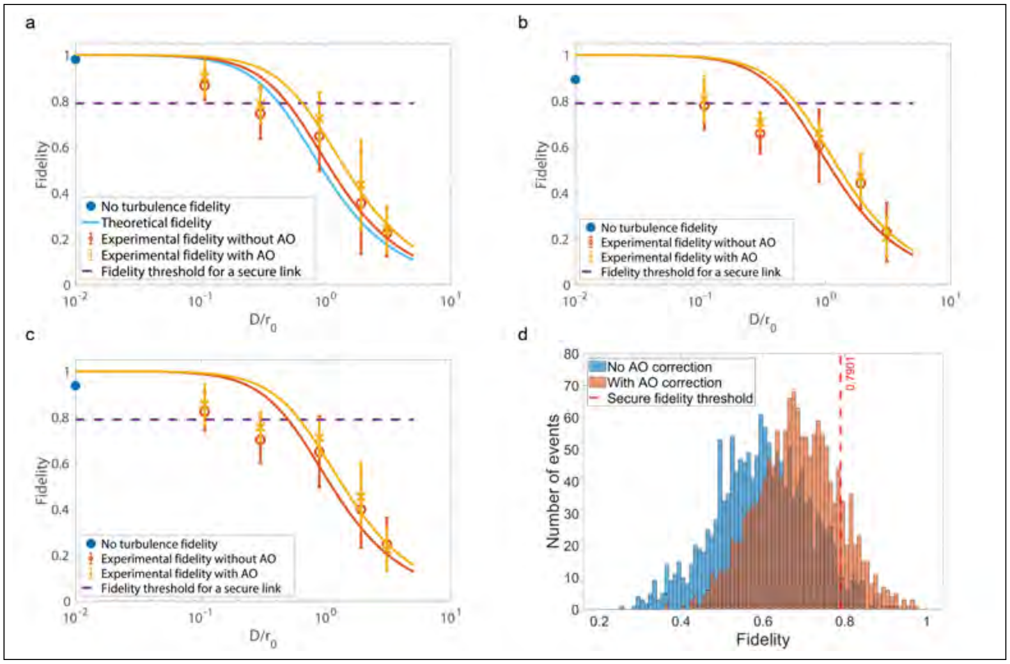

Figure 4.2: Measured fidelity of lab-scale OAM QKD as functions of turbulence strength and time. (a): measured fidelity of the OAM basis. (b): measured fidelity of the ANG basis. (c): measured fidelity of the MUBs which is the average of (a) and (b). The data point with $D/r_0 = 0.01$ corresponds to the no turbulence case. All the yellow and red curves are least-square fitting results of the measured data using the same model with different coefficients c. All the error bars are the measured standard deviation of the fidelity distribution over the measurement time. Each error bar is the average standard deviation of all states in the corresponding basis. One example of the fidelity histogram distributions is shown in (d). The standard deviation without AO correction is 11.24%. When AO is turned on, this is reduced to 8.68%. As a comparison, the measurement uncertainty without turbulence is 1.46%, which is mainly induced by the laser power fluctuation. (d): histogram of the fidelity of the OAM state $\ell = 1$ with and without AO correction. D/r_0 is 0.884.

red curves are least square fitting results of the experimental data. Even under weak turbulence with $D/r_0 = 0.11$, the average fidelity in the ANG basis (78.04%) is below the threshold. After we turn on the AO, the fidelity is improved to 80.07% in the ANG basis and the fidelity in the OAM basis is improved from 86.69% to 90.35%. Therefore, a secure channel, which could not have been otherwise established, becomes possible after the AO correction is applied.

The modest improvement in fidelity mainly comes from the limited performance of the AO with an insufficient number of micromirrors on DM and the trade-off between speed and accuracy of the WFS. Our DM only has 32 actuators (6×6 square grid without corners). To avoid being cutoff by the edge, the signal beams are aligned to fall within only the central actuators (3×3 actuators for $|\ell = 1\rangle$) while the beacon beam fills the entire aperture. The inadequate number of actuators can result in a low complexity of the wavefront that can be corrected and a poor accuracy, which means that only the first few orders of Zernike terms can be corrected with limited precision.

The trade-off between correction speed and accuracy exists in most AO systems. To provide a fast wavefront measurement, our WFS is set to operate in the high-speed mode. This specific mode can provide a measurement speed up to kHz levels by sacrificing the number of lenslets used to estimate the Zernike coefficients, which indicates that a more accurate wavefront measurement leads to a slower speed of AO compensation. In our case, WFS is working at 350 Hz, which is also the speed of our AO system according to the manual of our AO kit (AOK5-UM01-Manual). To optimize the performance, one needs to first measure the bandwidth of turbulence to select an AO speed that is fast enough to sample the turbulence. This goal can be achieved by measuring the fidelity fluctuations as a function of time. For an AO system to be effective in compensating for turbulence, its speed must exceed the fluctuation rate of the atmosphere, a frequency around 60 Hz known as the Greenwood frequency [111, 112, 113, 114, 115]. Our AO system, with a sampling speed of 350 Hz, satisfies this condition. One also needs to consider the complexity of the Zernike terms that can be corrected by the DM. If the DM has a small number of actuators, one can limit the order of Zernikes measured by the WFS to further improve the speed. Otherwise, the number of Zernike terms measured by WFS should be large enough to avoid the waste of DM correction power. From the number of actuators on the DM, the speed of WFS, and the corresponding number of lenslets, one can determine the beam sizes on the WFS and then use a telescope to relay the field at DM to WFS. Through this procedure, the optimal combination of AO speed and the number of spots on WFS can be found, which will provide the best performance for each specific system. In our case, since the complexity of the DM (6×6 actuators) limits the performance of our AO system, the number of pixels of the WFS is set to a lower level (23×23 lenslets) to provide a faster sampling rate.

Another observation is that for a given AO system, the effect of AO compensation varies with the level of turbulence. For our system, the optimal performance occurs when the turbulence is moderate ($D/r_0 = 0.884$). As shown in Figure 4.2(d), when the correction is enabled, the average fidelity of the OAM state $|\ell = 1\rangle$ is improved from 64.68% to 72.24%, and the standard deviation is reduced from 11.24% to 8.68% as shown in Figure 4.2(d). The probability of events which have an instantaneous fidelity larger than the threshold is increased by a factor of 3.48. In contrast, the improvement in either weak turbulence or strong turbulence is small. This is caused by different reasons in weak turbulence case and strong turbulence case.

When the turbulence is weak, the Zernike terms that introduce the majority of the error are tip and tilt, and the high-order terms are usually small and may be negligible compared to the WFS noise. Even though tip and tilt can in principle be easily corrected by two sets of FSM and PD, only one set is involved in our system. Therefore, the propagation direction of the beams leaving the FSM is not under control. After being imaged onto the DM plane, the error in the propagation direction should be corrected by the DM. Apart from tip and tilt, other aberrations in the weak turbulence are not so strong that thus not much error needs to be corrected. This combination of errors seems easy to be corrected. However, due to the inadequate number of actuators on the DM and the noise of the WFS, the AO may introduce some errors to the system that limits the potential fidelity improvement.

When strong or deep turbulence (extremely strong turbulence) is present, the high-order Zernike terms contribute more to the errors compared to low-order terms. Not only does the transverse phase profile get disturbed, but also the intensity profile is highly distorted. For example, when strong astigmatism (the 5th and 6th Zernike polynominals in Noll index) is present, the phase singularity at the center of OAM states $|\ell\rangle$ will get fractured into ℓ new singularities, and the OAM states will get stretched to elliptical shapes. Similar distortion also happens in our cross-campus link as shown in Figure 4.4(a). This phenomenon is observed when D/r_0 equals to 1.90 and 3.06, which indicates that the turbulence is strong. In such a case, one simple AO system cannot sufficiently correct the errors in both phase and intensity profiles. Moreover, considering the inadequate number of actuators on the DM, the complexity of the wavefront that the DM can provide is not good enough to correct high-order terms. Therefore, an advanced AO system including multiple conjugate DMs and WFS with fast speed and high resolution is essential to correct strong and deep turbulence, while the exact specifications depends on the level of turbulence [106]. In contrast, for moderate turbulence, Zernike coefficients are usually large enough so that the WFS can provide a precise measurement, and the DM can also provide a relatively accurate correction. In the meantime, the wavefront complexity is acceptable. Considering both effects, our AO correction has adequate performance in the moderate turbulence regime.

4.3 Free-space link across the UR campus

We next investigate the performance of AO compensation in a 340 m long free-space link across the University of Rochester (UR). The experimental setup is shown in Figure 4.3. The state preparation stage is the same as the

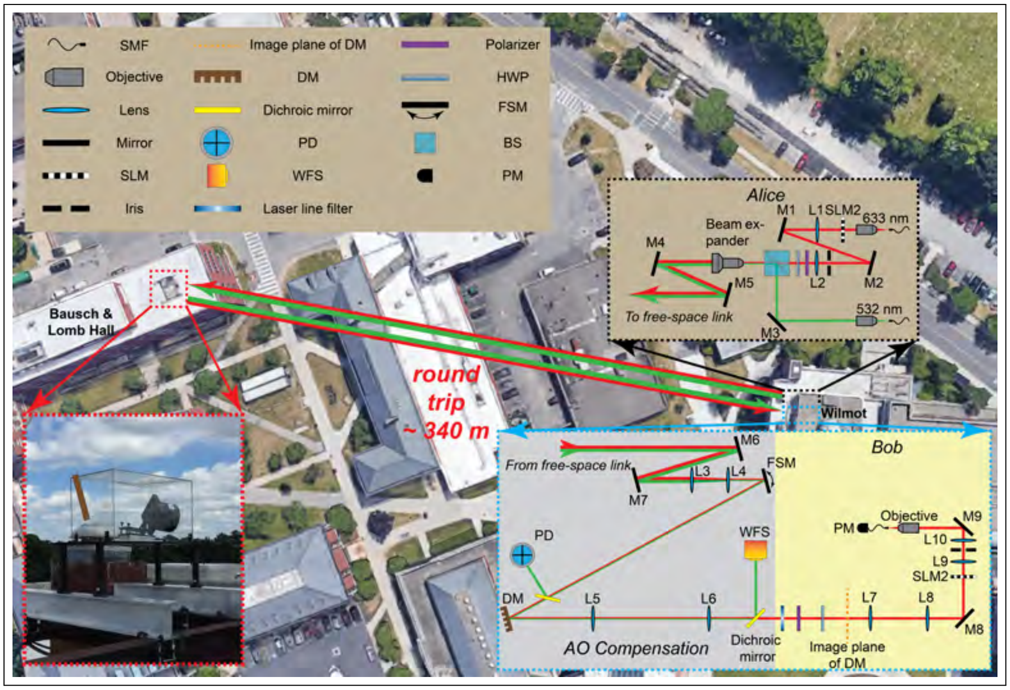

Figure 4.3: The configuration of a 340 m long cross-campus link. Both Alice and Bob are on the optical table. Since the turbulence in the cross-campus link is not controllable, the turbulence structure number varies between 5.4×10^{-15} m$^{-2/3}$ and 3.2×10^{-14} m$^{-2/3}$.

setup shown in Figure 4.1. After BS, the combined beam is expanded using an achromatic 3× beam expander (GBE03-A from Thorlabs) and launched to the roof of Bausch & Lomb Hall through the use of one pair of mirrors (M4 and M5). As shown in the photograph, the hollow retroreflector (#49-672 from Edmund Optics) and the rotation stage are mounted on an optical breadboard, which is then mounted on the steel and aluminum frames on the roof. To protect the retroreflector, a double protection scheme is used. A high efficiency AR coated protection window is used to seal the front aperture of the retroreflector, which can prevent the formation of dew on the mirrors. The entire system, which is about 35 m above the ground, is also covered by an acrylic protection box (the front side of this box is replaced with a high efficiency window (#43-975 from Edmund Optics)) to protect the retroreflector and stage from weather. The reflected beams are collected by a pair of mirrors (3 inch clear aperture, M6 and M7), giving a Fresnel number N_f of the system equal to 4.89. An achromatic lens with 3 inch diameter (L3, $f_3 = 200$ mm) and a negative achromatic lens (L4, $f_4 = -40$ mm) are used to reduce the beam size. After this, the beams are sent to the AO system, which is almost the same as what is shown in Figure 4.1 except that the DM has 140 actuators (12×12 without corners, DM140A-35-UM01 from Boston Micromachine). The large DM has more actuators which can provide a better accuracy and complexity in the wavefront correction. To match the size of the clear aperture of DM and WFS, the beam size is reduced by several imaging systems which are not shown in the figure. All the lenses used in the imaging systems are best form spherical singlet lenses to reduce the spherical aberration.

The turbulence structure number C_n^2 of our cross-campus link is estimated by calculating the beam wander of the returned $|\ell\rangle$ beam, which yields a C_n^2 from 5.4×10^{-15} $\mathrm{m}^{-2/3}$ to 3.2×10^{-14} $\mathrm{m}^{-2/3}$. The corresponding D/r_0 is from 1.03 to 2.98. This indicates a moderate to strong turbulence [69]. The intensity profiles of the prepared and received states under a turbulence strength $C_n^2 = 1.9 \times 10^{-14}$ $\mathrm{m}^{-2/3}$ are shown in Figure 4.4(a), and the corresponding

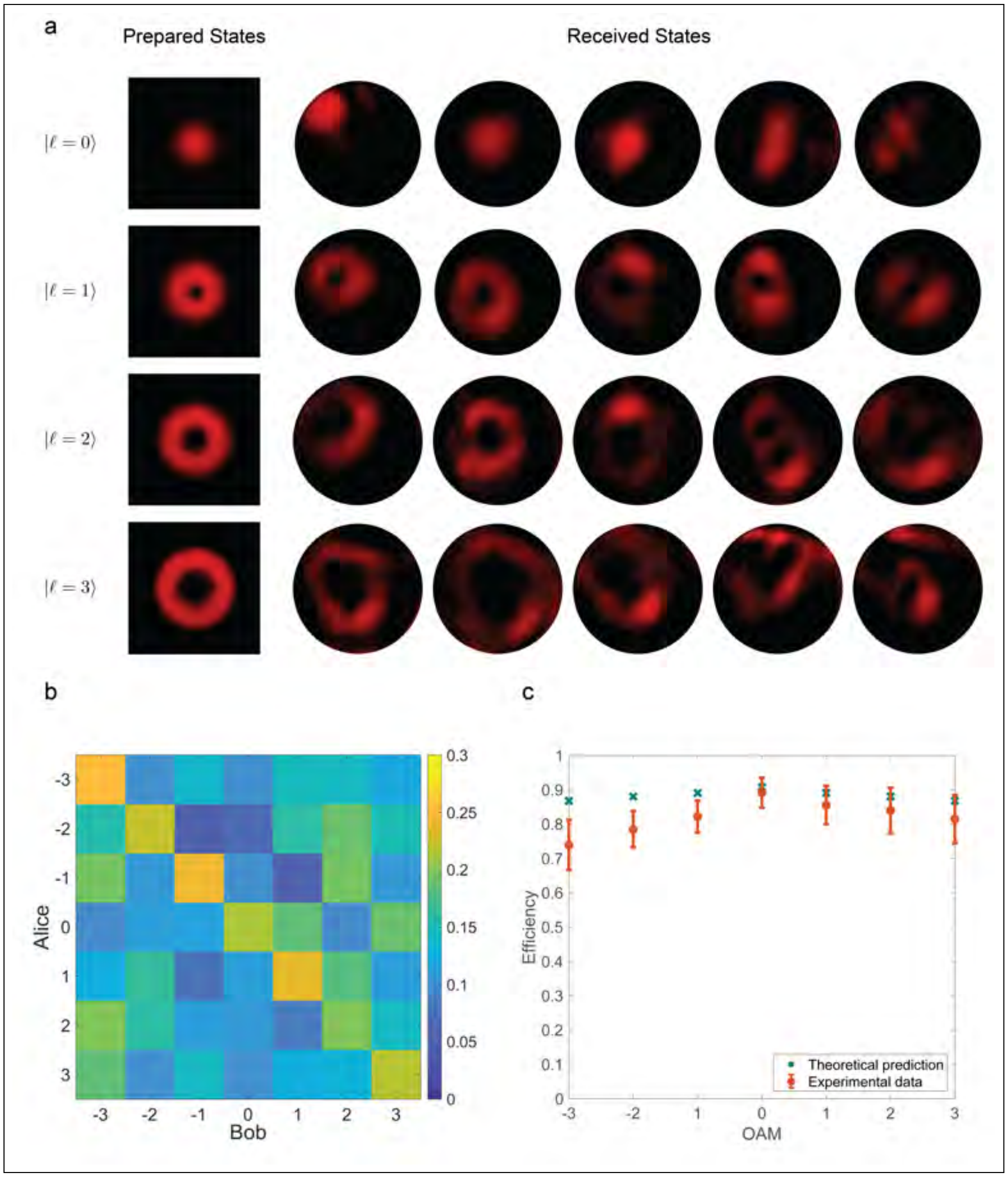

Figure 4.4: (a): Examples of prepared and received states in the cross-campus link with different OAM values. (b): crosstalk matrix of the OAM basis after AO correction. (c): The theoretical and measured mode transmission efficiency. The error bars correspond to the standard deviation in transmission efficiencies.

D/r_0 is 2.18. Note that the images of the prepared states have been scaled up by a factor of 3. The images of the received states only show the field in the collection aperture, and the intensities of the received $|\ell = 2, 3\rangle$ states are enhanced by a factor of 1.5. The intensity profiles are strongly distorted by turbulence so that the original donut shapes of the OAM states are not maintained. One can also see the effects induced by different Zernike terms from these images. For example, the first column of the received states have relatively good intensity profiles but are not at the center of receiver's aperture. These shifts are the result of tip and tilt. The received states in the 4th column show the effects induced by astigmatism. The received states are elongated into elliptical shapes, and the phase singularities are fractured into multiple vortices. In scenarios where multiple Zernike terms dominate the effect, the received states can be highly distorted leading to indistinguishable intensity profiles. For instance, as shown in the 5th column, the $|\ell = 0\rangle$ and $|\ell = 1\rangle$ states are split into 2 separate spots so that the two intensity profiles are similar to each other. To quantitatively show the statistic of such cases, we define the charge number of the received OAM states. This quantity denotes the number of phase singularities in the received states. When the state is so distorted as to break down, the charge number will become 0. After carefully analyzing all the received states, we find that only 0.11% of the received $|\ell = 0\rangle$ has a charge number more than 0. In principle, the received Gaussian state should have 0 charge number. Therefore, even though very rare under this turbulence level, Gaussian state can possibly break down into a non-Gaussian shape (as shown in the top right figure of Figure 4.4(a)). For $|\ell = 1\rangle$, 22.21% of the received states has a charge number equal to 0. This number becomes 49.52% and 78.74% for $|\ell = 2, 3\rangle$ respectively. This surprising result comes from the fact that when the beam wander is strong, beams are easily cut off by the aperture due to the lack of precise beam tracking. When the cut off happens, the donut shape of OAM states cannot be maintained and thus the phase profile will be incomplete, which will lead to the failure of OAM measurement.

The crosstalk matrix and the measured transmission efficiency are shown in Figure 4.4(b) and (c). With AO compensation, the fidelity in the OAM basis is only improved from 19.74% to 22.57% which is far below the fidelity threshold (76.30% for $d = 7$ systems), and the improvement in fidelity provided by AO is modest compared to the lab-scale data with a similar turbulence level (for $D/r_0 = 1.90$, the lab-scale fidelity can be improved from 35.53% to 43.47%). Meanwhile, the transmission efficiency of OAM states, especially the high order terms, also fluctuates significantly. As shown in Figure 4.4(c), the theoretical efficiency of the $|\ell = 3\rangle$ state, including the effect of mode-dependent diffraction, should be 86.83%. However, the measured efficiency in the cross-campus link under AO correction is only 73.95% with 7.32% standard deviation, which is 12.88% lower than the expected efficiency. As a comparison, the measured efficiency of a Gaussian state is 89.21% with little fluctuation, which is only 1.58% lower than the theoretical efficiency predicted by the simulation. Considering that we are not in the strong or deep turbulence regimes, the low link efficiency with considerable fluctuations and modest improvements with AO are mainly caused by the distorted beacon beam, finite collection aperture size and mode-dependent diffraction [6, 66]. These effects are only observed in the cross-campus link since the lab-scale link has a sufficiently large Fresnel number product (in our case the $N_f > 270$ in the lab-scale link) and a more stable turbulence strength. The breakdown of the Gaussian state is usually observed in strong and deep turbulence regime but is also occasionally observed in our cross-campus link (the last photograph of the received $|\ell = 0\rangle$ state in Figure 4.4(a)), which leads to the failure of precise beam tracking for low Fresnel number channels. This will then lead to a low link efficiency and a problematic tip-tilt correction, which will introduce additional errors. This effect becomes more severe for a limited Fresnel number of the link due to finite collection aperture and long propagation distance. In this case, a high-order OAM state arriving at the receiver's aperture will be have a much larger size than the beacon beam due to mode-dependent diffraction. In our case, due to the spherical aberration and defocus, the size of the $|\ell = 3\rangle$ states can vary from 6 cm to more than 7.62 cm, which exceeds the size of collection aperture (effective size is less than 7.62 cm). This indicates that, for a given Fried parameter r_0, higher order OAM states with larger cross sections are more distorted than the lower order states. Therefore, a slight mistracking caused by a distorted beacon beam will lead to the cutoff of high-order OAM state and hence a lower efficiency and a much larger error. Meanwhile, due to the mode-dependent diffraction, the size of beacon beam (usually in $|\ell = 0\rangle$ state) cannot match the size of high-order states across the whole link. This indicates that the beacon beam cannot capture all the aberrations that the high-order states experience in the link, which leads to an inefficient and inaccurate AO correction. To solve this, one may need to introduce new protocols to mitigate mode-dependent diffraction, for example as discussed in previous chapter.

After the analysis above, we can find that, for free-space OAM QKD channels, one distinctive requirement is the fine beam tracking system with a reliable beam stabilization, which usually involves multiple FSMs and PDs. Different from conventional polarization or time-bin encoding systems where beam tracking and stabilization system only contribute to the transmission efficiency, such a system can affect multiple factors in OAM QKD systems. As what we discuss in the previous chapters and above, a successful measurement of OAM states has two conditions: 1. the phase singularity has to be on optical axis; 2. the phase profile, i.e. the helical phase structure, has to be complete. When such a beam tracking and stabilization system is missing, for example in our configuration, the received OAM states will wander around in the receiving aperture (Figure 4.4(a))). When this beam wander is not strong, only condition 1 will contribute to the failure measurement of OAM states. If the beam wander is so strong that the finite-sized receiving aperture cuts off OAM states, both condition 1 and 2 result in the poor measured fidelity of OAM states. Therefore, apart from the enhanced transmission efficiency, a precise beam tracking and stabilization system will significantly improve the fidelity of received OAM states.

However, it is worth noting that a precise beam tracking is still not sufficient to correct the turbulence-induced errors since, in principle, it can only correct lowest Zernike terms (tip and tilt). As we show in the lab-scale link, high-order Zernike terms, which can only be corrected by multiple DMs and WFSs, become dominant under moderate or strong turbulence. That is to say, an advanced AO system should include two basic compositions: at least one set of beam stabilization and tracking system, and one set of advanced wavefront correction system consisting of multiple conjugate DMs and WFSs [67, 68, 106].

4.4 Additional approaches and discussion

As what we discuss above, a simple AO system cannot provide sufficient correction of OAM QKD system, and additional approaches are necessary to further improve the performance.

One widely used solution is increasing the mode spacing in the encoding space, and we will discuss the effectiveness and limitation of this approach. As shown in Figure 4.5, by simply increasing the mode spacing to 2, i.e. encode information with $|\ell = -4, -2, 0, 2, 4\rangle$ states, we can improve the average fidelity from 35.53% to 45.72% under the turbulence level $D/r_0 = 1.90$ even without AO correction. If AO correction is introduced, the average fidelity can be improved from 43.47 to 57.54%. This improvement can be further enhanced if the mode spacing increases. Under the same turbulence, when the mode spacing becomes 4 (i.e. using $|\ell = -4\rangle$, $|\ell = 0\rangle$ and $|\ell = 4\rangle$ states), the fidelity can be improved from 71.49% to 84.33% in a $d = 3$ system, which is above the fidelity threshold ($F = 84.05\%$) and a secure channel is achievable (not shown in the figure).

However, this solution has two limitations. For a fixed dimension d, a large mode spacing involves states with larger $|\ell|$, which will sacrifice the information capacity and exacerbate the defects induced by mode-dependent diffraction [6]. As what we discuss in the first and second chapter, the information capacity of a given link is fixed so that the maximal number of states supported by this link is limited. Thus, increasing the mode spacing will inevitably reduce the number of states available for encoding, which further leads to a lower information capacity. Furthermore, due to the mode-dependent diffraction, high-order states will suffer more turbulence due to the larger beam size. This will result in a lower data rate compared to an encoding system with the same dimensionality but consecutive states. The other limitation is the lack of an efficient sorter to measure the corresponding MUBs. Even though a generic quantum sorter for an arbitrary system has been proposed, implementing such an idea usually requires multiple phase screens, which results in a low overall efficiency and hence a lower key rate and more security loopholes [116, 117]. Even though this approach can alleviate the crosstalk problem to some extent, it might be unsuited for OAM encoding unless these limitations are solved.

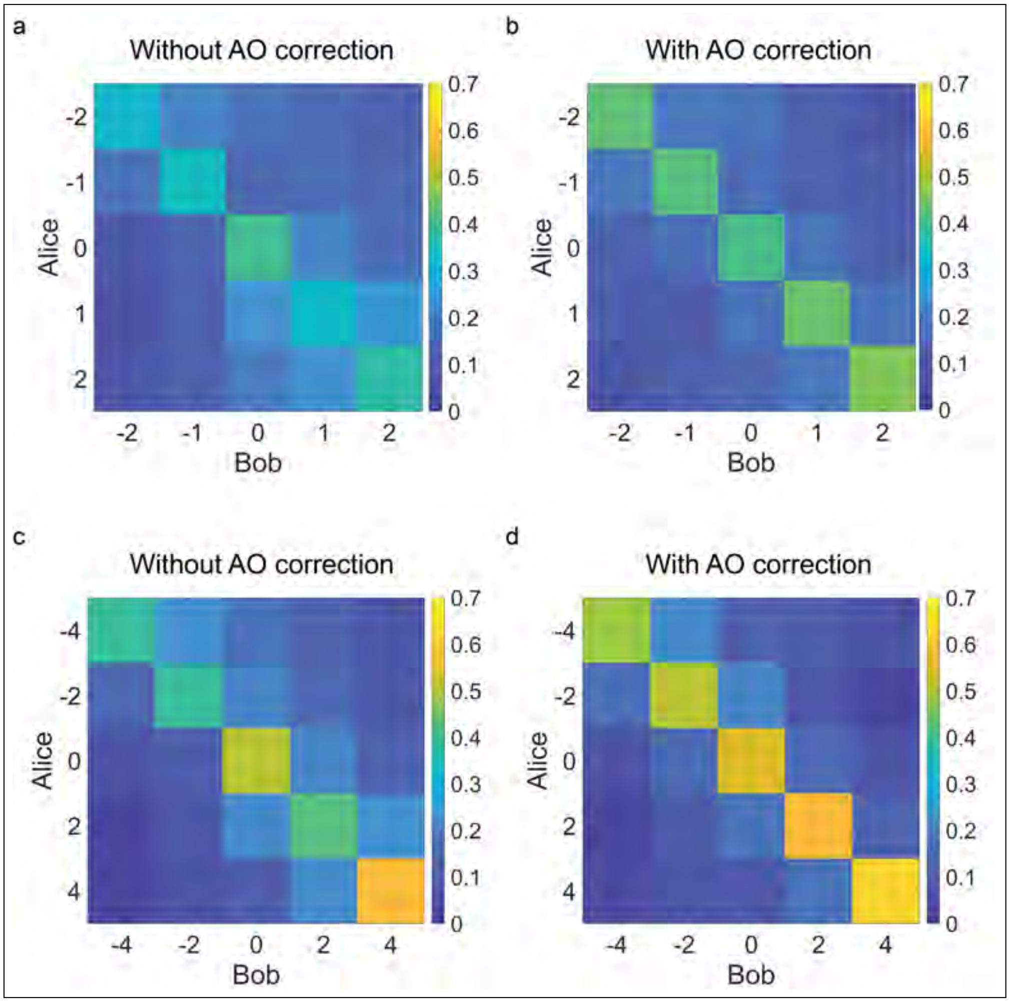

Figure 4.5: (a) and (b): measured crosstalk matrix of the OAM basis in the lab-scale link without and with AO correction respectively. The mode spacing is 1 in both cases. (c) and (d): measured crosstalk matrix of OAM basis in the lab-scale link without and with AO correction respectively. The mode spacing is 2 in both cases. The turbulence level in all figures is $D/r_0 = 1.90$.

Another approach is to introduce a new degree of freedom, which is robust to turbulence, as the ancillary basis. By doing so, the dimension d can be increased significantly, leading to a more robust encoding system. The most straightforward idea is using polarization as the ancillary basis, and the new emerging possible candidate basis include the radial degree of freedom. The possibility of encoding information on polarization and spatial degrees of freedom has been demonstrated in Ref.[8, 118], in which the authors cascade the spatial mode sorter (including radial and OAM) after HWPs and polarizing beam splitters (PBSs) to efficiently measure the received photons. Regarding our configuration, by introducing the polarization degree of freedom, the new joint encoding system has a threshold of 73.78% for $d = 10$, which is 5.23% lower than the error threshold for a $d = 5$ system (79.01%) [55]. The crosstalk matrix is shown in Figure 4.6 with turbulence level $D/r_0 = 1.90$. By calculating the average fidelity over all polarization states, we can find that the fidelity of the polarization degree of freedom is 98.23%. This demonstrates that the polarization degree of freedom is robust to turbulence, and will not introduce much additional error to the combined OAM-polarization MUBs.

Even though this improvement in the encoding dimensionality can be achieved by doubling the OAM encoding space, OAM states, especially the high order states, are not as robust as polarization states under turbulence [78, 99, 100]. Therefore, it is more convenient and robust to enlarge the encoding space by using polarization degree of freedom. Moreover, as shown in Figure 4.2, the fidelity under a turbulence level $D/r_0 = 0.30$ can be improved from 70.14% to 75.63% with AO correction. Considering the new error threshold of 73.78%, this improvement will allow two parties to estab-

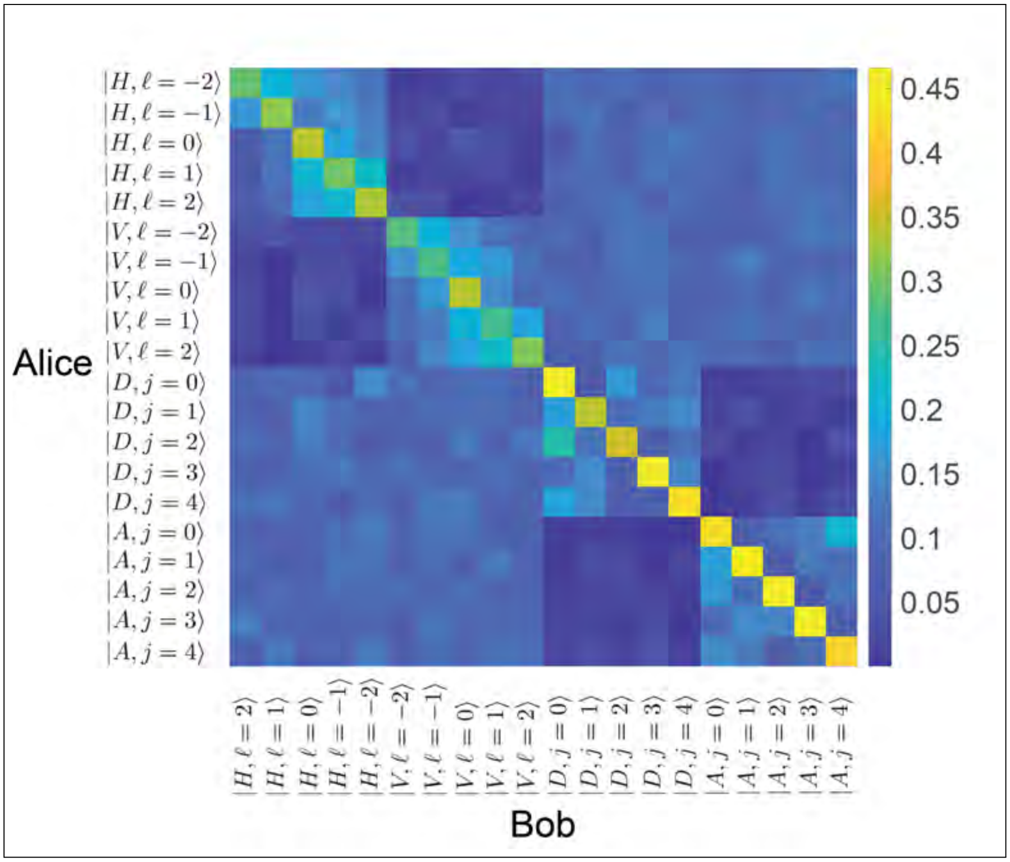

Figure 4.6: Crosstalk matrix of the joint encoding space including both OAM and polarization degree of freedoms.

lish a secure channel in our lab-scale link, which should have been impossible without enlarging the encoding space by introducing the polarization basis. However, we should note that the downside of this solution also exist. Since the error threshold is a logarithmic function of d, the improvement will become relatively small when the original d is large. Therefore, this approach is only applicable to systems whose QSER is close to the error threshold.

The last solution is to improve the performance of the entire AO correction system, which is conceptually most straightforward but also most complicated in engineering implementation. As we discuss before, a simple AO system consisting of one DM, one WFS, one FSM and one PD will not be sufficient for realistic OAM QKD systems, and the performance of each device should also be improved. Note that the specifications of each device depend on the free-space link, and the exact numbers can only be determined when the link parameters are fixed. The DM needs a large number of actuators to provide a high complexity of reconstructed wavefront, which should at least match the number of lenslets on the WFS and be complex enough to correct the dominant Zernike terms. The WFS should have an adequate number of lenslets and a high SNR for an accurate measurement. The AO system should operate at a high enough speed, which should be ten times faster than the Greenwood frequency (around 60 Hz), to comprehensively sample the time-varying wavefront and control the compensation loop [114]. The bandwidth of the FSM and PD is usually large enough and the more challenging requirement is the resolution and sensitivity. The FSM should be able to provide a sufficiently small step size but a considerable angular range so that it can accurately direct the beams toward the center of receiver's aperture even when the displacement is large.

In a real free-space link, an advanced AO system with multiple devices is necessary to compensate the wavefront error introduced by atmospheric turbulence. The first section of the system should consist of two FSMs, located at the Alice's side, to point the beams at the center of collection aperture.

At the Bob's side, the second section of correction system needs two FSMs and two PDs to accurately stabilize the received beams. These two sections jointly provide a precise beam tracking and control, which is essential to the advanced wavefront corrections afterwards [67, 68, 106]. In order to mitigate the error in intensity and phase profiles induced by moderate or stronger turbulence, an advanced wavefront correction system consisting of multiple conjugate DMs and WFSs with high resolution and large bandwidths is required. Based on our experimental data and simulation results [67, 68], we believe that an advanced AO correction system as described above is necessary. In theory, it should be able to correct the errors even under strong turbulence as well. However, the performance of such a system on OAM QKD still needs to be experimentally investigated.

Considering the complexity and cost of an advanced AO system as the one described above, it might be difficult to comprehensively build such a system. Therefore, we would suggest the following priority order under a limited budget. Based on our experimental observation, precise beam tracking is usually the first priority of the entire AO system. This conclusion comes from the fact that the OAM states are very sensitive to lateral displacement at the receiver's aperture, and such a tracking system is essential to the rest of the AO system. In addition, we believe the noise level and bandwidth are more important than the number of actuators on DM and the number of lenslets on WFS. This conclusion comes from the laboratory observation that in weak turbulence cases a pair of low-noise and high-bandwidth DM and

WFS should provide better measurement and correction accuracy than our results. The bandwidth for a comprehensive correction should be ten times larger than the Greenwood frequency of the turbulence [114]. However, for strong atmospheric turbulence, both of the pairs will not work and one has to use high-resolution and bandwidth DM and WFS.

Chapter 5

Conclusion and future work of free-space OAM QKD

In this first half of the thesis, I have tried to enhance the performance of high-dimensional OAM QKD in a free-space communication channel. The first study tries to answer the question: what is the optimal information carrier for OAM states for a distorted, noisy free-space channel. We use transmission efficiency and the fidelity of the received states to quantify the quality of each set of OAM modes. Four different states are numerically studied under various turbulence levels. Based on previous researches, the fidelity of the received states can be improved by using turbulence correction techniques. Therefore, we choose MEL states, which have the best transmission efficiency and the second-to-the best fidelity, as the optimal carrier in our research.

In chapter 3, we have analyzed the performance of a high-dimensional QKD system based on OAM encoding in the presence of SDD. In practical free-space quantum links with finite aperture sizes and long transmission distance, SDD can introduce a high error rate and security loopholes, which can significantly reduce the information capacity of the quantum link and the robustness against quantum attacks. To overcome this threat, we propose the WPC based on the use of MEL states, which have a uniform loss for all encoding states. We implemented this approach experimentally and showed that it can appreciably reduce the QSER and improve the secure key rate per transmitted photon. Since the two bases in the WPC protocol are orthogonal and mutually unbiased, the security of this new approach is the same as the conventional BB84 protocol. Therefore, by intentionally increasing the loss for certain states to get a uniform efficiency, we can significantly reduce the adverse effects induced by SDD, and improve the secure key rate in QKD systems.

In chapter 4, we study the performance and the possibility of OAM QKD in a turbulent channel under real-time AO correction. The effect of turbulence and the performance of the AO system are quantitatively studied in a lab-scale link under a controllable level of turbulence. We find that, under weak turbulence, real-time AO correction can mitigate the error induced by turbulence and recover the security of the channel. For moderate and strong turbulence, a simple AO system will not be adequate to mitigate the error and an advanced AO system as we described above is required. The performance of an AO system and OAM QKD in a 340 m long free-space link with finite collection aperture is also studied. Other than the effects we observed in the laboratory measurements, additional errors are induced by the lack of precise beam tracking system and mode-dependent diffraction. These errors can be mitigated by implementing a precise beam tracking and control. Finally, we discuss three different solutions to improve the performance of OAM QKD over a free-space communication link. We anticipate that, by following our suggestions, one should be able to comprehensively correct the error induced by atmospheric turbulence, either weak or strong turbulence, in an OAM QKD system.

We should also note that the main challenge in OAM QKD, no matter in free-space or fiber channels, is the strong modal-crosstalk induced by the random media. Therefore, the future demonstration should still focus on the efficient correction of distorted OAM states. I have also participated in other projects aiming to solve this issue. For example, the digital phase conjugation method done by our group has shown a new possibility of correcting OAM states in both fiber and free-space links [1, 2]. Therefore, we believe that the spatial modes are still promising candidates for future information-related applications.

Chapter 6

Introduction to computational spatio-temporal characterization of THz pulses

6.1 Terahertz frequency band and challenges in terahertz sensing

Based on the definition from the International Telecommunication Union, terahertz (THz) radiation denotes the electromagnetic waves within the frequency band from 0.3×10^{12} Hz (0.3 THz) to 3×10^{12} Hz (3 THz). A more flexible definition of THz frequency band ranges from 0.1 THz to 10 THz. Both definitions indicate the fact that the THz band lies between the microwave band and infrared band. Due to the lack of efficient generation and detection of THz radiation, the THz frequency band is considered as the THz gap for decades. Not until 1980s, few advanced were made, leading to a fast development of the field.

Since the THz radiation falls between the microwave radiation and infrared radiation, it shares some common properties of both frequency bands, which further leads to some unique applications of THz radiation. Similar to microwaves, THz radiation can penetrate a large collection of non-conducting material including wood, cloth, and plastic, which enables numerous applications in nondestructive inspection and security check. Due to the shorter wavelength, THz radiation can provide a better resolution comparing to microwaves. Like infrared and X-ray, THz radiation can also penetrate skin. Even though THz photons can introduce bleaching to some proteins, most biological tissues are not bleached or ionized by THz radiation due to the longer wavelength compared X-ray and infrared radiations, which is ideal for biomedical applications. Since some materials have their unique fingerprints in the THz frequency band, THz spectroscopy based on broadband pulsed THz radiations becomes a powerful tool to reveal the insights of composite objects, and hence the THz hyperspectral imaging, which is a spectroscopic imaging technique that the image can contain the information from a wide frequency bands, becomes a prominent application of THz technique. Therefore, in the second half of this dissertation, I will focus on the techniques of broadband THz pulses, which can inherit both general advantages of THz radiation as well as the rich spectral information carried by pulses.

However, all the applications discussed above are limited by the inefficient detection of THz radiations. Even though various studies are performed in the past three decades, efficient measurement of THz photons is still challenging in the community. Due to the long wavelength nature of THz photons, traditional semiconductor photodiodes are not applicable for THz detection.

Hence, the silicon-based charge-coupled device (CCD) camera is not able to capture THz images. As a consequence, the most widely used THz cameras are based on thermal detectors such as bolometers. Even though those incoherent thermal detectors can cover a broad frequency band and more sophisticated detectors based on metamaterial are developed in the past decade [119, 120], the sensitivity and dynamic range are usually unsatisfactory for weak pulse measurements unless they are cooled.

The most commonly used coherent THz measurement technique is based on electro-optic (EO) sampling, which can provide a sensitivity less than aJ-level and an accurate phase measurement with a precision less than 10^{-2} rad [121, 122, 123]. The underlying mechanism of EO sampling is the Pockels effect in EO crystals, which has an apparent similarity between the second-order nonlinear effect [123]:

$$\begin{aligned} P_i^{(2)}(\omega) &= 2\sum_{j,k} \epsilon_0 \chi_{ijk}^{(2)}(\omega,\omega,0)E_j(\omega)E_k(0) \\ &= \sum_{j} \epsilon_0 \chi_{i,j}^{(2)}(\omega)E_j(\omega), \end{aligned} \tag{6.1}$$

where $P_i^{(2)}(\omega)$ is the nonlinear polarization at frequency ω, and $\chi_{i,j}^{(2)}(\omega) = 2\sum_{j,k}\chi_{ijk}^{(2)}(\omega,\omega,0)E_k(0)$ is the field induced susceptibility tensor. Since in a lossless medium $\chi_{ijk}^{(2)}(\omega,\omega,0) = \chi_{ijk}^{(2)}(0,\omega,-\omega)$ [124], the nonlinear coefficient of the Pockels effect is the same as the optical rectification. Thus, a nonlinear crystal which is ideal for THz generation via optical rectification will be an appropriate candidate for THz detection. From Eq. (6.1), it is obvious that, in a nonlinear media with the second order susceptibility, a static electric field $E_k(0)$ can introduce a birefringence to the field $E_j(\omega)$ and the amount of the polarization drift is proportional to the field amplitude. Inversely, one can also determine the field amplitude by measuring the field-induced birefringence, which is the cornerstone of EO sampling. It is worth noting that the assumption of the static electric field $E_k(0)$ is usually valid in THz detection because the electric field of THz pulses can be considered as a static field due to the much slower oscillation compared to the optical or near-infrared (NIR) pulses.

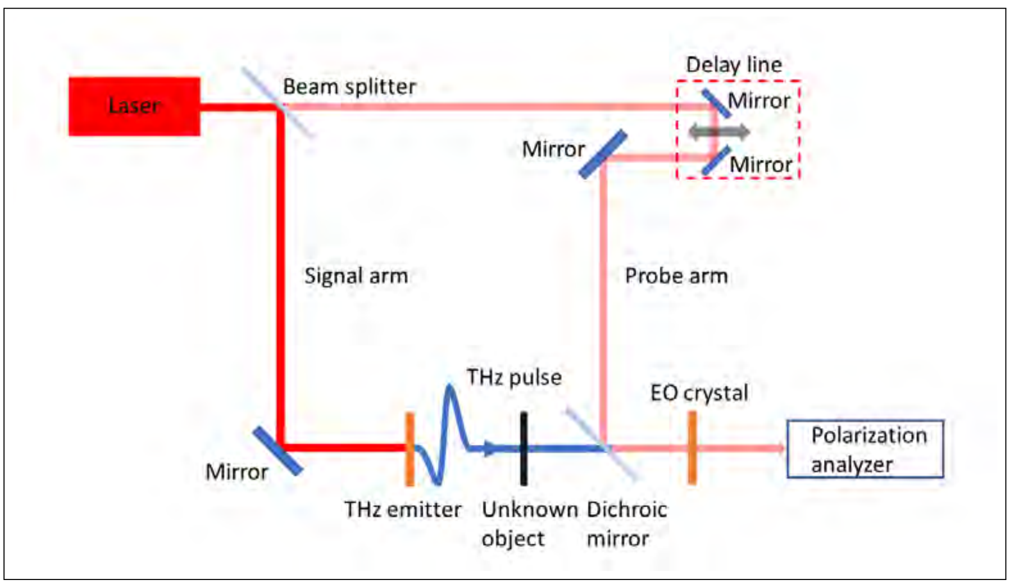

Figure 6.1: The typical configuration of a THz time-domain spectroscopy system. The dark red line denotes the signal pulse while the dim red line stands for the probe pulse.

Based on EO sampling, researchers develop the THz time-domain spectroscopy (THz TDS) system, which becomes the dominant technique for coherent detection of THz pulses. The typical setup of THz TDS is shown in Figure 6.1. The laser pulse is splitted into two parts by a beam splitter. The first pulse, which is usually the stronger one and called the signal beam, is used to pump a THz emitter for THz pulse generation. Note that this THz emitter can be but not limited to nonlinear crystals, antennas, plasma or spintronic devices. After the generation crystal, the THz pulse is usually focused onto the unknown object to provide a better signal-to-noise ratio (SNR). A THz lens or parabolic mirror, which is not shown in the figure, is used to refocus the THz pulse, which is carrying the information of the object, onto the detection EO crystal. The second pulse, which is usually named as the probe beam, is used as the reference to measure THz pulses. To make sure both pulses interact in the EO crystal, they have to be spatio-temporally coincide with each other, and the relative time delay between two pulses can be adjusted by a delay stage. Thus, the system becomes a two-arm nonlinear interferometer. We should note that even though the delay line is shown in the probe arm, it can also be placed in the signal arm. After the EO crystal, the polarization drift of the probe pulse will be detected by the polarization analyzer. To enhance the sensitivity and robustness against noises, the signal is usually detected by a pair of balanced photodiodes and analyzed by the lock-in amplifier. If we use $P_{\mathrm{s}}(t)$ to represent the differentiated signal detected by the balanced photodiodes, we will find the following relation [123]:

$$P_{\mathrm{s}}(t) = \frac{1}{c} I_0(\omega_1)\omega_1 L n_0^3(\omega_1) r_{14} E_{\mathrm{THz}}(\omega_{\mathrm{THz}}, t), \tag{6.2}$$

where c is the speed of light in vacuum, and $E_{\mathrm{THz}}(\omega_{\mathrm{THz}}, t)$ is the THz electric field. $I_0(\omega_1)$ is the intensity of the probe on the detection crystal. L is the thickness of the detection crystal, and ω_1 is the frequency of probe. $n_0(\omega_1)$ is the refractive index of the detection crystal at optical frequency ω_1. r_{14} is the EO efficient of the detection crystal, and here we have assumed that the detection crystal is ZnTe.

Even though EO sampling can provide coherent measurement of THz pulses with a high sensitivity and precision, it is not very convenient in real applications such as THz imaging. To measure the image of an unknown object, raster scanning is usually required to provide the sampling over the entire transverse plane. If a hyperspectral image is required, raster scanning all three degrees of freedom, two transverse and one longitudinal degrees of freedom, is necessary to acquire a comprehensive hyperspectral image. This time-consuming measurement procedure can take hours to get one image, which is not ideal for real applications.

To reduce the data acquisition time in the imaging process, EO imaging was demonstrated as a real-time THz imaging technique in late 1990s [125, 126]. Rather than focusing the THz pulse onto one single spot, researchers use parabolic mirrors or THz lenses to collimate the THz pulse, and adjust the size of the THz pulse to be large enough to cover the unknown object. Then this collimated THz pulse is used to illuminate the unknown object. After the polarization analyzer, a camera is used to replace the photodiode to provide the real-time measurement of the entire transverse structure of the THz pulse. The balanced detection strategy in the single-pixel THz TDS system can be implemented as well to further enhance the sensitivity and robustness against noises. However, EO imaging inevitably has a worse SNR comparing to the conventional raster scanning THz imaging, which mainly comes from two facts: 1. The sensitivity of camera sensor is usually worse than photodiodes; 2. The intensity of the THz pulse in EO imaging is much weaker. Therefore, based on Eq. (6.2), both reasons result in the fact that, to get a high quality image from EO imaging, a THz pulse with a large electric field, hence the high pulse energy (pJ to nJ level), a thick EO crystal and a high-performance camera are necessary. In order to generate a pJ to nJ level THz pulse, the pump pulse energy is usually above μJ level. This indicates that the compact oscillator lasers without amplification cannot be used due to the weak pulse energy (usually sub-μJ level). Therefore, to meet these requirements, a complicated and expensive system would be required, which is not convenient for most applications.

Some new techniques have emerged in the past two decades to achieve fast THz imaging with a high sensitivity. For example, the interferometric or tomographic method can significantly reduce the number of measurements to get a good image. However, the acquisition speed is still limited by the scanning rate unless a sensor array is used [127, 128]. Another possible approach is THz reciprocal imaging, which can achieve high-speed imaging with a single-pixel detector but requires multiple sources modulated at different frequencies [129]. Therefore, this method is not ideal for most applications.

To reduce the measurement time in the time-domain measurement, numerous attempts are demonstrated as well. The most widely used approach is still mechanically scanning a delay line. By designing various mechanical stages, the state-of-art scanning rate can be hundreds of Hz providing real-time TDS measurement. However, the physical limitation of mechanical scanning, such as accuracy and stability, cannot be omitted. Single-shot measurement is another approach to achieve real-time THz measurement using cameras or spectrometers. However, due to the limited performance of cameras and spectrometers, the measurable THz pulses are usually at pJ to nJ level. Thus, this technique is not applicable for weak pulse measurement at the moment [130]. Asynchronous optical sampling has been demonstrated to be effective for real-time THz pulse measurement as well [131, 132]. Unfortunately, the system has to include two mode-locked ultrafast lasers with a fixed repetition frequency offset, which is not ideal for real applications as well.

Based on what we discuss above, we can conclude that for practical and time-critical applications, a THz sensing system should not only preserve the advantage in detection sensitivity of the single-pixel detection scheme and the coherent detection nature of EO sampling, but also have a fast data-acquisition time to achieve real-time spatio-temporal characterization of THz pulses. Luckily, regarding the spatial measurement, these requirements naturally coincides with the advantage of single-pixel imaging technique so that developing practical THz single-pixel imaging system becomes a promising direction. Meanwhile, due to the spatio-temporal duality of light pulses, applying the concept of single-pixel imaging to the time domain could be a possible solution to achieve real-time, sensitive THz sensing as well.

6.2 Principle of single-pixel imaging and compressive sensing

Before we introduce the development of THz single-pixel imaging in the past decade, it is convenient to briefly introduce the history and principle of single-pixel imaging (SPI), as well as the major algorithm used in this technique: compressive sensing.

SPI originates from ghost imaging, which was firstly developed by Yanhua Shih's group in 1995 [133, 134]. In the early development of ghost imaging, the phenomenon is believed to originate from the quantum nature of light. Until 2002, Robert Boyd's group demonstrates that the quantum source is not necessary and the result can be obtained by using a classical source along with correlation measurement [135]. From that point, people start realizing that the core of ghost imaging is not entanglement but the correlation between the measurement results and corresponding structured illumination used to sample the objects. In 2008, the computational ghost imaging is proposed theoretically by Jeffrey Shapiro, who points out that the camera, which is used to record the structure of the illumination in ghost imaging, is not necessary if one deterministically prepare the structured illumination using a SLM [136]. The first experimental realization of this proposal is demonstrated later by Yaron Silberberg's team, which becomes the prototype of SPI [137]. Since then, this technique becomes a computational imaging technique and is demonstrated in multiple fields including different electromagnetic waves at various wavelengths, 3-D imaging, acoustic imaging, etc [138, 139, 140, 141].

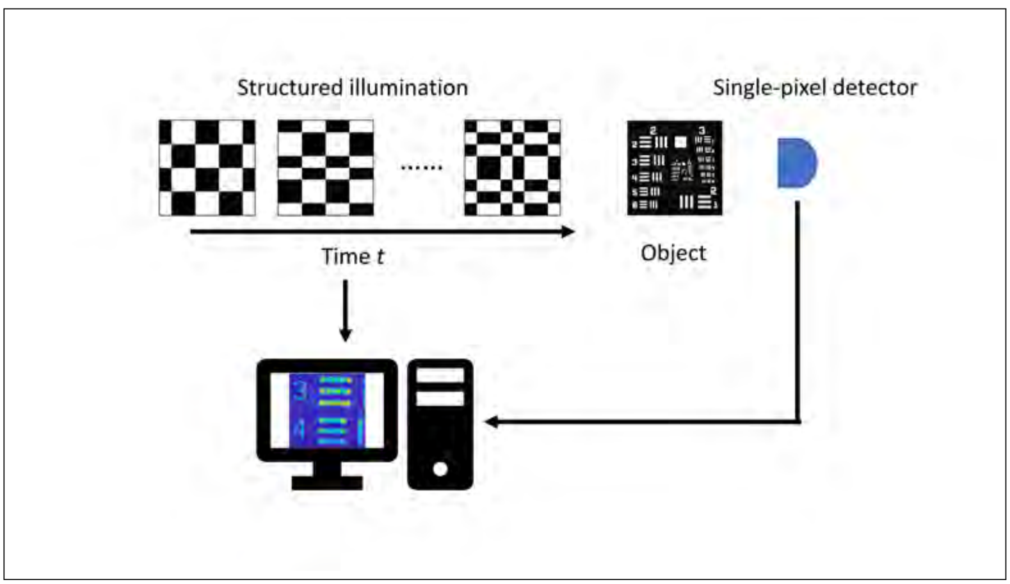

Figure 6.2: The flowchart of the single-pixel imaging procedure.

Conventional imaging systems are based on plane-wave illumination and cameras. The sampling of the continuous electromagnetic wave is executed by the pixelated sensor array on the camera simultaneously, while the sampling size is the pixel size of the sensor array. As a comparison, the procedure of SPI is very different as the flowchart we show in Figure 6.2. The first step is using various structured illuminations, sequentially in time, to sample the object, and a single-pixel detector, without any spatial resolution, to collect the entire electromagnetic field after the object. Then by correlating the structured illumination and the corresponding signal registered on the detector, the image can be computationally recovered using compressive sensing.

The entire procedure can be understood mathematically using vector decomposition as well. If we assume the desired image has N pixels, we will use a N-dimensional unknown vector ψ in a N dimensional Hilbert space to represent it. Therefore, this unknown vector can be decomposed into a set of complete orthogonal basis S in that N dimensional Hilbert space with a coefficient vector ϕ. We can rewrite this decomposition into the matrix form: $\psi = S\phi$, where ψ and ϕ are two N dimensional column vectors representing the unknown vector and the coefficients of each basis vector respectively. S is a $N \times N$ matrix and each row represents a basis vector in the Hilbert space. Therefore, one can reconstruct the unknown vector ψ by measuring the coefficients sets ϕ in the complete orthogonal basis S, and these coefficients can be found as $\phi = S^{-1}\psi$. In order to measure the coefficient vector ϕ, the unknown vector ψ needs to interact with the sampling matrix S^{-1}, which is the most important step in the experimental realization.

In the conventional imaging system using either raster scanning or cameras, the sampling basis S is the natural basis which is a N-dimensional identity matrix and each row vector representing the sampling of one specific position. Therefore, there is no correlation in the sampling process between two arbitrary positions. The only difference between raster scanning and the camera is that the sampling process happens simultaneously for all positions in camera while sequentially in raster scanning. However, we can use other basis, whose row vectors contain multiple nonzero elements, to sample multiple positions simultaneously as well. In this case, each sampling includes the correlation between multiple positions and thus provides richer information in each measurement. To get a better understanding, we will use an example to illustrate the difference. We assume that a $A \times B$ image with $N = AB$ can be unwrapped into a N-dimensional vector ψ whose the first B elements are the B elements in the first row of the image. If we are using the natural basis to recover the image, the kth row vector of S will represent the sampling of the kth element in ψ, which corresponds to the position (a, b) in the image where $k = (a-1) \times B + b$. As a comparison, if we use a more complicated matrix S and assume that the kth row vector of S simply have 2 nonzero elements, the $(k+1)th$ and $(k-1)th$ element, this row vector will jointly sample both $(a, b+1)$ and $(a, b-1)$ positions in the image. This further leads to one advantage of SPI: better SNR than conventional imaging. If we assume that the noise-equivalent power of all detectors, including both photodiodes and each single detector on the detector array, is the same, the image acquires by both raster scanning and camera will have the same SNR. As a comparison, since multiple pixels are illuminated during each sampling in SPI, the SNR will be much higher than raster scanning and camera imaging, and the experimental demonstration will be present in the next chapter.

Another advantage of SPI is the more efficient data acquisition step when the compressive sensing (CS) algorithm is used, thereby a reduced requirement of data storage and transfer, which is especially important for applications involving a large amount of data such as hyperspectral imaging. The basic idea of compressive sensing comes from the fact that, for a N dimensional vector ψ, it is possible to find a basis R that most coefficients in the coefficient vector ϕ are zero or very small. What the CS does is to exploit the sparsity of the signal vector, through optimization, to recover most information by only adopting those nonzero coefficients. Therefore, one can beat the Nyquist sampling limit by sub-sampling the signal without losing too much information. To successfully implement CS, two conditions have to be fulfilled: the sparsity of the signals of interest, and the incoherence of sensing basis S and recovery basis R [142].

Sparsity pertains to the signals of interest that is independent of the choice of sensing basis. Luckily, most signals in nature are sparse if they are represented in convenient bases [142]. Therefore, in most cases, we don't have to worry about the first condition. The second condition requires that the sampling and recovery bases are mutually incoherent. The coherence between two bases is defined as the largest correlation between any two elements in

S and R:

$$\mu(S,R) = \sqrt{N} \times \max|\langle S_k, R_j \rangle|, \tag{6.3}$$

where N is the dimension of the basis and $1 \leq k, j \leq N$. Therefore, two bases are maximally incoherent when $\mu(S,R) = 1$. One example of maximally incoherent bases is the Fourier conjugate bases (for example position-momentum, time-frequency). Another general choice of the sampling basis is random basis since it has little coherence with any fixed basis ($\mu(R,S) \sim \sqrt{2\log N}$). This explains why random basis, no matter in spatial ghost imaging or temporal ghost imaging, can always work as the sampling basis in CS. However, we will show that random basis is usually not the ideal choice of the sampling basis.

We first assume that the signal ψ can be measured using basis S with the measurement result coefficient vector ϕ: $\phi = S\psi$. Now we assume that there is a basis R which is incoherent with S. If we assume that most coefficients under this representation R are close or equal to zero, we can recover the signal ψ by ℓ_1-norm minimization. The solution coefficient vector ϕ' can be found by solving the convex optimization problem [142, 143]:

$$\min \|R\psi'\|_{\ell_1}, \text{subject to } S\psi' = \phi', \tag{6.4}$$

where $\|\cdot\|_{\ell_1}$ is the ℓ_1-norm. If the coherent coefficient between two bases Q and T is very little, i.e. two bases are incoherent, the THz field vector ψ can be reconstructed with $M \geq O[Klog(N)]$ measurements, where K is the number of nonzero components of vector $R\psi$ [144]. Therefore, we can surpass the Nyquist rate but still recover the field with a high fidelity, where the fidelity is defined as the correlation coefficient between the vector recovered by CS and the vector recorded by camera.

Before we proceed, it is necessary to discuss the basis choice in CS. As what we discuss above, Fourier conjugate basis and random basis are both common choice of sampling basis in CS. From a historical reason, random basis has been used in ghost imaging or SPI for about two decades since the early development of ghost imaging. However, we have to carefully reconsider the use of random basis and keep in mind that the goal of using CS is to achieve high fidelity signal recovery via sub-sampling the signal. Even though random basis is a choice of sampling basis for most scenarios, it is not the ideal choice in most cases due to the randomness in the sampling process. This randomness will result in a noisy recovered signal if one strictly sub-samples the signal and does not average out these noise. Therefore, when the random basis is used, one usually has to over-sample the signal to eliminate noise, which loses the point of implementing CS instead. The experimental demonstration has been reported separately by different groups and will be shown in the next chapter. Thus, a deterministic basis is a better choice in real applications unless the preparation of such basis is not available.

One widely used and deterministic basis is the family of Hadamard matrices (HM), which includes many differently ordered HM such as the natural-ordered HM and Walsh-ordered HM. This matrix is a square matrix whose elements are either +1 or -1, and satisfies the relation: $HH^T = H^T H = NI$, where H^T is the transpose of H and I is the N-dimensional identity matrix [145]. Since the rows of the matrix are mutually orthogonal, the N-dimensional HM matrix naturally spans a N-dimensional Hilbert space, and the row vectors are basis vectors [145]. Mathematically speaking, multiplying the HM to a vector is called the Hadamard transform of the vector, which is a generalized Fourier transform. Therefore, HM is the Fourier conjugate basis which is maximally incoherent with the natural basis. That is to say, when we use HM as the sampling basis in SPI, the measurement is done at different spatial frequencies. If we use HM to sample a temporal signal, the measurement is done at different frequencies. Considering the fact that low frequency components carry the major information of most signals in nature, it is convenient to use Walsh-ordered HM as the sampling basis, whose row vectors represent different frequencies in an increasing order. Meanwhile, using HM in imaging can minimize the mean square error of the image as well [145]. Therefore, using Walsh-ordered HM as the sampling basis is advantageous and convenient, which will be our choice of sampling basis.

In the next two chapters, we will focus on applying the concept of SPI in THz sensing. We will first introduce the development of THz SPI and reveal the fact that all current THz SPI techniques either require the fabrication of THz devices, a complicated system with multiple lasers, or suffer from a limited sampling rate as well as the tradeoff between resolution and SNR. To provide a simple and robust configuration of THz SPI, we propose and demonstrate the concept of probe-beam encoding. Images are recovered using different measurement approaches, and a comprehensive discussion is provided. Later, we implement the concept of SPI into the time domain, and propose the concept of temporal SPI for the first time. By using the temporal SPI based on probe-beam encoding, we successfully recover ultrafast signals at different frequency bands with a high measurement efficiency and fidelity. The robustness against temporal distortion is also demonstrated. We show that a THz spectroscopy system can be realized only with our sensitive technique even with the help of machine learning.

Chapter 7

Computational sampling of terahertz field based on probe-beam encoding

7.1 Development of terahertz SPI

From our discussion in the last chapter, we can find that SPI is naturally compatible with THz TDS systemsbecause it solely requires a single-pixel detector for the measurement. Moreover, the high SNR and better measurement efficient are both desired feature for THz sensing. However, the difficulty of directly applying this technique to THz frequency band is the lack of THz SLM.

The most important step in the sampling process of SPI is the preparation, especially the deterministic preparation, of structured illumination. This is straightforward for optical and NIR frequency bands due to the high-performance commercially available SLM, while for THz band, such devices are not available. Therefore, in the past decade, people devote their efforts to find effect ways to modulate the structure of THz pulse. The modulation of the THz illumination in first experimental realization, which is demonstrated by Daniel Mittleman's group, of THz SPI is achieved by using spatial masks [146]. The random sampling basis is printed onto numerous metallic masks, which are illuminated by a plane-wave THz pulse. A Chinese characeter "light" is successfully imaged at different compression ratios (CR). Compression ratio is defined as the ratio between the number of measurements taken in the experiment over the number of measurements that would correspond to the Nyquist sampling rate. As the first demonstration, this work shows the potential ability of imaging THz waves using a conventional TDS system. However, as one can imagine, static masks are not ideal tools for real applications due to limited flexibility. Moreover, the limited mechanical switching speed further increase the total measurement time, which is not practical for time-sensitive imaging.

Thus, people start trying to develop THz SLMs to efficiently modulate THz pulses. The first attempt of THz SLM is also carried out by Daniel Mittleman's group in 2009 [147]. A 4×4 active THz metamaterial is prepared as the THz SLM. Due to the limited performance including low modulation depth, large crosstalk between adjacent pixels and a small number of pixels, THz SPI was not demonstrated at that moment. In 2014, Willie Padilla's group demonstrate the first THz SPI using a metamaterial-based THz SLM [148]. A cross sign is imaged with 8×8 pixels using a 64-dimensional HM and random matrix. With a 70% CR, they can achieve real-time imaging at 1 frame/s and the switching rate is about 45 Hz. This state-of-art demonstration shows the possibility of building customized THz SLMs and using it for SPI. However, the performance of these THz SLMs are still worse than their optical counterparts. They are not only hard and expensive to fabricate, but also have a slower switching rate and a much fewer number of pixels even compared to LCOS-SLMs.

People then try to use optical SLMs to modulate structures of THz pulses. The first demonstration is also done by Willie Padilla's group in 2013, and then becomes a popular approach in the past few years [149]. Through modulating the density distribution of the photoexcited free carriers in semiconductors and hence the THz transmittance distribution, they successfully modulate the THz structure using a commercially available optical SLM. The high flexibility and speed of optical SLMs enable the real-time recovery of a 7×9 image. This method is then adopted to achieve near-field THz imaging in 2016 [150]. However, the main limitation of this approach is the complicated system and the slow response of free carriers in semiconductors. To excite the free carrier, an additional laser is required. Splitting the laser pulse used for THz TDS into the third copy is effective way to avoid the requirement of a new laser. However, this will further results in a more complicated system which is basically a three-arm interferometer. Moreover, the switching speed of this approach is fundamentally limited by the free-carrier lifetime in semiconductors, leading to a modulation rate around kHz. Therefore, even though this approach has been developed over 8 years, real-time imaging has only been demonstrated recently for 32×32 images [151].

A novel approach of using optical SLMs to achieve THz SPI is proposed in 2018 [152]. Based on the concept of nonlinear ghost imaging, structured pump is firstly prepared with optical SLMs and then used to generate structured THz pulses. The system is almost the same as the conventional THz TDS system, and therefore a simple and reliable configuration is obtained. However, due to the limited damage threshold of optical SLMs, the energy of the pump pulse cannot be strong, and hence the generated THz pulse will have a lower upper bound of the pulse energy. One possible solution to this issue is using a thicker crystal for THz generation. Unfortunately, due to the strong diffraction of THz pulses, the structured pattern on THz pulses will quickly get blurred during the propagation inside a thick crystal, leading to an inaccurate sampling of the object. Therefore, this approach fundamentally suffers from the tradeoff between SNR and resolution.

Thus, it is necessary to develop a simpler THz spatial sampling approach which not only preserves the advantage in simplicity and flexibility of the conventional THz TDS, but also takes the advantage of commercially available optical SLMs.

7.2 Concept of probe-beam encoding and the theoretical model

As what we introduce in the last chapter, the EO effect is one of the most widely used THz techniques for coherent detection. When a THz field interacts with an EO crystal (usually ZnTe or GaP), it introduces a birefringence, which modifies the polarization of a co-propagating 800 nm NIR probe beam. This rotation in polarization is measured by a pair of balanced detectors to determine the time-dependent THz electric field. If we rewrite Eq. (6.2) in the form containing the transverse distribution of fields, we will have the following equation describing the relation between the probe-beam intensity distribution $I_0(x, y, \omega_1)$ and THz field distribution $E_{\mathrm{THz}}(x, y, \omega_{\mathrm{THz}}, t)$:

$$P_{\mathrm{s}}(t) = \int\int \frac{1}{c} I_0(x, y, \omega_1)\omega_1 L n_0^3(\omega_1) r_{14}(x, y) E_{\mathrm{THz}}(x, y, \omega_{\mathrm{THz}}, t) dx dy, \quad (7.1)$$

where $E_{\mathrm{THz}}(x, y, \omega_{\mathrm{THz}}, t)$ also carries the information of the unknown object. It is obvious that only the THz field which both spatially and temporally coincides with the probe on the detection crystal can be detected. Therefore, solely manipulating the probe arm in the spatial domain is equivalent to spatially modulating the THz field in the same manner but leaving the probe field unchanged. Moreover, from the measurement point of view, as long as the polarization of the optical probe is kept, spatially changing the probe field will not change the signal on the balanced detector. Therefore, from the SPI point of view, it does not matter whether we manipulate the THz field or the probe field. However, even both methods give the same result in principle, encoding patterns on the probe beam can significantly simplify the system without any additional requirement as what we discuss in the introduction. Moreover, since the energy of the probe pulse is intrinsically weak and irrelevant to the pump pulse energy, there is no limitation on the pump pulse so that a strong THz pulse is applicable. Therefore, it is advantageous to use probe-beam encoding to achieve THz SPI.

To encode HM basis onto the probe beam, we will use a commercially available NIR SLM. Since HM is a square matrix with $+1$ or -1 elements and SLM cannot encode negative values, we have to decompose the HM matrix into H_{+1} and H_{-1} which carries only $+1$ or 0 elements and -1 or 0 elements respectively: $H = H_{+1} + H_{-1} = H_{+1} - |H_{-1}|$. Considering the rules of linear algebra, we have the following relation to reconstruct the image:

$$\psi = (H_{+1} - |H_{-1}|)\phi, \tag{7.2}$$

where both H_{+1} and $|H_{-1}|$ only carry $+1$ or 0 elements so that they can be generated from SLM directly.

Now we consider an unknown object with intensity distribution $O(x, y)$ placed before the detection crystal. For a given i_{th} HM pattern $I_i(x, y, \omega_1)$ which is imaged from SLM plane onto the detection ZnTe crystal with thickness $d = z_1 - z_0$, we can find the measured THz total field $P_{\mathrm{s},i}$ from Eq. (7.1) as:

$$\begin{aligned} P_{\mathrm{s},i}(t) = \int\int\int_{z_0}^{z_1} \frac{1}{c} I_i(x, y, z, \omega_1)\omega_1 L n_0(\omega_1)^3 \times \\ r_{14}(x, y) E_{\mathrm{THz}}(x, y, z, \omega_{\mathrm{THz}}, t) dxdydz, \end{aligned} \tag{7.3}$$

where $E_{\mathrm{THz}}(x, y, z, \omega_{\mathrm{THz}}, t)$ can be found from scalar diffraction theory using angular spectrum:

$$\begin{aligned} E_{\mathrm{THz}}(x,y,z,\omega_{\mathrm{THz}},t) =& \mathcal{F}^{-1}\{\mathcal{F}[O(x,y,0)]\times \\ & \exp\Big[i2\pi\sqrt{(k_{\mathrm{THz}}/2\pi)^2 - f_x^2 - f_y^2 z}\Big]\}. \end{aligned} \tag{7.4}$$

$\mathcal{F}$ and $\mathcal{F}^{-1}$ represent Fourier Transform and inverse Fourier Transform respectively. f_x and f_y are spatial frequencies in x and y directions. Here, we have assumed that the THz wave has a uniformly distributed intensity. One can then find the corresponding HM pattern $I_i(x,y,z,\omega_1)$ using Eq. (7.4). With $I_i(x,y,z,\omega_1)$ and $E_{\mathrm{THz}}(x,y,z,\omega_{\mathrm{THz}},t)$, we can find the signal $P_{\mathrm{s},i}$ for the i_{th} pattern. By repeating this procedure for all patterns, we can get the signal set $P_{\mathrm{s},i}$ which form the coefficient vector ϕ. This coefficient vector will be used to reconstruct the image vector ψ through Eq. (7.2). To show the state of art, the analysis here does not include the broadband nature of THz pulse. However, the simulation we will show already take the spectra contribution into consideration.

7.3 Experimental realization of THz SPI via probe-beam encoding

The experimental setup is shown in Figure 7.1. A THz pulse, generated through optical rectification from a ZnTe crystal as shown in the schematic Figure 7.1(a) and (b), passes through a covered object and is detected through electro-optic sampling by another ZnTe crystal [153]. A sequence of spatial

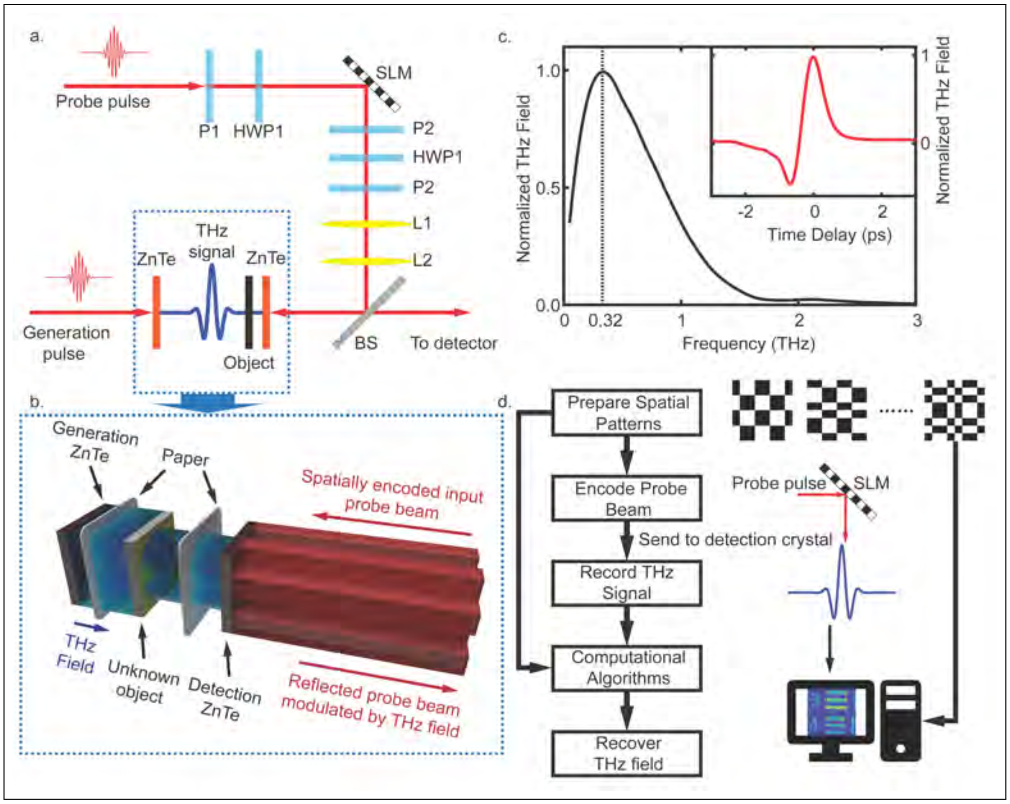

Figure 7.1: (a). Diagram showing the schematic system configuration while (b) shows the detailed feature of the sampling approach. The unknown object, an AF test chart, is wrapped in paper so that it is invisible to the NIR probe beam. P1, P2, and P3 are polarizers while HWP1 and HWP2 represent half-wave plates. L1 and L2 image the SLM plane onto the left surface of detection ZnTe crystal. BS is a 50/50 beam splitter. The modulated probe beam is then sent to a single-pixel detector for measurement. Detailed specifications can be found in the Methods. (c). The spectrum of the generated THz pulse, and the time-domain electric field distribution with a spatial mask encoded on the NIR probe beam. The spectral peak occurs at 0.32 THz, which corresponds to 940 μm central wavelength. The SNR of the THz signal is about 300. (d). The flowchart shows our procedure of single-pixel imaging via probe-beam encoding.

masks is loaded on the SLM to encode the NIR probe pulse. Then this spatially encoded 800 nm probe beam first illuminates the detection ZnTe crystal in the counter-propagation direction of the THz pulse as shown in Figure 7.1(b). On reflection from the both surfaces of the detection ZnTe crystal, two reflected NIR beams co-propagate with the THz pulse. However, only the polarization of the beam reflected from the left surface of the crystal is modulated by the spatiotemporally coincident THz field. To separate these two reflected beams, the detection ZnTe crystal is slightly tilted, and one lens is then used to focus them (not shown in the figure). With the help of an iris at the focus, the reflected beam carrying information is selected out and sent to the single-pixel detector, consisting of a quarter-wave plate, a Wollaston prism and a balanced photodiode detector, to retrieve the time-dependent THz signal. The original time domain THz pulse and corresponding spectrum are shown in Figure 7.1(b) and (c), respectively. The object, a positive US Air Force (AF) target made with chromium, is wrapped in a 70-μm thick piece of paper, and placed tightly before the detection crystal. Therefore, THz pulse only travels about 70 μm before interacting with the detection crystal, and the near-field information is maintained [154]. As shown in the flowchart in Figure 7.1(d), after recording the THz signal and the corresponding patterns, the THz transverse field distributions can be reconstructed with computational algorithms. Note that the translation stage keeps at the peak value position during the imaging process.

We first use the HM to probe the THz field, and successfully recover the

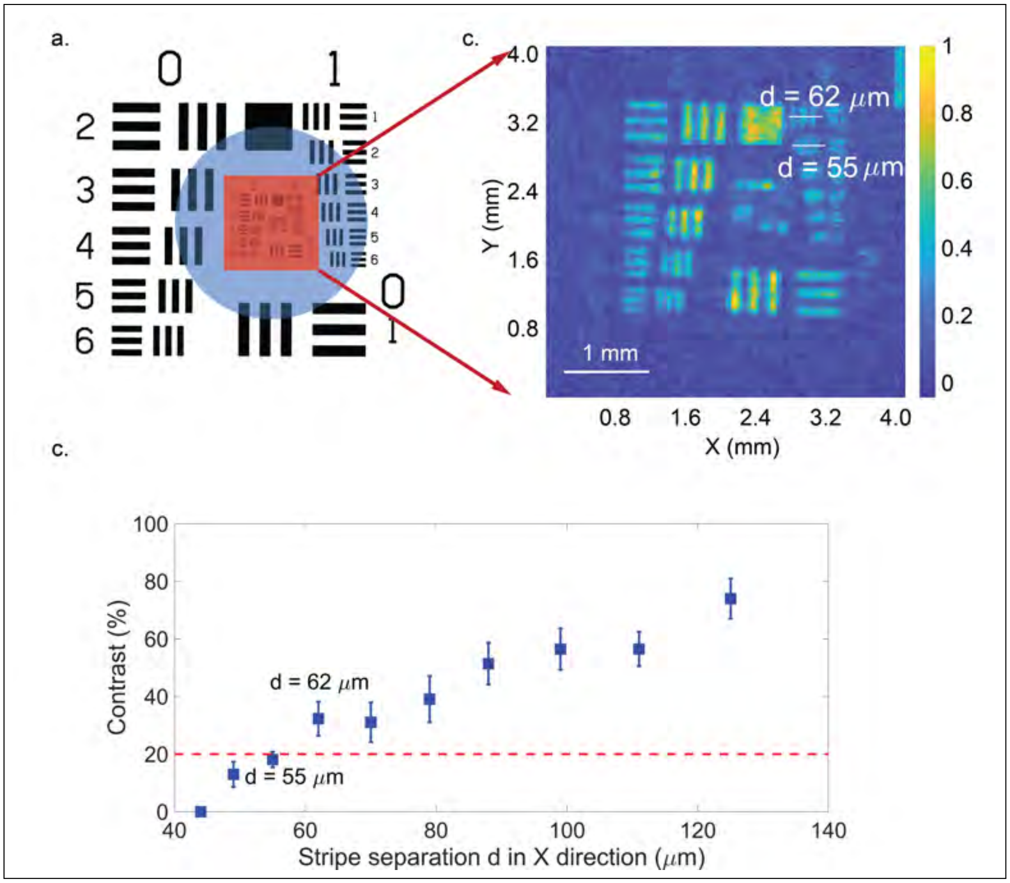

Figure 7.2: (a). The original AF target. The red square is the area that the probe beam illuminates. The blue circle shows the parts illuminated by the THz field. (b). The experimental result with 128×128 pixels showing the resolution limit. (c). The contrast as a function of strip separation d. The red dashed line is the threshold contrast assumed by Rayleigh criterion. Two points can be resolved if the contrast is equal or greater than 20%. Therefore, the element set with d = 55 μm is not resolved while the element set with d = 62 μm is resolved according to the Rayleigh criterion.

field distribution with 128×128 sample points. As what we discuss before, since the SLM can only encode non-negative values, we have to break the HM into H_{+1} and $|H_{-1}|$. The experimental realization of this procedure is done by encoding the probe beam with H_{+1} and $|H_{-1}|$ patterns sequentially on one SLM, and recording the corresponding signals. To reconstruct the image, one needs to subtract the $|H_{-1}|$ patterns weighted by the corresponding signal from H_{+1} patterns weighted by the corresponding signal. Although this differential method will double the measurement time, it can eliminate the source noise if one immediately shines the $|H_{-1}|$ mask right after the corresponding H_{+1} mask. That is to say, one does not need to introduce any additional power monitor to track the laser power fluctuation.

7.4 Resolution estimation

The experimental results are shown in Figure 7.2. In Figure 7.2(a), we selectively sample the central elements of the AF chart to estimate the spatial resolution limit, which is defined as the size of the smallest resolvable feature. The recovered image is shown in Figure 7.2(b), and has a square sampling pixel with 32 μm width(i.e. one pixel consists of 2×2 pixels on the SLM). In Figure 7.2(c), we show the contrast of each element in group 2, and element 3-1 (the first set of elements in group 3) and 3-2 as a function of strip separation d in the X direction. We find that the element with d = 55 μm (element 3-2) has an average contrast of 18.10%, while the element with d = 62 μm (element 3-1) has a 32.28% average contrast. Since from Rayleigh criterion, two points are barely resolved with a contrast equal to 20% (red dashed line in Figure 7.2(c)), the resolution of our system is found to be

62 μm. Considering the central THz wavelength (λ_c) is 940 μm, we have achieved a resolution of about $\lambda_c/15$.

It should be noted that the features in the X direction are better resolved than those in the Y direction due to the horizontal polarization of the THz beam [150]. A better resolution in the Y direction can be expected when the THz field is vertically polarized, and to get a better resolution for features in all direction, a circularly polarized THz field may be required. Since the strip separations in elements 3-1 and 3-2 are 62 μm and 55 μm but the sampling pixel is 32 μm, we can see strong pixelization effects in the experimental data. The pixelization makes the reconstructed image blurred, and further limits the resolution of our scheme. Through the simulations shown in the later section, we find that the resolution of our configuration (with a 32 μm pixel size) is less than 35 μm. This resolution limit can be further improved to 11 μm ($\lambda/86$) if the pixel size is 8 μm. Another interesting observation from the simulation shows that a longer central wavelength can provide a better spatial resolution. This counter-intuitive conclusion comes from the nature of near-field imaging. As analyzed in the previous work [154], for the diffraction field of a sub-wavelength object in the near-field region, a small ratio of z/λ can maintain more features, where z is the propagation distance. Therefore, the factors that limit the spatial resolution include the polarization of the illumination, the pixel size, the thickness of the detection crystal, the central wavelength of the THz pulse and the separation between the detection crystal and object. Thus, we can further improve the resolution to few microns through illuminating a longer wavelength THz pulse on a thinner crystal with a larger nonlinearity, as well as encoding the probe beam with a smaller pixel size and moving the sample closer to the detection crystal [155, 126].

Note that, our scheme can probe any portion of the THz field without changing optics. This is because that we can change the location of the NIR probe on the THz field through the change of the location of the encoding masks on the SLM using Matlab. For instance, the results that we show above use the central part of the SLM for encoding, which yields a reconstructed field of the central part of THz field.

7.5 Comparison of different imaging algorithms

As what we introduce in the last chapter, raster scanning is the prevalent single-pixel sampling technique due to the lack of economical high performance THz cameras. The limitations in speed and contrast become apparent when the total number of sampling points increases. With a finer sampling and an increased number of pixels, the SNR on each pixel is reduced due to the reduction in the signal level on each pixel. As a result, one needs to significantly increase the integration time in order to average out the noise. Furthermore, finer sampling also requires very precise mechanical controls. As a comparison, SPI removes the requirement of mechanical scanning, which results in an accurate sampling control. Because multiple pixels are sampled in each measurement, the limitations due to the detector noise are mitigated.

Moreover, different algorithms can provide various benefits in image quality and reconstruction speed.

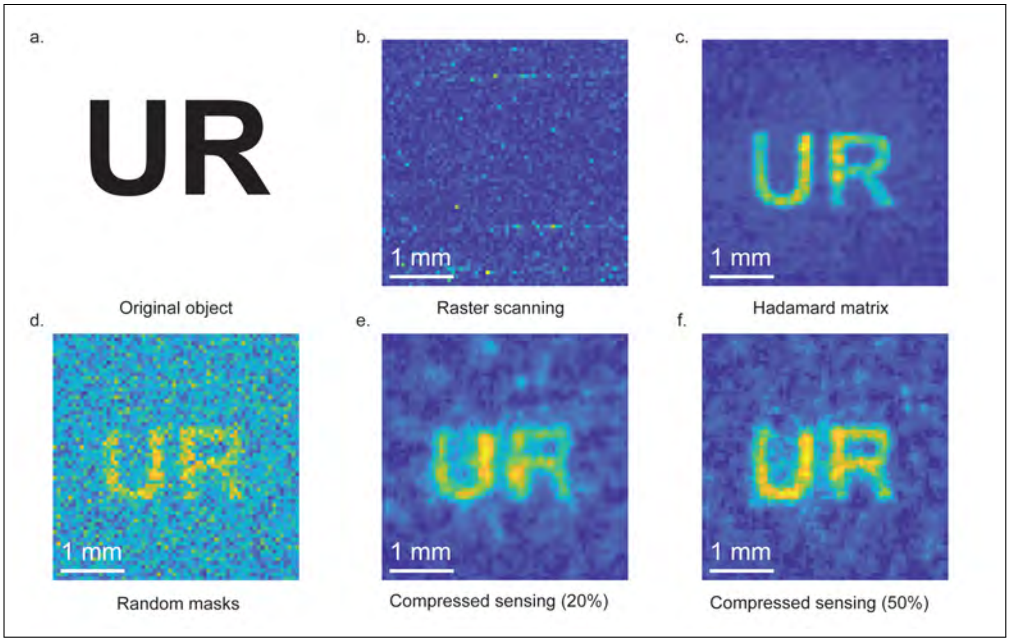

Figure 7.3: (a). Original "UR" object. (b). Field distribution obtained by raster scanning. (c). Field distribution reconstructed by HM algorithm. (d). Reconstructed field obtained by random masks. (e) and (f). Recovered field through the use of CS with different sampling ratios.

To directly show the advantage of SPI, the experimental comparison of raster scanning, HM and CS algorithms is shown in Figure 7.3. The object is a positive "UR" mask (Fig. 3(a)) with a 300 μm line width ($\lambda_c/3.13$). In theory, the raster scanning requires to illuminate each pixel sequentially and record the THz signal for the corresponding pixel. In terms of the SNR, this approach is identical to use a camera to simultaneously measure all pixels, and will not reveal any information of the field if the signal on each scanning pixel is smaller than the detector noise. Therefore, to make this comparison more convincing, we intentionally increase the pixel size from 32 μm to 64 μm to give a favor to raster scanning. In this case, the incident power on each pixel is 4 times larger than the recovered field shown in Figure 7.2(b) but the intensity is same. Even in this scenario, comparing the recovered normalized field distributions obtained from raster scanning (Figure 7.3(b)), random binary masks (Figure 7.3(d)), HM (Figure 7.3(c)) and CS (Figure 7.3(e) and (f)), we can see that all the computational algorithms can reveal the image of the object scanning under the same acquisition time. This is because for the pixel size of 64 μm, which is much smaller than the wavelength, the signal of the THz field on each single pixel is still less than the detector noise. Therefore, the results measured by raster scanning only gives the detector noise but not reveal any spatial information about the THz field. Note that the bright central part of the "UR" comes from the non-uniformly distributed THz field.

Comparing the results from all computational algorithms, HM provides the best contrast, while the image reconstructed from random masks is the noisiest, which matches the expectation. By sub-sampling the field with a 20% sampling ratio, the CS yields a field distribution with 89.6% fidelity. Fidelity is defined as the correlation coefficients between the recovered THz field and the original object. With a 50% sampling ratio, we can achieve 96.9% fidelity, which is mainly limited by the background noise. One can further improve the fidelity by adding more image processing algorithms in the restoration stage. Therefore, we believe that the field recovered by the CS algorithm with a 50% sampling ratio could be the best choice for real applications. This comes from the fact that high fidelity field distributions are accessible with only half of the original total acquisition time (compared to HM algorithm) by sacrificing a tolerable information.

A faster acquisition time is mainly limited by the low switching speed of the SLM (60 Hz), and will be further limited by the repetition rate of our laser (1 kHz) if a high-speed (kHz-level) digital micromirror devices (DMDs) is used as the new SLM. Since a THz field with a uniform spatial distribution is the only requirement for field reconstruction with a high quality, spintronic THz emitters pumped by a high repetition rate oscillator laser can be employed for ultrafast sampling [156], which can lead to real-time beam profiling and future integrated THz imaging devices [157]. As what we discuss before, this approach has no physical limitation in sampling speed as what is demonstrated in Ref. [150, 151, 158, 159], and hence a faster imaging rate can be achieved once a high speed SLM and a high repetition rate laser are implemented.

7.6 Simulation results

To figure out the limiting factors in our system, we numerically simulate the entire sampling process with different sets of parameters. Before we start figuring out the limiting factors in resolution, it is convenient to show the

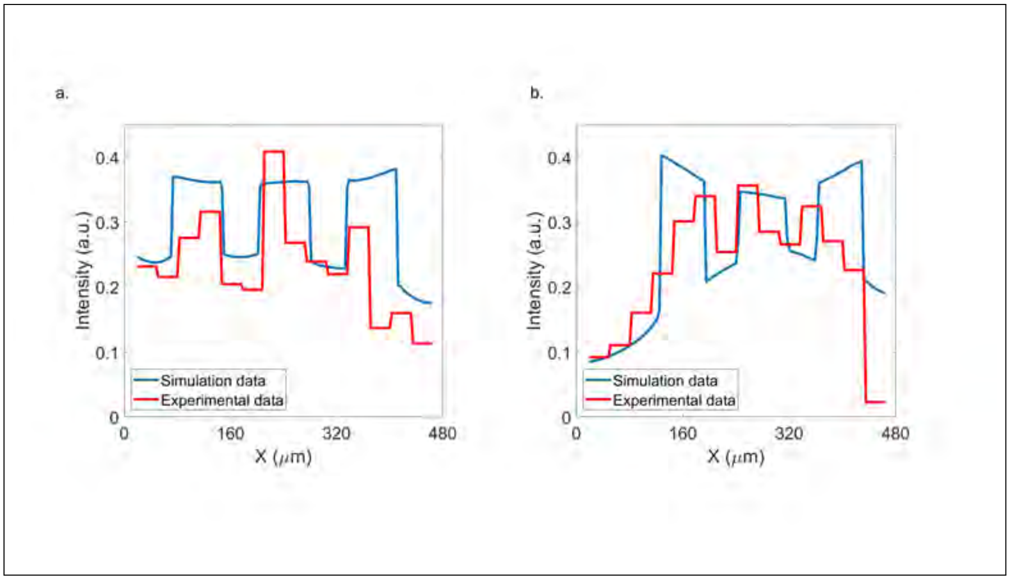

Figure 7.4: (a) and (b) are intensity cross sections of element set 3-1 and 3-2 in Figure 7.2(b) in the main text respectively.

resolution we have in the experimental data.

As what we discuss before, the resolution here is defined as the size of the smallest resolvable feature in the image of the object. The criterion to justify whether the feature can be 'resolved' is Rayleigh criterion, which yields a 20% contrast ratio if the feature is barely resolved. Therefore, in our resolution estimation procedure, we first take the intensity cross sections of different element sets and then calculate the contrasts. As shown in Figure 7.4, the intensity cross sections of element set with d = 55 μm and d = 62 μm are shown. From these two plots, the average contrast ratio can be found as 18.10% and 32.28% respectively. As a result, we can claim that the resolution is 62 μm. However, due to the pixelization issue, one can find that the contrast ratio of the experimental data of d = 55 μm is slightly worse than the simulation data, and we will show that this pixelization problem is the strongest factor limiting the resolution in the discussion later. Therefore, the theoretical resolution should be 49 μm for our experimental setup.

Now we will figure out the role of three different parameters in resolution: the thickness of detection crystal, the pixel size and the central wavelength of the THz pulse.

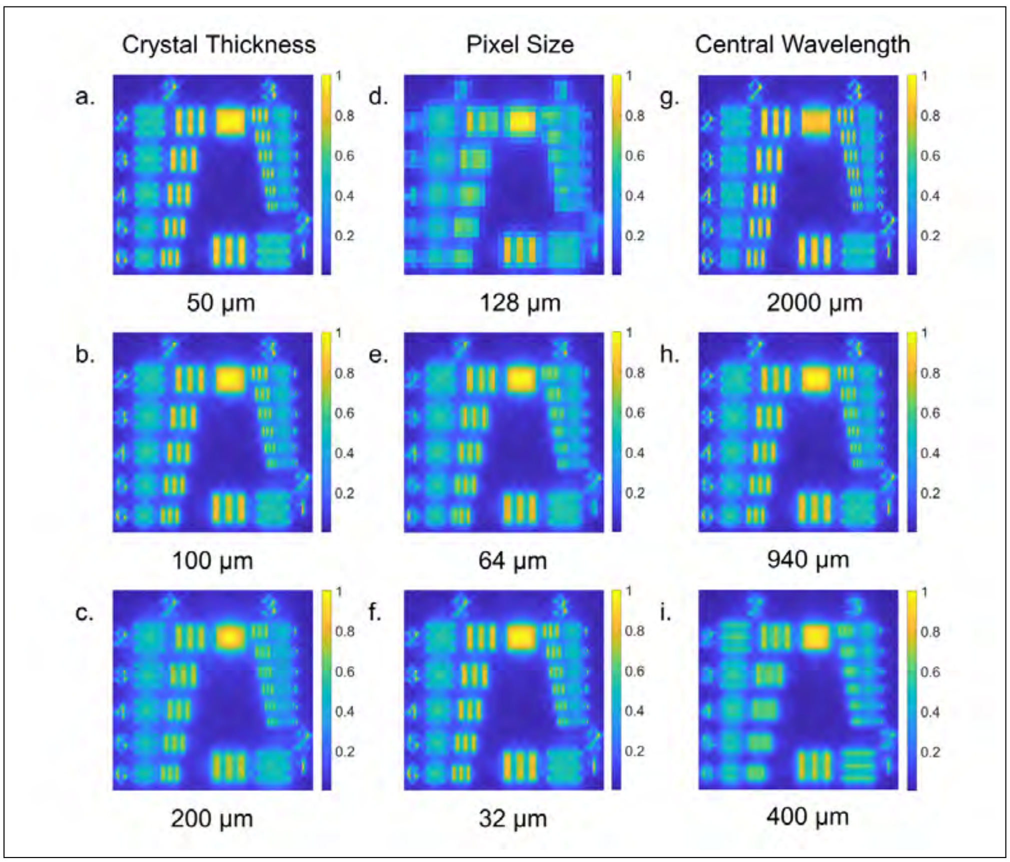

Figure 7.5: (a) to (c): Normalized results with different crystal thicknesses. (d) to (f): Normalized results with different pixel sizes. (g) to (i): Normalized results with different central wavelengths.

Three different thicknesses of detection ZnTe crystal are chosen with a 32 μm pixel size and 128 pixels: 50 μm, 100 μm and 200 μm. The central wavelength is 940 μm. As shown in Figure 7.5(a)-(c), the reconstructed field with 50 μm crystal thickness is the most clear one. By calculating the contrast of each element using the same method as mentioned in the main draft (the example of the cross sections can be found in Figure 7.6(c)), we find that with 50 μm and 100 μm detection crystal thicknesses, even the element 3-6 (d = 35 μm) can be fully resolved with a 35.36% contrast and a 28.47% contrast respectively. As a comparison, the resolution in Figure 7.5(c) is only 88 μm with a 20.79% contrast. If we can further reduce the crystal thickness to 20 μm with a 8 μm pixel size, as shown in Figure 7.6(d), the resolution can easily reach 8.8 μm with a 30.00% average contrast. The reason why we change the pixel size here is that, from the comparison below, a large pixel size can strongly limit the resolution even though the thickness is small. Therefore, to reduce the pixelization effect, we change the pixel size to a lower level for a fair comparison. Therefore, we can conclude that a thin detection crystal can significantly increase the resolution. However, we should note that a thinner crystal will inevitably leads to a weaker signal, and hence a worse SNR in the recovered image. Thus, a thinner crystal might not be the first choice if we pursue a better resolution.

Next, three different pixel sizes are simulated under a 100 μm thick detection crystal with a 940 μm central wavelength THz pulse: 128 μm, 64 μm and 32 μm. Since our field size is fixed, the number of pixels in each case then becomes 32, 64 and 128 respectively. The recovered figures are shown in Figure 7.5(d)-(f) respectively. Through calculating the contrast using cross sections (as shown in Figure 7.6(b)), the resolution in Figure 7.5(d) is 125 μm and the contrast is only 22.08%. As the comparison, the resolution in Figure 7.5(e) is 88 μm with a 25.96% contrast while the resolution in Figure 7.5(f) is less than 35 μm as we discussed in previous paragraph. These results shows that the pixelization effect can significantly reduce the resolution and contrast, and one can expect a better resolution if we use a smaller pixel size. Therefore, as shown in Figure 7.6(e), when we decrease the pixel size to 8 μm, the resolution is found to be 11 μm ($\lambda/86$) with a 33.7% average contrast. This can be understood by the Nyquist sampling theorem. When the spatial frequency provided by the sampling devices is not high enough to measure the high spatial frequency components carried by the electromagnetic field, these high frequency terms will lost in the measurement stage leading to a much blurred image. Therefore, optical SLMs are more favorable than THz SLMs in computational imaging since the pixel size is much smaller, which indicates that a higher spatial frequency can be measured. One should note that since the pixel size cannot be infinitely small, the resolution in our approach will be limited by the pixel size projected on the detection crystal, which is a common resolution limit of computational imaging methods. Comparing to a thinner crystal, reducing the pixel size will not sacrifice any SNR but lead to a increasing data acquisition time if the entire field size is fixed. Thus, if a faster sampling speed is available or imaging time is not the first priority, reducing the pixel size would be the best choice to increase the resolution in THz SPI.

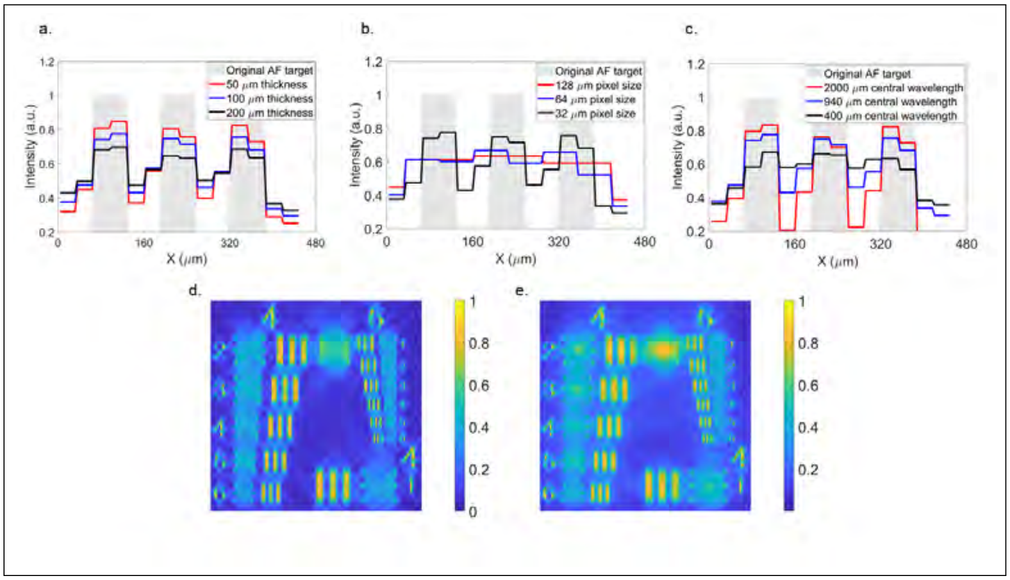

Figure 7.6: (a). The intensity cross section comparisons with different crystal thickness. (b). The intensity cross section comparisons with different pixel sizes. (c). The intensity cross section comparisons with different central wavelengths. The gray stripes stands for the intensity cross section of element 3-1 in the original AF target. (d). Recovered image with 20 μm thick detection crystal and 8 μm pixel size. (e). Recovered image with 100 μm thick detection crystal and 8 μm pixel size.

Last but not least, three different central wavelength with the same spectrum shape are analyzed with a 100 μm thick detection crystal: 2000 μm, 940 μm, 400 μm. The number of pixels is 128 so that the pixel size is 32 μm. Note that even the central wavelength has shifted, the shapes of the spectrum are same for all three cases. Intuitively speaking, Figure 7.5(g) (2000 μm central wavelength) has the best contrast while Figure 7.5(i) is the worst. By calculating the contrast of the elements in all three figures (the example of the cross sections can be found in Figure 7.6(c)), we find that the resolution in Figure 7.5(i) is only 125 μm with a 21.05%. That is to say, in the sub-wavelength region, the resolution in Figure 7.5(i) is worse than the resolution in Figure 7.5(c) even the detection crystal is much thinner. However, the resolution in Figure 7.5(g) should be much less than 35 μm since the contrast of element 3-6 is found to be 48.11%, which is much higher than the contrast of the same element in Figure 7.5(a). Therefore, in the near-field region, a longer central wavelength pulse will provide a better resolution even when the detection crystal is thicker. The conclusion here is very different from the conclusion in far-field imaging where a shorter wavelength is always desired for a higher resolution.

Then we want to numerically compare our method to the conventional THz EO imaging. The conventional near-field EO imaging utilizes a similar detection method as ours [160, 161]. One can use an optical CCD array to retrieve real-time images of the THz field. Unlike other near-field imaging techniques, this EO imaging technique also provides noninvasive measurements with a concise and reliable setup. However, the resolution of this technique is not as good as our approach especially when the crystal goes thicker. The resolution limitations in both cases highly depend on the thickness of the detection crystal. However, this factor has less impact in our case because we measure the total electrical field of each spatial pattern as shown in Eq. (7.3), which is an accumulation result through the whole thickness of detection crystal. Therefore, we can find a position z' where the product of THz field, the i_{th} spatial pattern and the thickness of the crystal d is exactly equivalent to the integral in Eq. (7.3). That is to say, we can rewrite the Eq. (7.3) into another form:

$$\begin{aligned} P_{\mathrm{s},i}(t) =& \int\int\int_{z_0}^{z_1} \frac{1}{c} I_i(x,y,z,\omega_1)\omega_1 L n_0^3(\omega_1) r_{14}(x,y)\times \\ & E_{\mathrm{THz}}(x,y,z,\omega_{\mathrm{THz}},t)dxdydz \\ =& \int\int \frac{1}{c} z' I_i(x,y,z',\omega_1)\omega_1 L n_0^3(\omega_1) r_{14}(x,y)\times \\ & E_{\mathrm{THz}}(x,y,z',\omega_{\mathrm{THz}},t)dxdy, \end{aligned} \tag{7.5}$$

where $E_{\mathrm{THz}}(x,y,z',\omega_{\mathrm{THz}})$ and $I_i(x,y,z',\omega_1)$ are THz field and i_{th} spatial pattern at distance z' respectively. Note that z' is less than z_1 so that the THz field at z' is less diffracted than the field at z_1. Therefore, what the computational imaging recovers is not the field at the end of detection crystal but the field at position z'. However, in the EO near-field imaging case, what the camera measures is the transverse structure of the THz field at the rear surface of detection crystal (i.e., z_1), which is more blurred due to the relatively stronger diffraction. In another word, when the detection crystal has a thickness $d = z_1 - z_0$, the field recovered by the computational imaging method with this crystal is equivalent to the field imaged by EO imaging with a thinner crystal thickness $d' = z' - z_0$. This difference in the measurement favors the superior resolution in our sampling technique by sacrificing the image acquisition time. Another drawback in the near-field EO imaging is the requirement of high power lasers [162]. As what we discuss before, a thinner crystal can give better resolution but worse contrast and SNR, and the sensors on camera measure the signal separately. Therefore, to get high resolution images with a good contrast, a high energy laser is used to provide a strong THz field in conventional EO imaging. However, in our case, high contrast images can be retrieved with a low intensity pump laser and a extremely weak probe because all the fields are collected by a single-pixel detector.

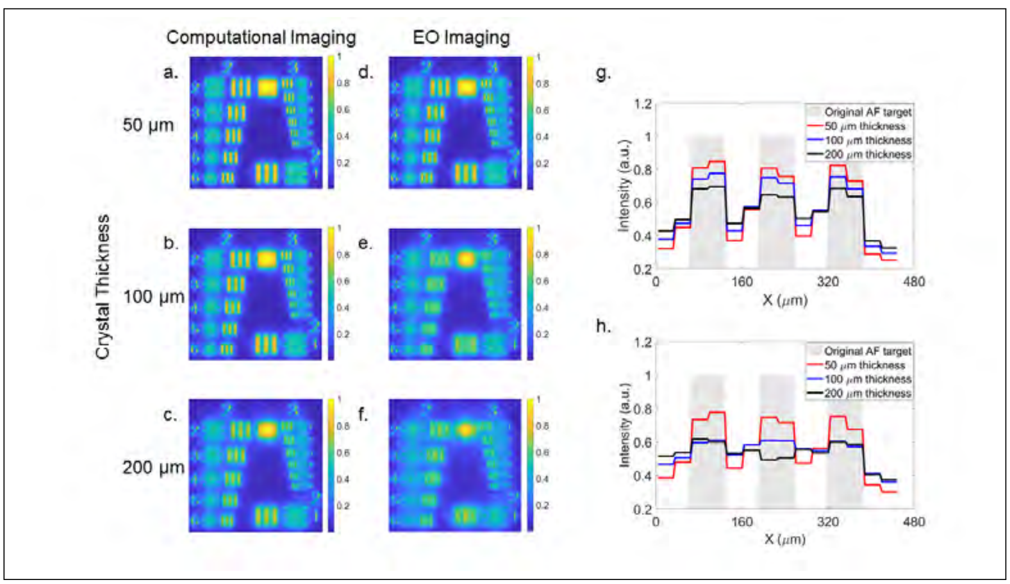

Figure 7.7: (a) to (c). Normalized results using computational imaging methods. (d) to (f). Normalized results using EO imaging methods. The figure (a) and (d) both have a 50 μm thick detection crystal while the crystal thicknesses in figure (b) and (e) are both 100 μm. The crystal thicknesses in figure (c) and (f) are 200 μm. (g) and (h). Intensity cross sections of element 3-1 using computational imaging and EO imaging respectively.

To intuitively show the comparison, we compare the reconstructed images from computational imaging and the images from near-field EO imaging with different thicknesses of the crystal. As shown in Figure 7.7(a)-(c), three different images with thicknesses 50 μm, 100 μm and 200 μm are reconstructed. To keep the comparison fair, this set of images all have 128 pixels with 32 μm pixel size. After calculating the contrast of each element from intensity cross sections (as shown in Figure 7.7(g) and (h)), the element 3-6 (d = 35 μm) can still be fully resolved in Figure 7.7(d) but with a 26.11% contrast, which is much lower than the contrast using computational imaging method in Figure 7.7(a). For Figure 7.7(e) and (f), there is no element can be resolved. That is to say, our computational imaging method can significantly improve the resolution especially when the detection crystal is quite thick, which matches our prediction. Therefore, for applications requiring a thick detection crystal, our approach can provide much better performance than the conventional EO imaging. Therefore, under the same conditions, our computational method is superior than the conventional EO imaging in resolution and contrast with a sacrifice of imaging speed.

7.7 Discussion

We have demonstrated that our near-field spatial sampling technique through the use of a spatially encoded probe can provide a sub-wavelength resolution with a high fidelity, and shown the possibility of improving this technique to achieve real-time THz imaging with both amplitude and spectral information via simulations [146, 159]. In comparison to raster-scanning methods, our approach provides a better sampling accuracy, resolution, and contrast. These advantages are facilitated by computational algorithms that offer a general advantage over all THz imaging methods based on raster scanning [148, 163].

In relation to the EO imaging [125, 126], as what we compare in the simulation section, we do not measure the THz spatial profile directly, but recover the transverse field distribution through the use of computational algorithms. This measurement gives rise to a better performance in both resolution and contrast without requiring high power lasers, especially when the detection crystal is thick [162].

Regarding the computational imaging approaches with dedicated THz SLMs, the advantages in our method mainly comes from the use of optical SLMs. As what we discuss before, THz SLMs usually have a lower modulation rate which is impractical for real applications. The large pixel size also limits the resolution to few hundreds of microns even in the near-field region [147, 148]. Last but not the least, these inefficiency devices are specially designed and fabricated, which means they are not economical for most applications.

Compared to the imaging techniques using photon-excited free carries, the probe beam encoding also waives the reliance on complicated high-speed synchronization among three arms, which makes the system less complicated both optically and electronically [150, 151, 158, 159, 164]. Another advantage is that there is no physical limit in sampling speed in our approach, so that we can fully utilize the potential of high-speed optical SLMs [151].

In comparison with the novel THz nonlinear ghost imaging technique [152], we believe that our approach can provide a better resolution and SNR. Through encoding the spatial pattern directly onto the pump beam, the THz nonlinear ghost imaging technique can conveniently generate structured THz field to achieve computational imaging. However, this also limit the thickness of the generation crystal, and leads to the tradeoff between SNR and resolution. Therefore, to get an accurate sampling to provide a high resolution, the thickness of the generation crystal has to be limited to a very thin crystal, which may lead to a weak THz field and hence the low SNR recovered image. As a result, our experimental data has a even better resolution ($\lambda/15$) than the simulation data ($\lambda/12$) in their work.

Due to the concise and robust configuration, the probe beam encoding provides numerous advantages over previous works. We believe that our approach can be the ideal approach to be developed as a new generation integrated THz imaging devices for future applications.

Chapter 8

Single-pixel imaging in the time domain

8.1 Brief introduction to ultrafast sensing

Ultrafast pulses usually refer to the electromagnetic pulses with a duration of the picosecond (ps) level or less. The broadband nature of these pulses lead to numerous applications in spectroscopy, high energy physics and plasmonics. However, since these ultrafast pulses have sub-picosecond oscillations, they cannot be resolved by a photodiode and oscilloscope due to low bandwidth nature of electronics. Therefore, traditional approaches, which are used to measure slow time events, are not applicable for ultrafast signals, and new approaches has to be specifically designed. Note that the ultrafast measurement discussed here only focuses on the picosecond and femtosecond pulses. Attosecond technique is beyond the scope of this dissertation.

Similar to the spatial sampling case, the most straightforward idea of measuring an ultrafast pulse is using another shorter event as the probe to sample the unknown pulse, which can be simply achieved by raster scanning either the unknown pulse or the probe pulse. Analogous to the spatial imaging system, the measurement result $P_s(t)$ can be described by the convolution of the probe pulse $E_p(t)$ and unknown pulse $E_{un}(t)$:

$$P_s(t) = E_p(t) * E_{un}(t), \tag{8.1}$$

where we have assumed a coherent measurement of the pulse electric field. In the pulse shape measurement, one can simply replace the electric field terms above with intensity distributions. It is straightforward that when the probe field is a Dirac delta function, the measured signal $P_s(t)$ is identical to the unknown pulse $E_{un}(t)$. Thus, in this raster scanning scheme, a probe pulse with a very short pulse duration is always desired to approximate a Dirac delta function. For example, in THz TDS, the NIR pulse is usually much narrower than the THz pulse and the measurement result can be directly considered as the original THz pulse. When the pulse duration of the probe pulse is not narrow enough, a deconvolution is required to retrieve the unknown pulse $E_{un}(t)$ from $P_s(t)$ and $E_p(t)$.

Even though the method described above is theoretically simple, the experimental realization highly relies on the preparation of a well-characterized short pulse as the probe pulse. Unfortunately, in realistic scenarios, this requirement cannot be always satisfied. Therefore, people develop new methods to measure ultrafast signals. The most straightforward approach is auto-

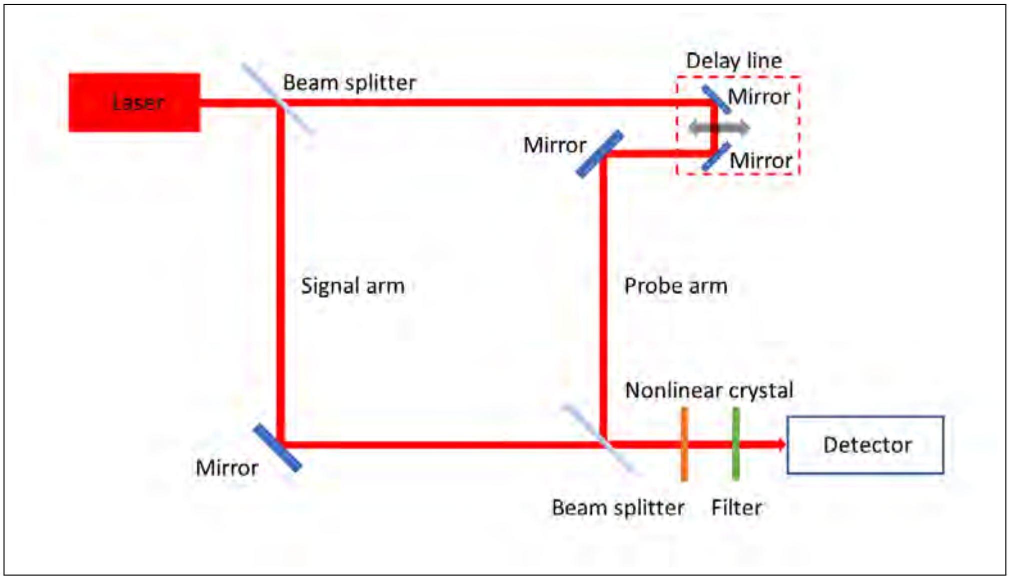

Figure 8.1: Schematic of an interferometric autocorrelator.

correlator, which includes both intensity autocorrelator and interferometric autocorrelator. A typical setup of an interferometeric autocorrelator is shown in Figure 8.1. The beam splitter splits an unknown pulse into two copies, and the relative time delay between them is controlled by a delay line. After the second beam splitter, two pulses are focused on the nonlinear crystal and temporally coincide with each other. By filtering out the fundamental frequency and using a photodiode or photomultiplier tube (PMT), we can solely measurement the signal frequency generated by the sum frequency generation in the nonlinear crystal, which further results in the pulse duration information of the unknown pulse. It is worth noting that if the intensity autocorrelator is implemented, the phase information will not be available. One advantage of autocorrelator is reference-free so that no requirement of a well-characterized short pulse is required. Meanwhile, single-shot measurement is also available if one use cylindrical lens to focus the pulse and a camera to perform the measurement. If a very thin crystal is used so that the group velocity mismatch can be reduced, autocorrelator is also suitable for very short pulses (less than 10 fs). However, we should note that the autocorrelator relies on the nonlinear process which indicates the fact that, for weak pulses, this method is not applicable. Moreover, due to the nature of autocorrelation, pulse measurement, especially the pulse shape, cannot be accurate if the pulse shape of the unknown pulse $E_{un}(t)$ is asymmetric. When the pulse shape of $E_{un}(t)$ is highly distorted, the result from autocorrelator might be misleading as well. Moreover, for very short pulses, the thin crystal is required for an accurate measurement, which will inevitably lead to a poor SNR and a limited phase-matching bandwidth.

One solution to these problems is the famous frequency-resolved optical grating (FROG), which is developed by Dr. Rick Trebino's group [165]. The difference between an autocorrelator and a FROG is the measurement. Rather than using a simple photodiode or PMT, a spectrometer is implemented to measure multiple spectra under different time delays. A FROG trace, which is a spectrogram showing the spectra at different time delays, is generated and used to recover the pulse shape via a phase retrieval algorithm. FROG can provide accurate pulse measurement, including both amplitude and phase, even for short pulses at few fs and highly distorted pulses. Therefore, FROG can solve many problems in autocorrrelator and become a popular method for ultrafast sensing. However, the requirement of sensitive spectrometers or cameras (in GRENOUILLE) makes this approach not suitable for wavelengths, such as THz band, where sensitive spectrometers and cameras are not available [166]. Meanwhile, as what we discuss in the last chapter, the sensitivity of spectrometers and cameras is usually worse than the single-pixel detectors, for example PMTs. Therefore, the sensitivity is not as good as autocorrelator. Last but not least, the accuracy of phase retrieval algorithm highly relies on the calibration of the FROG trace over the desired frequency bands. Therefore, for very broadband pulse measurements such as THz pulses, a complicated calibration is necessary.

Another approach is spectral shearing interferometry, which can provide a comprehensive measurement of pulses as well. One famous setup is called Spectral Phase Interferometry for Direct Electric-field Reconstruction (SPIDER) [167]. The system is more complicated than FROG but still shares a similar structure to the autocorrelator. The pulse in the signal arm is splited into two copies which are spatially overlapped but temporally separated. The probe pulse is strongly broadened via a diffraction grating. The signal pulse and probe pulse are then combined in a nonlinear crystal to generate sum-frequency signals. Since the two copies in the signal arm are temporally separated, these two copies interact with different frequency components in the sum-frequency generation, which becomes a spectra shear interferometry. By varying the time-delay between two copies and the relative time between the signal and probe pulses, one can recover the spectral phase and thus the entire pulse. As one can seem SPIDER can solve the disadvantages in autocorrelator as well. Comparing to FROG, even though SPIDER does not require any complicated phase retrieval algorithm and pre-calibration of FROG trace, FROG has a simpler system which is usually easier and more reliable to operate. However, similar to FROG, the requirement of sensitive spectrometer and camera still limits this technique to a few frequency bands and the sensitivity would be less compared to techniques using single-pixel detectors.

Time lens is another novel technique developed for ultrafast sensing [168, 169, 170]. The underlying physics of time lens is the mathematical equivalence between diffraction and dispersion, which comes from the spatio-temporal duality of light pulses. Therefore, similar to the functionality of a lens, time lenses can temporally image the ultrafast pulse with a magnification so that the stretched pulse has the same pulse shape but a longer pulse duration. When the magnification is large enough, the stretched pulse will be measurable to slow electronics and hence the ultrafast sensing becomes straightforward. The quadratic phase can be applied to pulses via phase modulator or nonlinear processes. This technique is very convenient in the measurement stage since the stretched pulse can be ns-level. Therefore, a single-pixel detector with a high bandwidth is good enough for ultrafast sensing, and the pulse shape can be directly readout through an oscilloscope. However, designing a time lens is not straightforward. One has to carefully engineer the dispersion in the material so that the quadratic phase can be correctly applied to the spectra. If this is accomplished by the nonlinear photonic platform, phase matching condition has to be satisfied as well to provide efficient operation. Since a uniform dispersion is not universally available for any frequency bands, which is the same as the spatial case, time lenses designed for one frequency band will becomes incompatible for another frequency band. Thus, the commercial ultrafast sensing devices using time lenses are still not developed. Furthermore, the narrowband nature of time lenses also leads to the failure of measuring broadband pulses.

All techniques mention above solely need one single laser for the operation. If multiple lasers are implemented, new techniques, for example asynchronous optical sampling, can be developed as well. However, we will not discuss these techniques here due to the complicated setup of these multi-laser systems.

8.2 Concept of time-domain single-pixel imaging

From the discussion above, we can find the lack of an ultrafast sensing system which can provide a high sensitivity for multiple frequency bands, especially for those frequency bands that high performance spectrometers and cameras are not available. Coincidentally, such difficulties also exist in spatial imaging at wavelengths where cameras are not available or impractical, and based on the concept and history of SPI introduced in the previous chapter, we know that SPI has emerged as a promising technique for solving this difficulty. Therefore, if we can develop a temporal analog of SPI, it will be a possible ultrafast sensing technique which can provide a sensitive measurement for multiple frequency bands.

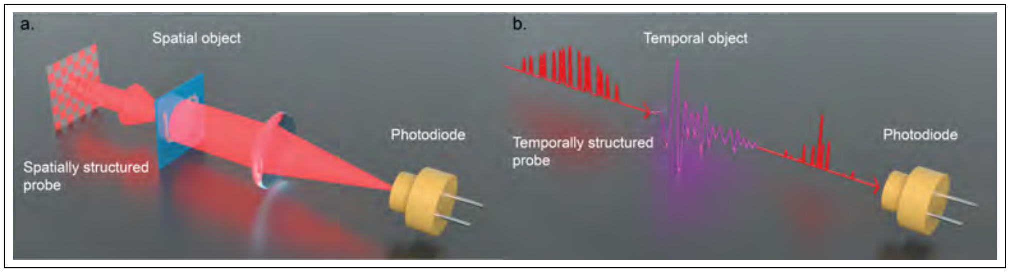

Figure 8.2: Analogy between single-pixel imaging and time-domain single-pixel imaging. (a). A typical single-pixel imaging configuration. The photodiode is the bucket detector which has only one pixel and hence provides no spatial resolution. (b). Our proposed time-domain single-pixel imaging configuration. Analogously, the slow photodiode, which lacks the temporal bandwidth to resolve ultrafast signals by itself, works as the "single-pixel" detector in the time domain.

Before we introduce the concept of time-domain single-pixel imaging (TSPI), it is convenient to firstly clarify the analogies which we make in the development of the concept, which is shown in Figure 8.2. A spatial image is a 2D distribution of the electromagnetic field, and can be directly measured using pixelated sensor arrays because these devices provide accurate spatial sampling of the electromagnetic field. As what we show in the last section, the sampling size will impact the resolution of the measured image as well because of the Nyquist sampling theorem. Thus, in the extreme case where our camera only has one pixel so that no spatial resolution can be provided, it cannot resolve the image unless raster scanning or SPI is implemented. When we use SPI to image the field, a spatially structured probe is used to provide the spatial sampling. Therefore, the image can be recovered even the detector is a single-pixel detector without any spatial resolution. Imaging a temporal object can be accomplished analogously through the use of a time-resolving detector. In order to temporally resolve the object, the detector should have a high bandwidth to provide a sufficient sampling rate, which is the temporal analog to the spatial resolution of a sensor array. When this temporal sampling rate, i.e. the bandwidth of the detector, is much lower than the oscillation of the ultrafast signal, high frequency terms will lost and the measured signal will be distorted. Therefore, a slow detector whose bandwidth is much less than the frequency of the unknown signal is the 'single-pixel' detector in the time domain.

Based on the analogies we make above, it is obvious that all ultrafast sensing techniques mentioned above have to follow the Nyquist sampling theorem, and hence a 'single-pixel' detector in the time domain, or frequency domain, cannot be used if a comprehensive measurement is desired. For example, in time lenses, even the pulse gets stretched, fast photodiodes at 100 GHz-level are usually required to provide enough sampling to high frequency terms. As a comparison, TSPI should have no requirement of the bandwidth of detectors since the temporal sampling is provided by the temporally structured pulse rather than the detector. That is to say, even kHz-level photodiodes, which are "single-pixel" detectors in the time domain, can be used to measure sub-ps-level oscillations without any mechanical scanning. Furthermore, TSPI inherits other advantages of spatial single-pixel imaging: increased sampling efficiency, flexibility for diverse wavelengths and high sensitivity for weak signals. Therefore, TSPI can link the ultrafast optical signals with slow electronics.

Now, we assume that we have a temporal modulator called programmable temporal fan-out (TFO) gate, which is the temporal analog of spatial fan-out that can duplicate an incoming light pulse into spatially separated replicas [61, 171, 172, 173]. TFO can duplicate the input ultrafast pulse into coherent replicas separated in the time domain, forming an ultrafast pulse train. If the TFO gate is programmable, an ultrafast pulse train with a variable temporal interval and arbitrary temporal structure can be deterministically prepared.

Based on the assumption above, the theoretical model of TSPI can be developed. Assume that our input ultrafast pulse is horizontally polarized, and has a carrier frequency of ω_0 with a pulse duration equal to τ_w. We can write the input pulse $E_{in}(x, y, z, \omega_0, t)$ propagating in the z direction as the following:

$$E_{\mathrm{in}}(x, y, z, \omega_0, t) = A_0(x, y) \exp\left(-\frac{t^2}{\tau_w^2}\right) \exp\left(i\omega_0 t + i\vec{k} \cdot \vec{z}\right), \tag{8.2}$$

where $A_0(x, y)$ is the transverse amplitude distribution. Since the input pulse is propagating along z direction, the dot product of wave vector $\vec{k}$ and longitudinal coordinate $\vec{z}$ will be just a scalar product kz. After TFO gate, we get a sequence of replicas $E_{\mathrm{TFO}}(x, y, z, \omega_0, t)$ which are separated by the temporal interval $\Delta\tau$:

$$
\begin{aligned}
E_{\mathrm{TFO}}(x, y, z, \omega_0, t) = &\sum_j A_j(x, y) \exp\left(-\frac{(t - j\Delta\tau)^2}{\tau_w^2}\right)\times \\
&\exp(i\omega_0(t - j\Delta\tau) + ikz),
\end{aligned}
\tag{8.3}
$$

where$A_j(x, y)$ is the amplitude of the jth replica. Eq. (8.3) represents a field consisting of sequence of pulses with duration τ_w and amplitude $A_j(x, y)$ located at temporal position $j\Delta\tau$.

When we use the field shown in Eq. (8.3) as the probe pulse to sample the temporal object, which is a THz pulse $E_{\mathrm{THz}}(x, y, \omega_{\mathrm{THz}}, t)$, the signal $P_{s,i}$ from the balanced detector can be found as:

$$
\begin{aligned}
P_{s,i} = &\int\int \frac{1}{c}|E_{\mathrm{TFO.i}}(x, y, \omega_0, t)|^2\times \\
&\omega_0 L n_0^3(\omega_0) r_{41} E_{\mathrm{THz}}(x, y, \omega_{\mathrm{THz}}, t) dxdydt,
\end{aligned}
\tag{8.4}
$$

where $E_{\mathrm{TFO.i}}(x, y, \omega_0, t)$ stands for the output pulse train of TFO has been modulated by the i_{th} row of the sampling matrix, and c is the speed of light in vacuum. L is the thickness of the detection crystal, and ω_0 is the frequency of probe. $n_0(\omega_0)$ is the refractive index of the detection crystal at frequency ω_0, and r_{41} is the EO efficient of the detection crystal. From Eq. (8.4), we can see that the THz pulse can only be detected when that part of the THz pulse is temporally coinciding with a TFO replica. Therefore, temporally modulating the structure of TFO output $E_{\mathrm{TFO}}(x, y, z, \omega_0, t)$ is equivalent to temporally modulating the THz field in the same manner but leaving the probe field unchanged. However, as what we discuss in the last chapter, temporally encoding the probe beam can be achieved using commercially available NIR devices, and releases the requirement of ultrafast THz temporal modulator, which, to the best of our knowledge, has not been reported yet.

Now we assume that our THz pulse is temporally sampled N times, and the measured pulse is represented by a N dimensional vector ψ. The measurement basis is S, and according to what we show before, to fully take advantage of CS, we will use Walsh-ordered HM as the sampling basis. The corresponding coefficient vector is ϕ, which consists of measurement results on the balanced detector $P_{s,i}$. Thus, by using CS, we can recover the THz pulse ψ from S and ϕ. From a practical point of view, we use the Total Variation Minimization by Augmented Lagrangian and Alternating Direction Algorithms (TVAL3) package, which provides 4 different total variation based minimization models to solve the minimization problem. The package was provided by Chengbo Li, Wotao Yin and Yin Zhang at Rice University [174]. Figure 8.3 shows the simulated fidelity and RMSE as functions of compression ratio (CR) under different pulse durations. We show that the performance of our SPTI only slightly depends on the pulse duration of the input pulse of TFO gate, which demonstrates that our approach is practical to different pulse durations.

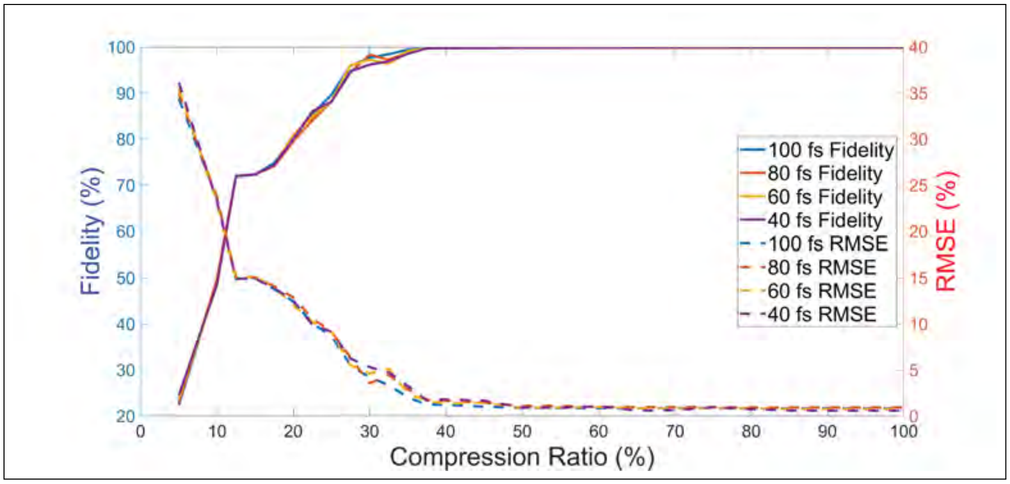

Figure 8.3: Fidelity and RMSE of recovered THz pulses as functions of CR under different input pulse durations.

8.3 Experimental realization

As what we discuss in last chapter, the most challenging step in SPI is the deterministic modulation of spatially structured beam. In TSPI, the difficulty is the deterministic preparation of temporally structured pulse. Once again, we would like to address that a deterministic sampling basis is more favorable than random sampling basis in terms of the sampling efficiency and the data acquisition time. In fact, some primary researches on TSPI were done in the past few years, for example, temporal ghost imaging [175, 176, 177, 178, 179, 180, 181, 182]. However, previous demonstrations did not achieve sub-ps-level ultrafast sensing due to the difficulty of deterministically preparing temporally structured pulses with fs-level modulation. The best modulation is at 10-ps level which comes from the randomness of the incoherent laser source. As a comparison, we develop a programmable TFO gate based on a commercially available DMD, with a minimum temporal sampling size $\Delta\tau = 16.00\pm0.01$ fs. With this TFO gate, we can deterministically prepare temporally structured pulse at 10-fs level sampling accuracy, which, to the best of our knowledge, is the record.

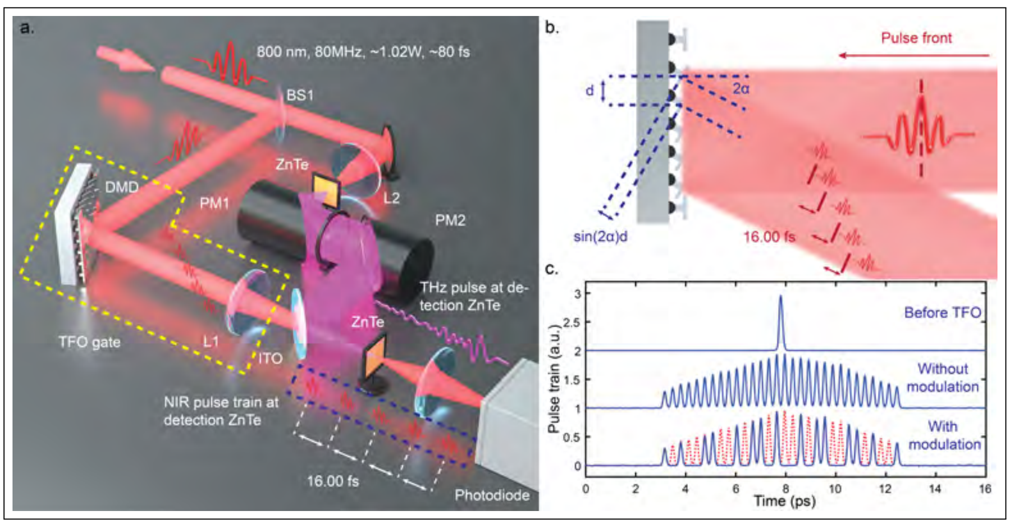

Figure 8.4: Schematics of the experimental setup and the structure of the TFO gate. (a): Experimental configuration. (b): A detailed sketch illustrates the layout of DMD and how its geometry leads to our TFO. (c): Examples showing how the TFO works.

The experimental realization of the entire system is shown in Figure 8.4(a). One terahertz (THz) pulse with about 3 V/cm peak electric field and 5 fJ pulse energy works as the temporal object in the current system. The yellow dashed box indicates our TFO gate which consists of a DMD (Texas Instruments DLP3000) and a lens (L1), and the blue dashed box indicates the prepared ultrafast pulse train at the detection ZnTe crystal plane. The entire system is very similar to the conventional THz TDS except that the temporal structure of the probe pulse is deterministically modulated via our TFO gate.

A 800 nm NIR laser pulse (Maitai oscillator laser from Spectra-Physics) with 80 fs pulse duration and 80 MHz repetition rate is split by a 45:55 non-polarizing beam splitter (BS1). The average power is 1.02 W which corresponds to 12.75 nJ pulse energy. The diameter of the probe pulse is expanded to 30 mm by two lenses with focal lengths equal to 75 mm and 500 mm, respectively (not shown in figure). One rectangular aperture stop (3.7 mm by 6.6 mm, not shown in figure) is used to select the central part of the expanded probe pulse, providing a relatively uniform intensity distribution. The selected probe pulse is then incident on the DMD. Note that, our DMD chip is the most basic one which has a medium micromirror size, a small amount of micromirrors and a small total size of the mirror array. Therefore, by using a more advanced commercially available DMD with a smaller mirror size (a shorter $\Delta\tau$, e.g. $\sim$11 fs), a larger N (e.g. 2560) and a larger temporal field-of-view (a larger T, e.g. $\sim$28 ps), one can easily extend the potential applications of our scheme. After DMD, a 250-mm-focal-length lens (L1) is used to perform the Fourier transform, and the detection ZnTe crystal ($10\times10\times3$ mm) is placed at the Fourier plane. In the signal arm, a delay stage (not shown in the figure) with two mirrors is used to measure THz waveforms for comparison. The NIR pulse is then focused onto an 1-mm-thick ZnTe crystal using a 75-mm focal length lens (L2) to generate

THz pulse. Two 4-inch-focal-length parabolic mirrors (PM1 and PM2) are used to collimate and refocus THz pulses onto the detection ZnTe. An ITO-coated glass plate is used as a dichroic mirror to combine THz and probe beams. After the detection crystal, a conventional EO sampling detection unit is used, which consists of a quarter-wave plate, a Wollaston prism and a balanced photodiode detector (Hamamatsu Photonics S2386-8K). The signal from the balanced photodiode detector is finally measured by a lock-in amplifier (Stanford Research Systems SR830). The acquisition time of each measurement (one pattern on DMD or one temporal position on delay stage) in either TSPI or delay stage raster scanning is the same (100 ms). However, the integration time (time constant) on lock-in amplifier is different. The delay stage raster scanning has a integration time of 100 ms while the TSPI data is 30 ms to avoid the rolling average on lock-in amplifier. Therefore, the SNR of each measurement in delay stage raster scanning is 1.83 times stronger than the TSPI data.

The geometry and layout of the DMD are shown in Figure 8.4(b). The dark red arrow shows the propagation direction of input ultrafast pulse, and before the DMD, there is no time delay in the pulse front of the incident pulse, which is represented by dark red lines. After the DMD, N spatio-temporally separated fan-out replicas are generated [183]. L1 is used to perform a Fourier transform so that, in the Fourier plane, the input ultrafast pulse is converted to pulse trains containing N TFO copies at the same transverse position without any spatial-temporally coupled phase from diffraction.

Due to the spread in the direction of wave vectors, each replica will have a different wave vector $\vec{k_j}$ at focus. Then the dot product of $\vec{k_j}$ and $\vec{z}$ in Eq. (8.2) will be written as $k_j z \cos\theta_j$, where θ_j is the angle between two vectors. However, since the maximal θ_j in our case is only 0.01 rad, $k_j z \cos\theta_j$ can be approximated as kz so that we can still use Eq. (8.3) to represent the field generated by TFO gate.

N depends on the number of DMD columns illuminated by the incident pulse, which is 608 in the current system. The intensity of each replica can be arbitrarily tuned by enabling only a subset of the mirrors in each DMD column, which further enables arbitrary control over the pulse train. $\Delta\tau$ is determined by the physical size and tilt angle of the micromirrors. For the current device, $\alpha = 0.21$ rad is the tilt angle of each micromirror while $d = 10.8$ μm is the separation between two micromirrors. The theoretical value of $\Delta\tau$ between two TFO copies is given by: $\Delta\tau = \sin(2\alpha)d/c = 14.66$ fs, where c is the speed of light in air.

To experimentally measure the temporal interval $\Delta\tau$, we first prepare a pulse train which is the same as what show in the middle figure of Figure 8.4(c). Each effective TFO replica consists of 5 DMD columns, which means 5 columns are set to 'on' state. There are 15 DMD columns are set to 'on' state between two effective replicas, and each DMD column corresponds to one temporal interval $\Delta\tau$. Therefore, the separation between the peaks of two adjacent effective TFO replicas is 20 DMD columns, which is $20\Delta\tau$ in the time domain. Since there are 30 effective replicas at the 'on' state, the separation between the first effective replica to the last effective replica is 580 DMD columns, which is $580\Delta\tau$. We then calculate the temporal separation ΔT by measuring the position of the first effective replica and the last effective replica in 9 measurements. The temporal interval can be found as: $\Delta\tau = \Delta T/580 = 16.00$ fs with a standard deviation of 0.01 fs. Note that 0.01 fs is the average uncertainty of each micromirror, and the uncertainty of the entire pulse train is 6.08 fs, which corresponds to an uncertainty of 1.82 μm in spatial separation between the first and last effective replica. The 1.82 μm spatial uncertainty is a reasonable number according to the performance of our translation stage. Therefore, we believe that the temporal resolution induced by each micromirror is 16.00 ± 0.01 fs, which is consistent with the theoretical value..

A larger $\Delta\tau$ and a longer pulse duration of each TFO replica can be achieved by combining multiple DMD columns into a single "effective column" due to the interference between adjacent TFO replicas. As what we show in Figure 8.4(c), when each effective TFO replica consists of 5 DMD columns, each replica will have a pulse duration of 80 fs. Due to the long pulse duration of the NIR pulse, the separation between two effective replicas is 240 fs (15 DMD columns) to explicitly show the structure of pulse trains. The red dashed trace indicates that the TFO copies at those temporal position are turned off by modulating the TFO gate. All cross-correlation traces of pulse trains are averaged over 9 measurements. The total time window T (the temporal field-of-view) depends on the overall size of the mirror array, and is equal to $N \times \Delta\tau$, which is 9.73 ps. It is noteworthy that, by selecting a DMD chip with the appropriate specifications, different $\Delta\tau$, N and T can be achieved as well.

The encoding speed is mainly limited by the switching speed of the DMD, which can be as large as 4 kHz in our system and can be further increased to 20 kHz by using a faster DMD chip [151]. One of the beauties of TSPI is that the temporal sampling size comes from the modulation on TFO but not from detectors. Therefore, our scheme solely requires detectors with bandwidth exceeding the modulation frequency of the DMD, allowing the use of kHz-level photodiodes. As a comparison, previous temporal imaging schemes, including the use of time lenses and temporal ghost imaging, cannot hardly provide such an accurate sampling even with the use of fast detectors with bandwidths approaching 100 GHz [168, 169, 170, 175, 176, 177, 178, 179, 180, 181, 182, 184, 185, 186, 187, 188]. Thanks to encoding the probe beam as opposed to temporally modulating the THz pulses [7], our simple and reliable scheme can directly utilize commercially available DMDs with a high modulation speed and damage threshold, and hence no additional fabrication of devices, for example time lenses, is required.

8.4 Experimental results

Compared to the minimal $\Delta\tau$ of the pulse train, our laser pulse has a relatively long pulse duration of 80 fs. Therefore, adjacent replicas will be highly overlapped in time. Due to the fact that TFO replicas are mutually coherent, this overlap will lead to multi-pulse interference and the adjacent copies will coherently add up to form a new pulse, which will be shown numerically in the later section. Thus, to get a precise measurement, we combine every 4 DMD columns together as effective columns to prepare pulse trains with a $\Delta\tau = 64$ fs. For the same reason, to avoid the multi-pulse interference between adjacent TFO replicas, we represent each row of Walsh-ordered HM as the sum of four sub-rows. Letting the Nth row be defined as $\{a_i\}$, we set the sub-rows as { $b_i = a_i$, for i= 0,1,2,3 mod 4 }. For example, the 2nd row of H_8 is:

$$H_{8,2} = \begin{Bmatrix} 1 & 0 & 1 & 0 & 1 & 0 & 1 & 0 \end{Bmatrix}. \tag{8.5}$$

We break it into a 4 by 8 matrix consisting of 4 sub-rows:

$$H_{8,2} = \begin{Bmatrix} 1 & 0 & 0 & 0 & 1 & 0 & 0 & 0 \\ 0 & 0 & 0 & 0 & 0 & 0 & 0 & 0 \\ 0 & 0 & 1 & 0 & 0 & 0 & 1 & 0 \\ 0 & 0 & 0 & 0 & 0 & 0 & 0 & 0 \end{Bmatrix}. \tag{8.6}$$

This procedure will quadruple the acquisition time but provide a precise pulse train with less interference between adjacent TFO replicas, and hence a more accurate measurement. One can skip this procedure when a short pulse duration laser is used. As a comparison, if a pulse with a longer pulse duration is used, one has to break each row of Hadamard matrix into more sub-rows, which will lead to an increased data acquisition time. It is noteworthy that the original HM consists of both 1 and -1 elements. However, since our DMD can only encode non-negative values, we only use positive HM in our temporal encoding: $H_{+1} = (H + 1)/2$.

Figure 8.5 shows the THz pulses reconstructed based on TSPI and procedure mentioned above. Limited by the pulse duration of the original pulse (80 fs), we choose $\Delta\tau$ to be 64 fs by combining 4 DMD columns into 1 effective column. 128 TFO replicas, encoded by the 128-dimensional Walsh-ordered Hadamard matrix, constitute our probing pulse train with $T = 8.19$ ps. The red curves are THz fields and spectra measured by raster scanning a mechanical delay stage without averaging. As illustrated in Figure 8.5(d), by sacrificing high frequency components, a recovered THz pulse with high fidelity (84.30%) can be achieved even at 20% CR. At this CR, the last sampling pulse train is encoded by the 25th row of the Walsh-ordered Hadamard matrix, which results in the cutoff sampling frequency at 1.5 THz and a weak sidelobe at 2.4 THz. For a CR of 30%, additional high-frequency terms are measured and in the spectrum, almost all high-frequency terms in THz pulse are collected, leading to a near-unity fidelity of 97.43% in THz field. As the CR goes higher to 40%, more high-frequency components are collected but the improvement is limited (fidelity of 97.76% in field). When we look at the spectrum, two spectra match well for all frequencies except for some noises, which indicates that we have included enough high frequencies in the measurement. Therefore, all higher-frequency terms can be ignored due to

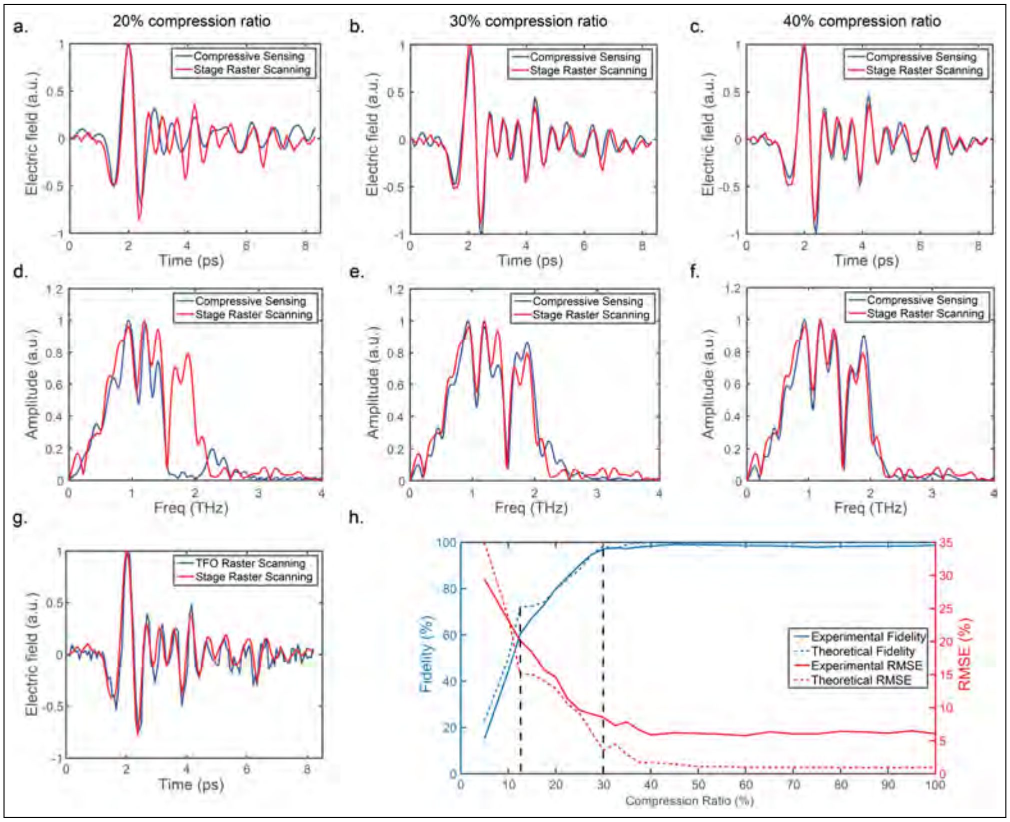

Figure 8.5: Recovered THz electric fields and spectra at different CRs (blue curves). (a) and (d): Recovered THz field and spectrum at 20% CR. The fidelity in THz field is 84.30% and the root mean square error (RMSE) is 14.92%. (b) and (e): Recovered THz field and spectrum at 30% CR. The fidelity in THz field is 97.43% and the RMSE is 7.69%. (c) and (f): Recovered THz field and spectrum at 40% CR. The fidelity in THz field is 97.76% and the RMSE is 7.17%. (g): Raster scanning using TFO. The sampling rate and acquisition time of each measurement are set to be the same as CS data. Fidelity is 87.35% and RMSE is 13.11%. (h): The measured and theoretical fidelities and RMSEs as functions of CR. The RMSE is mainly limited by the measurement noise.

their relatively small contributions. Note that due to the limited detection bandwidth of ZnTe crystal, we only show the spectra in 0-4 THz range.

Comparing to the data acquisition time of the mechanical stage raster scanning data (sampling rate at 2 Hz which is mainly limited by the stability of our mechanical stage, leading to a measurement time of ~64 s), our TSPI system requires only ~15 s with 30% CR (sampling rate at 10 Hz), and can be further reduced below 1 s by upgrading the experimental hardware (will be discussed later). Hence, TSPI can reduce data acquisition time, data storage and transfer memory requirements by a factor of at least 2/3, which would significantly enhance system efficiency in this era of big data. It is also worth noting that the data processing time is ~ 1 s for a 30% CR result, which will become longer when the CR is higher (the upper limit is less than 2 s). A shorter processing time should be available when the algorithm and MATLAB code are further optimized. Apart from a more efficient measurement, CS is also more robust to noise than raster-scanning. As shown in Figure 8.5(g), under the same sampling rate and integration time of each measurement, the fidelity of the TFO raster scanning data, i.e. sequentially turning on each DMD column, is only 87.35% and the RMSE is 13.11%, which are worse than the CS data even when the CR is only 30%.

These experimental results shown in Figure 8.5(h) are in good agreement with our theoretical predictions and Figure 8.3. As the CR increases, both fidelity and RMSE change dramatically at first, and then gradually level out after the CR reaches 30%. Our theoretical model also predicts that there are two discontinuity points in the slope of both RMSE and fidelity curves. As indicated by the two vertical dashed lines, the first turning point is located at CR equal to 12.5% while the second one is at CR equal to 30%. The slopes in both RMSE and fidelity curves abruptly decrease to a slower rate and can even change sign after the turning points. Similar observations have been found in spatial single-pixel imaging work when the sampling matrix is reordered [189]. Therefore, in both spatial and temporal CS, one can optimize the acquired information within a given CR by rearranging the sampling order, which demonstrates the spatio-temporal duality of light pulses. An improved measurement efficiency can be predicted by further optimizing the sampling strategy based on these turning points.

Similar to its spatial counterpart, TSPI is resistant to temporal distortions. To demonstrate this robustness, we first intentionally make the illumination on the DMD asymmetric, which is shown in Figure 8.6(a). This results in a different intensity for each TFO replica, and further leads to asymmetric pulse trains in the time domain (Figure 8.6(c)). The ratio between the maximal and minimal intensities in (c) is about 10. As a comparison, this ratio is about 3 in Figure 8.4(c) while the SNR is the same (∼350). Despite the distorted TFO replicas, the recovered THz signal, shown in Figure 8.6(d) and (e), has a fidelity of 96.96% in the field at 40% CR. The major information loss comes from underestimation of oscillations at the tail of the THz pulse (above 5 ps), which results from the weak intensities of TFO replicas at the end of the pulse train. Next, as illustrated by the blue arrow in Figure 8.6(b), we move the location of the Fourier plane of DMD 25 mm away from the ZnTe crystal by moving the TFO gate 25 mm away from the de-

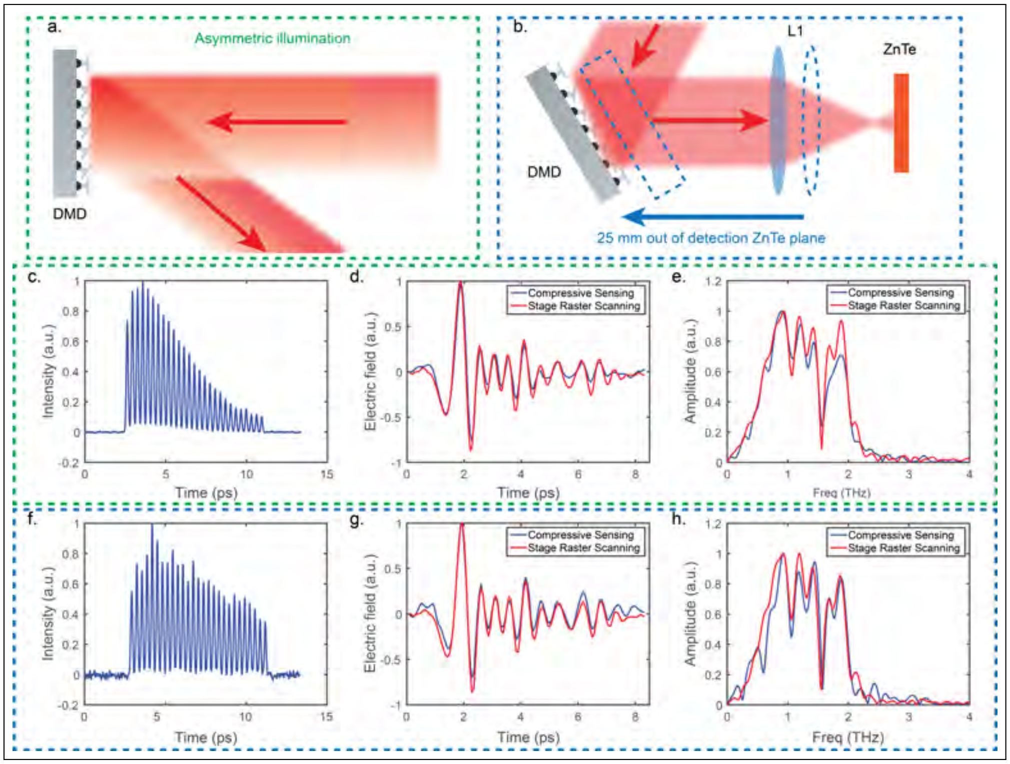

Figure 8.6: Recovered THz electric fields and spectra using distorted TFO gate at 40% CR. Red arrows illustrate the propagation direction of NIR pulses. (a): How we distort TFO gate with an asymmetric illumination. (b): How we move the Fourier plane of DMD 25 mm away from the detection ZnTe plane by moving TFO gate in the direction as the blue arrow shows. (c): The measured asymmetric pulse train formed by the distorted TFO copies. (d) and (e): The corresponding recovered THz field and spectrum. The RMSE in field is 7.21%. (f): The measured pulse train when the detection ZnTe crystal is 25 mm out of the Fourier plane of DMD. (g) and (h): Recovered THz pulse and spectrum using the distorted pulse train in (f). The RMSE in field is 7.66%. (c) and (f) are averaged results of 9 measurements while THz pulses recovered by CS and raster scanning have no averaging.

tection crystal. Due to the spread of k-vectors of each replica at the Fourier plane, the TFO copies will be spatio-temporally separated at the detection crystal plane. This leads to the spatio-temporal coupled sampling, which yields an irregular pulse train envelope and lowers the intensity of each sub-pulse shown in Figure 8.6(f) (SNR is only ∼80). Nevertheless, as shown in Figure 8.6(g) and (h), distorted pulse trains do not affect the quality of the recovered signal, which has a fidelity of 98.34% in field at 40% CR. Such a robustness can also be interpreted by the spatio-temporal duality of light pulses. In single-pixel imaging, the spatial correlation between the intensity distribution and position lies at the heart of the successful recovery of images. A distortion in the intensity profile of the illumination distribution will lead to the over- or under-estimation of the object intensity, but the accuracy of signal recovery will not decay significantly if CS is used. Similarly, as long as the correlation between temporal position of each TFO replica and intensity envelope of the entire pulse train is not destroyed, the THz pulse recovered by TSPI will be robust against temporal distortions, which will be numerically demonstrated later.

To demonstrate that TSPI can work for signals in a broad range of frequencies, we recover two NIR pulses with ∼90 fs and ∼125 fs pulse durations. To perform the measurement, the detection crystal is changed to a 1-mm-thick BBO crystal. A PMT is used as the new detector to replace the balanced photodiodes in THz measurements. Due to the long pulse duration of our laser (80 fs), preparing high-contrast sampling pulse trains with 16 fs temporal modulation size is not feasible. Therefore, we have to implement a rolling-average strategy to measure NIR pulses with 16 fs sampling size. In

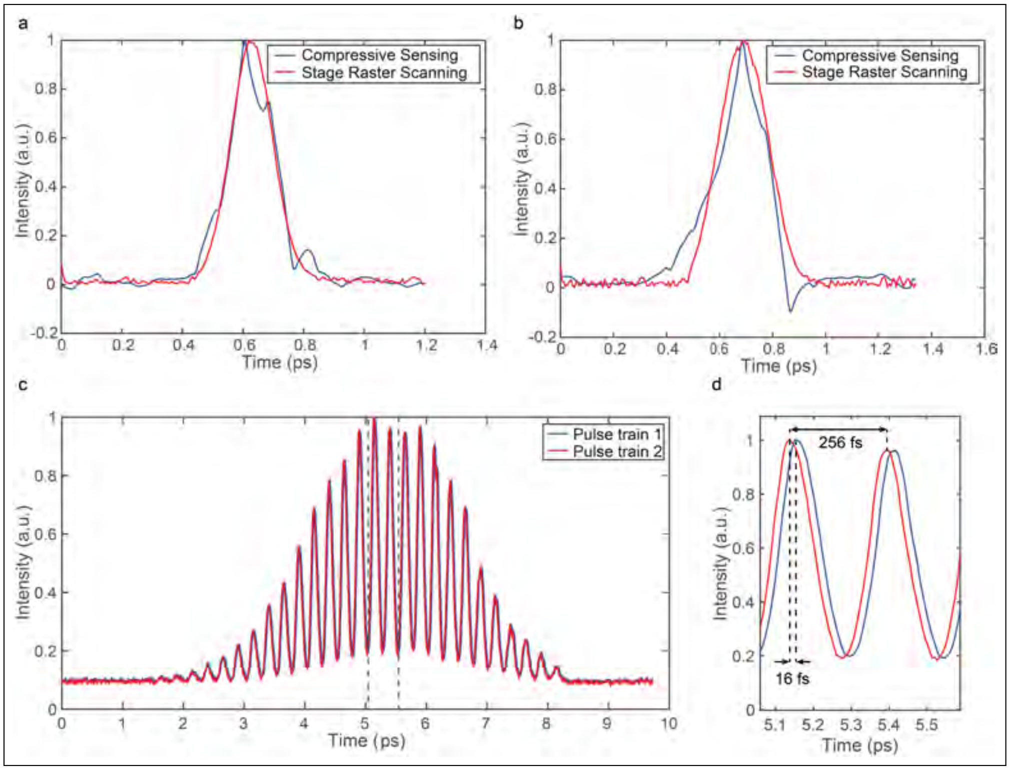

Figure 8.7: Recovered NIR pulses (blue curves) and the measured results using raster scanning (red curves). (a): Recovered NIR pulse with 90 fs pulse duration at 80% CR. (b): Recovered NIR pulse with 125 fs pulse duration at 80% CR. (c): Two pulse trains used for NIR measurement. By shifting 1 DMD column, we shift pulse train 1 16 fs forward to get pulse train 2. (d): The details of the measured pulse trains shown in the black dashed box in (c). One can find that the displacement between two pulse trains is 16 fs while the separation between two peaks in one pulse train is 256 fs.

order to do this, we first combine 5 DMD columns together (80.00 fs) as an effective column. Then we perform the measurement of the unknown pulse in one time window. Next, we shift this time window 16.00 fs forward to make another set of measurement, which corresponds to the shift of 1 DMD column. We continue this rolling process until 5 shifts are done. The final recovered NIR pulse is the rolling average of the measurements of all 5 shifts.

The experimental results are shown in Figure 8.7. We change the pulse duration in the signal arm by pre-chirping the laser pulse using the self-phase modulation effect inside a ZnTe crystal. In the meantime, the pulse duration of the probe arm is kept at 80 fs. Figure 8.7(a) is the compressive measurement result (blue curve) of a 90 fs pulse comparing to the delay stage result (red curve). The recovered signal has a fidelity of 98.48% in pulse shape while the pulse duration is 91.4 fs. Figure 8.7(b) shows the compressive result of a 125 fs pulse. The fidelity is 97.88% while the pulse duration is 110.0 fs. Both CS results are measured at 80% CR due to the fact that NIR pulses carries more high-frequency components. The main limiting factor in NIR pulse measurement is the instability induced by self-phase modulation. The instability not only leads to a worse SNR (less than 70 in delay stage data), but also results in a irregular but large intensity fluctuations at peak. When these significant sources of noise are included in CS recovery, we will have a distorted pulse. For example, we have observed a negative sidelobe at 0.85 ps in Figure 8.7(b), which has no physical meaning because the measured quantity is pulse intensity. We expect that this noise should vanish if one uses linear optics devices to introduce chirp. Therefore, a better recovery should be available for real NIR pulses whose pulse duration are not extended by nonlinear effects. To get a more accurate CS recovery, one can also intentionally stretch the NIR pulses, for example using time lenses, to a longer level and then use our TSPI to measure it [168, 169, 170, 184, 185, 186, 187, 188]. It is notable that the TSPI system can be used for other wavelengths as well. One simply needs to replace the crystal and detector with the ones at the correct frequency band.

8.5 Numerical simulation

To numerically verify our experimental results, a Matlab code is developed based on the theoretical model in section 8.2. We first simulate the results shown in Figure 8.5. As shown in Figure 8.8, our experimental data precisely matches our simulation results. When the CR is 20%, both experimental and simulation data show the lack of high frequency components above 1.5 THz. Meanwhile, as what we discuss before, the weak side lobe at 2.4 THz, which corresponds to the sampling frequency of the 25 th row of the Walsh-ordered HM, is also verified by simulation. When the CR goes to 30%, the main part of the spectrum has been accurately recovered except for the weak side lobe, which is also observed in our experimental data. When the CR goes to 40%, the side lobe disappears and the spectrum of the CS recovered pulse is almost identical to original spectrum. Therefore, these simulation results indicate that our experimental data has a high agreement with the theoretical model.

We then focus on the role of pulse duration of the input pulse in TFO, which has a critical impact to TFO outputs. Basically, all TFO replicas are coherent unless the input pulse is spatially incoherent. Therefore, due to the long pulse duration, the interference between adjacent two or more

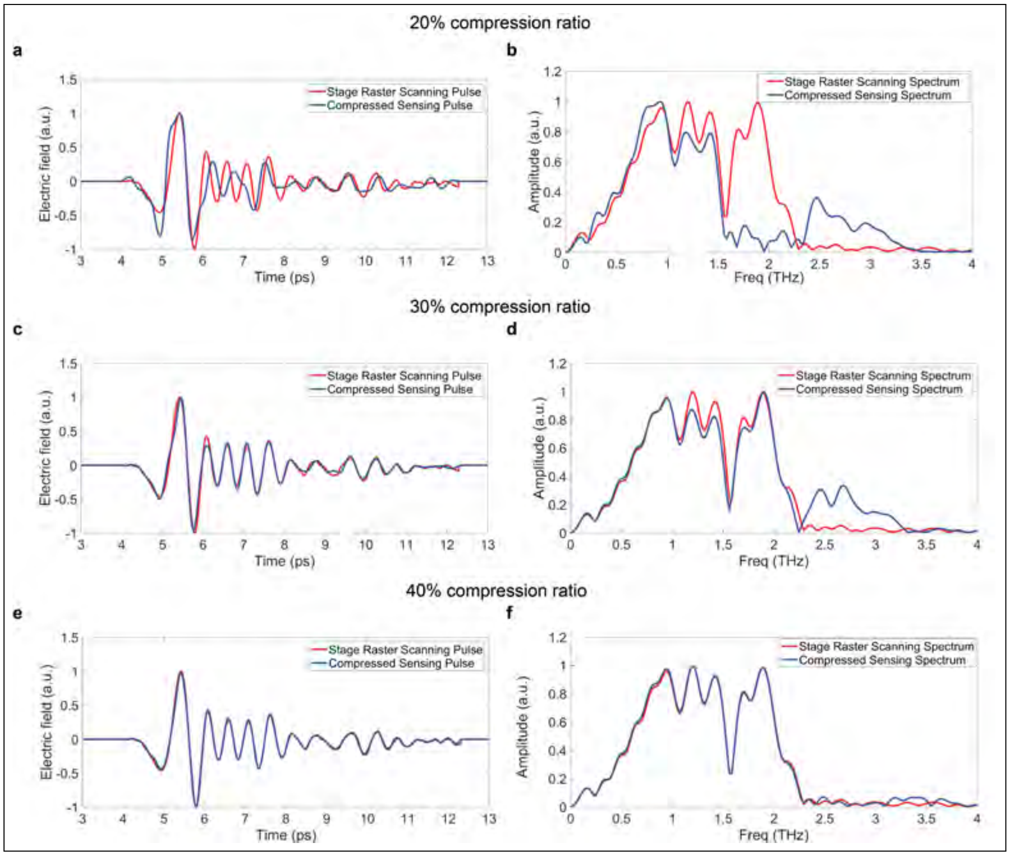

Figure 8.8: (a)-(c): Recovered THz pulses at different CRs: 20%, 30% and 40% respectively. (d)-(f): Corresponding spectra at different CRs: 20%, 30% and 40% respectively.

sub-pulses will result in temporal structures under control. For example, in Figure 8.9(a), when the input pulse has a duration of 80 fs and all columns are on, we can get a 9.73 ps long pulse in the time domain. As shown in Figure 8.9(a)-(c), even when we separate two effective TFO copies, each one is the coherence interference of 4 TFO copies, with 192 fs, one still cannot get a unit contrast of pulse trains when the pulse duration is longer than 60 fs. If we further reduce the separation to 64 fs, we can only get pulse trains with unit contrast when the input pulse duration is around 16 fs. When no separation is added between two effective TFO copies, a 8.19 ps long top-hat pulse is generated in the time domain even the input pulse duration is 40 fs. Pulse trains with a unit contrast are only available with input pulse duration is equal to 10 fs if there is no additional separation between adjacent replicas.

Then we turn to figure out the impact of pulse duration on recovered THz signals. We find that pulse duration, which leads to imperfections in pulse trains, only significantly affect the quality of pulses recovered by Walsh-ordered HM directly. Pulses recovered by CS, even both methods use the same encoding method, have similar fidelity and RMSE (difference less than 0.5%) under different pulse durations. As shown in Figure 8.10(a)-(c), when input pulse duration is long and pulse trains have poor contrasts, THz signals recovered by Walsh-ordered HM have both over-estimations and under-estimations compared to original signals. This effect will gets weaker when the pulse duration becomes short and the contrast of pulse trains gets close to unit. However, when pulse duration becomes ultra-short, for example 16 fs, one would expect the pixelization effect in the recovered THz signal as shown in Figure 8.10(g) and (h). As a comparison, THz signals recovered by CS, shown in Figure 8.10(d)-(f) and (i), are much less affected by pulse duration and the quality of pulse trains, which demonstrates the robustness of our TSPI. Therefore, our TSPI is more robust against temporal fluctuations of the input pulse of TFO gate.

Next, we will demonstrate that our TSPI is theoretically robust against

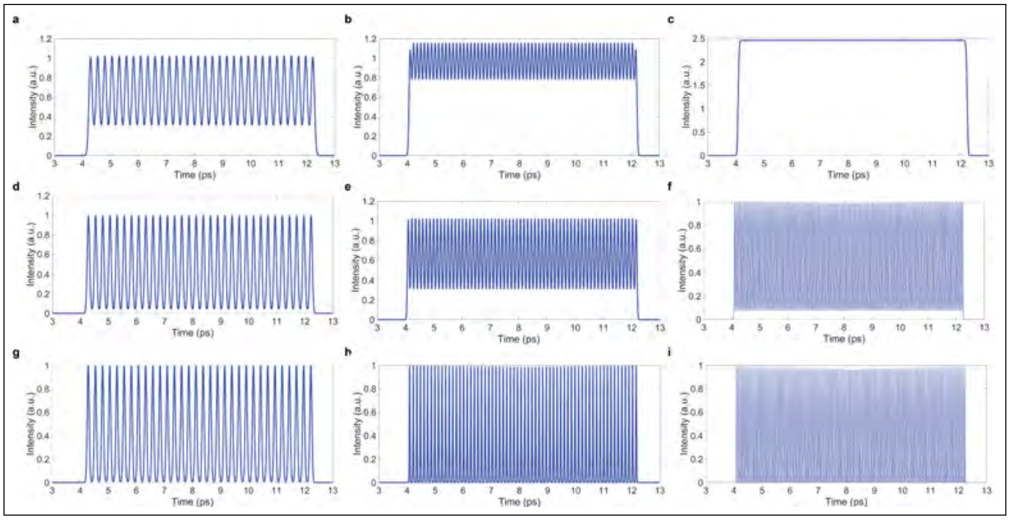

Figure 8.9: (a)-(c): Pulse trains at the output of the TFO for different input pulse durations: 100 fs, 80 fs and 60 fs respectively. The temporal separation between two effective columns is equal to 192 fs. The contrast in (a) is 53.59% while it becomes 91.97% in (b), which matches our experimental observation. (d)-(f): Pulse trains with different input pulse duration: 60 fs, 40 fs and 16 fs respectively. The temporal separation between two effective columns is equal to 64 fs. The contrast in (d) is 19.43% which is too poor to use. The contrast becomes 53.52% in (e) which is good enough for both TSPI and Walsh-ordered HM recovery. Pulse trains at the output of the TFO for different input pulse durations: 40 fs, 16 fs and 10 fs respectively. The temporal separation between two effective columns is equal to 16 fs. As shown in (g), due to the long pulse duration comparing to the temporal separation, we can only get a top-hat pulse in the time domain when the pulse duration is 40 fs. As a comparison, when the pulse duration reduced to 16 fs, the contrast in (h) is 86.06%. When the pulse duration reduced to 10 fs, we can get 100% contrast as shown in (i).

imperfections in TFO gate. We first prepare a simple distortion by making the envelop of pulse trains asymmetric. The ratio between the maximum and minimum in Figure 8.11(a) is about 10, which is the same as the pulse train shown in Figure 8.6(c). As one can see in Figure 8.11(b), asymmet-

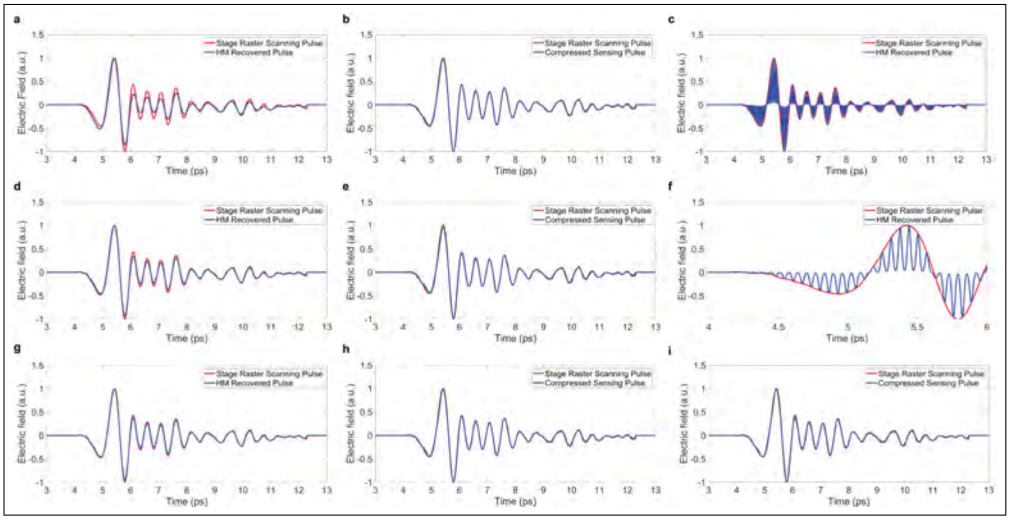

Figure 8.10: (a)-(c): Recovered THz pulses using Walsh-ordered HM directly. The encoding process is the same as what we do in the experiment, i.e. each row of Walsh-ordered HM is represented by the sum of 4 sub-rows, which results in the corresponding pulse trains shown in Figure 8.9(a)-(c) respectively. (d)-(f): Recovered THz pulses using CS and pulse trains in Fig. S4(a)-(c) respectively. CR is 40% for all three recoveries. (g): Recovery using Walsh-ordered HM directly. The pulse duration is 16 fs. (h): The zoom-in figure of 4-6 ps in (g). (i): CS recovery with a pulse duration of 16 fs.

ric pulse trains lead to the over-estimation at the tail of THz pulse and the under-estimation at the beginning of THz pulse when we use Walsh-ordered HM recovery directly. However, the defects from the distorted TFO gate do not affect the performance of TSPI (Figure 8.11(c)). Then we make the distortion more complicated by moving the Fourier plane of DMD 25 mm away from the detection crystal. Due to the spread of k-vectors of different TFO replicas, each copy will intersect with different transverse position of the THz pulse. Considering the Gaussian distribution of the THz pulse and the asymmetric structure of pulse trains, the measured envelop of pulse trains at the detection crystal plane have an irregular envelop as shown in Figure 8.11(d). The abnormal envelop of pulse trains leads to the over- and under-estimation of THz pulses. Nevertheless, our THz pulse recovered by CS is still robust to this more complicated distortion. The experimental verification and explanation of these two distortions have been shown in Figure 8.6. In fact, the envelop of pulse trains plays a much less important role in CS recovery than Walsh-ordered HM or random recovery. One can even use a highly distorted TFO gate generating random intensity envelope of pulse trains to recover THz signals using our TSPI approach. The results are shown in Figure 8.11(g)-(i). One can figure out that the random intensity envelope of pulse trains leads to a THz pulse with randomly distributed under- and over-estimations when Walsh-ordered HM recovery is used. However, in Figure 8.11(i), the THz signal recovered by CS only gets slightly affected. Therefore, based on both experimental verification and theoretical analysis, we can claim that, as long as the correlation between temporal position of each TFO replica and intensity envelope of the entire pulse train is not destroyed, the recovered THz pulse will be robust against distortions on TFO gate.

8.6 Machine learning enhanced THz TDS

Lastly, we demonstrate a compressive ultrafast THz TDS system as one potential application of TSPI, and show that we can improve its performance

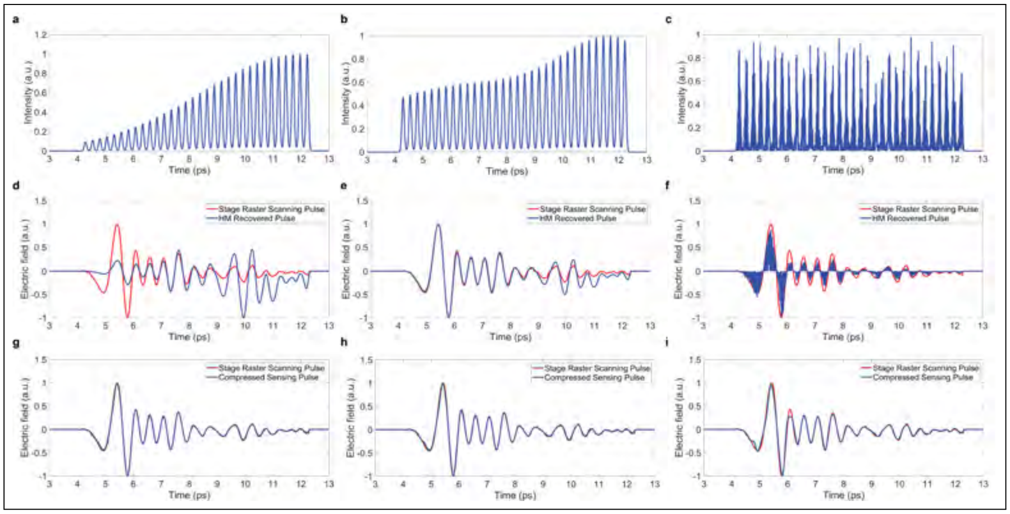

Figure 8.11: (a)-(c): Recovered THz pulses using asymmetric pulse trains generated by the temporally distorted TFO gate. (d)-(f): Recovered THz pulses using asymmetric pulse trains located 25mm out of the detection crystal plane. (g)-(i): Recovery based on a random envelop of pulse trains. The CR is 40% for all CS recoveries.

through use of machine learning (ML). A simple 12-layer convolutional neural network (CNN) is developed to classify the compressive signals of different samples under poor SNR, and the architecture is shown in Figure 8.12. The input signal layer (1×128) is connected to the first convolution layer with 16 1×4 filters. Then a batch normalization layer and a ReLu layer are implemented sequentially, which normalizes the activations and is the nonlinear activation function respectively. After the first stage, a max pooling layer with a 1×2 pooling size is used to localize the features. Then the second stage starts with another convolution layer consisting of 8 1×4 filters. Similar to the first stage, a batch normalization and a ReLu layer are used. After this, we enter the classification stage with two fully connected layers (8 neurons and 3 neurons respectively). At last, a softmax layer, which normalizes the output from the fully connected layer, and a classification layer are adopted.

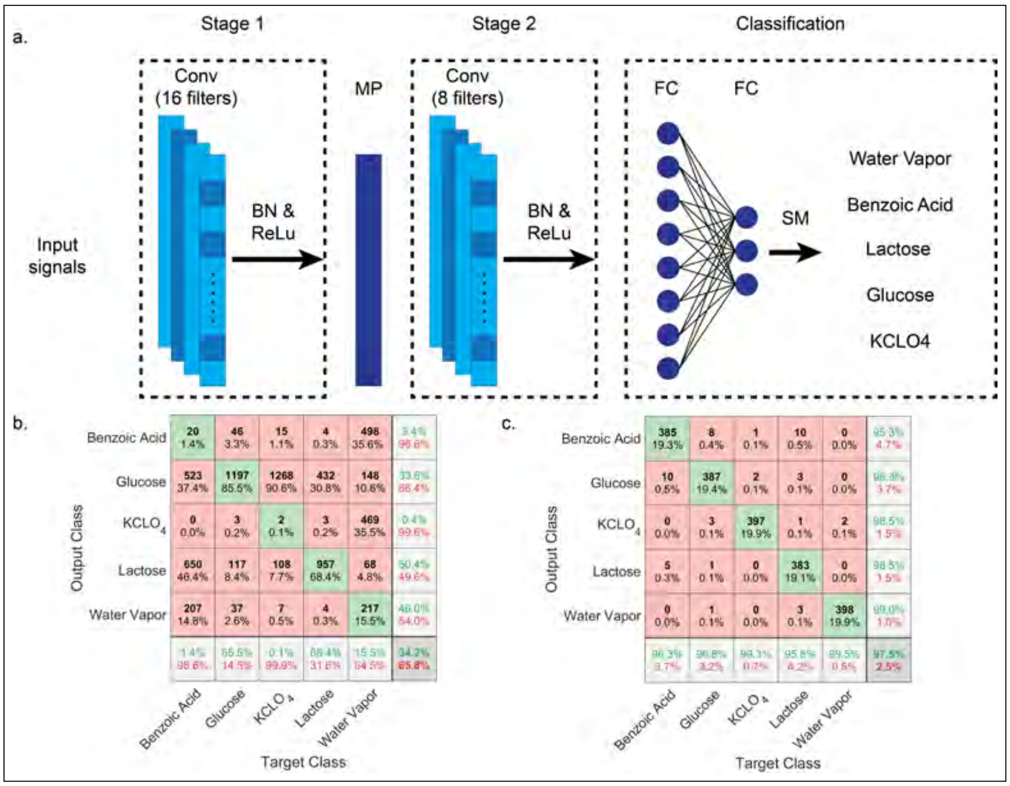

Figure 8.12: (a): Architecture of our CNN. Conv stands for convolution layer while BN and ReLu stand for batch normalization layer and rectified linear unity layer respectively. MP is the maxpooling layer and FC is the fully connected layers. SM is the softmax layer. (b): Confusion matrix before training. Due to the poor SNR, the classification accuracy is only 34.2%. The green numbers are accuracy of each sample while the red numbers are failure probabilities. The CR is 40%. (c): Confusion matrix after training. The CR is 40%.

Five samples (water vapor, glucose, lactose, benzoic acid and $KCLO_4$) are used to train this CNN. Each sample has 1000 sets of data from our ultrafast THz TDS system so that in total 5000 sets of data are used for training.

To show the noise resistance of the ML-enhanced TDS system, the SNR of the THz pulse is decreased to ∼10 by attenuating the THz pulse to sub-fJ level and lowering the integration time on the lock-in amplifier. Each set of data is measured under a sample rate of 20 Hz or 50 Hz with an integration time (time constant) of 3 ms, which corresponds to acquisition times for each DMD pattern of 50 ms and 20 ms respectively. However, due to the limited data readout time between lock-in amplifier and computer (∼15 ms), there are only 3 data points inside each acquisition time of 50 ms. For the same reason, only 1 data point for the acquisition time equal to 20 ms. Therefore, the effective measurement time of each DMD pattern in ML is 9 ms (for 50 ms acquisition time) and 3 ms (for 20 ms acquisition time). Since our THz pulse is attenuated to 3 times weaker, the final SNR of these data sets is about 10 (for 20 Hz sampling rate) or 17 (for 50 Hz sampling rate) times weaker than the data shown in Figure 8.5 and Figure 8.6. Due to the poor SNR, the accuracy of the successful classification without training is less than 35%. For example, 34.20% in the confusion matrix shown in Figure 8.12(b).

The training process shuffles these sets of data at the beginning of every epoch and 6 epochs are used. In order to provide a more stable network, a batch size of 150 sets of data is used, which further leads to the maximal number of iterations at 60. The entire training process takes about 400 s with a constant training rate of 0.01. We then use 2000 sets of data (400 sets of each sample) to validate the performance of our CNN, and the successful classification probability is about 97.5% at 40% CR as shown in

Figure 8.12(c).

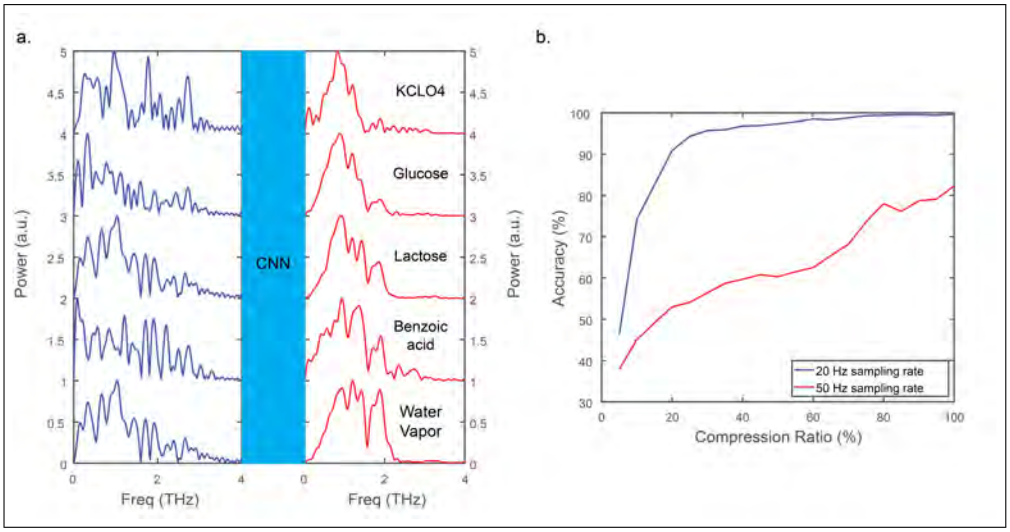

Figure 8.13: Results of CNN-enhanced THz spectroscopy. (a): The sample classification is based on a CNN. Red curves are clean spectra that we have after training while blue curves are noisy data before training. Due to the poor SNR, the fingerprints of each sample are lost and cannot be identified from spectra. (b): Accuracy as functions of CR. All the identification accuracies are averaged over 5 trainings.

To intuitively show results of CNN, we plot the measured spectra before training and the clean spectra after training, which are shown in Figure 8.13(a). Without the help of ML, the measured THz spectra are noisy which leads to a poor classification accuracy at 34.20%. As a comparison, after training our CNN with 5000 sets of data, we can successfully classify the remaining 2000 sets of data (400 for each sample) with an accuracy of 97.50% at 40% CR, and the clean spectra are shown as the red curves. If one further reduces the SNR by increasing the sampling rate from 20 Hz to 50 Hz, the identification accuracy will significantly decrease as shown in

Figure 8.13(b). When the sampling rate is 20 Hz, the accuracy rises up quickly when the CR increases from 5% to 20%, and then starts to converge, which has a very similar behavior as the fidelity shown in Figure 8.5. As a comparison, when sampling rate is 50 Hz, the SNR in each measurement becomes 1.73 times smaller than the 20 Hz sampling rate case, and accuracy curve does not start converging even when CR is 100%. Therefore, if training data sets are measured using other approaches with worse robustness against noise, for instance raster scanning, a high identification accuracy will not be achieved even with the help of ML.

8.7 Discussion and conclusion

The conventional approach for ultrafast sensing is raster scanning the time delay between a short probe pulse and the signal pulse. As a contrast, our method can significantly reduce the data acquisition time in the sampling process, and provide a better fidelity as well as an enhanced robustness against noise (the comparison in Figure 8.5(g)).

Compared to methods using cameras or spectrometers, our approach is applicable to both weak and strong pulses at various frequency bands. Even though cameras and spectrometers enable the possibility of single-shot measurements, effective measurement of weak pulses is not applicable at some wavebands. For example, in THz region, these single-shot measurement methods usually require the use of μJ-to-mJ-level pump pulse to generate nJ-to-pJ-level THz pulses [130, 190, 191, 192, 193, 194, 195]. As a comparison, our approach only needs nJ-level pump pulses, and is capable of measuring fJ-level THz pulses. Hence, the sensitivity of our system is about 3 orders of magnitude better than the camera- or spectrometer-based methods. Furthermore, when pulses become weak, these single-shot measurement methods will need to average over multiple shots to provide a good SNR, which is no longer a single-shot measurement and will result in a slow measurement speed as well. However, for NIR and optical pulse measurements, our method does not resolve spectral phase at the moment and minimal resolvable pulse duration cannot be below 10 fs, which is a drawback compared to FROG or SPIDER [165, 167].

Temporal imaging based on time lenses is another way to measure ultrafast signals. By stretching the pulse to a longer level, one can use fast photodiodes to measure the optical pulses [168, 169, 170, 184, 185, 186, 187, 188]. Even though the ultrafast measurement done by time lenses can be much faster than our computational-based TSPI, our technique is still advantageous in the working frequency bands and flexibility. The working frequency bands of time lenses is usually at optical and NIR regions, and time lenses in the THz band have not been demonstrated yet. Meanwhile, even in the optical and NIR wavebands, the design and fabrication of time lenses have to be changed for each wavelength, which usually lacks flexibility compared to our TSPI.

One limitation is the sampling speed of the system. Even though our system is faster than a delay stage, we does not fully utilize the advantage of DMD in sampling speed, and there are two limiting factors stop us from fast measurements at kHz level, which is the potential speed limit of the system. The first limiting factor is the poor SNR of our THz pulse. The signal becomes noisy when the integration time (time constant) on lock-in amplifier is below 10 ms and hence the recovered pulse has a poor quality. The second limiting factor is the communication speed between lock-in amplifier and our data acquisition program. The data read-out time from lock-in amplifier to our computer program is about 15 ms. Therefore, the maximal sampling rate with this lock-in amplifier is about 66.67 Hz, which is far below the speed limit of DMD. Hence, to improve the measurement speed to kHz level, not only a stronger THz pulse is required, a faster digital signal processing card with synchronization is also necessary. Luckily, both requirements are not hard to accomplish if the hardware are upgraded. For example, researchers have demonstrated the possibility of using a commercially available fiber-based THz system to generate high SNR THz signals, and perform fast measurement over 2 kHz with a fast data acquisition card [151]. Even though due to the long response time of silicon, the speed of their scheme cannot go beyond 4 kHz, our methods, including our previous spatial CS approach, have no such limitation [7]. Therefore, we believe that, after upgrading the hardware, kHz-level sampling rate is applicable to our approach, and it is even possible to reach the speed limit of DMD at 20 kHz.

Another limitation is the temporal field of view. As what we discuss before, the temporal field of view is limited to 28 ps. However, this limitation comes from the commerically available DMDs. One can further fabricate a customized DMD, or similar devices as long as it can introduce a spatial-temporal chirp, with a larger field of view, or cascade multiple DMDs to introduce more chirps to achieve a better field of view. Therefore, this limitation should not be an obstacle if additional fabrication is available.

Chapter 9

Conclusion and future work of computational THz sensing

In the second half of this dissertation, I try to develop a new approach to spatio-temporally characterize THz pulses. Both the spatial and temporal sampling systems are inspired by SPI technique, and follow the same train of thought: encoding the probe beam with commercially available optical SLMs to enhance the performance.

In the spatial sampling, we propose, for the first time, the concept of probe-beam encoding in THz SPI. By using an optical SLM in the probe arm of a conventional THz TDS system, we can successfully encode sampling patterns onto the probe beam, and then recover the image of THz field using a single-pixel detector via compressive sensing. As what we demonstrated, subwavelength imaging is available if the object is close to the detection crystal, and high fidelity images (more than 90%) can be recovered with a 50% CR. This new approach can release the requirement of THz SLM, multiple lasers and photoexcited free-carriers. In the meantime, there is no limitation to the pump pulse so that strong THz pulses are also available in our approach. Therefore, we believe that this method can provide sensitive and efficient measurement of THz pulses in flaw detection, security check and hyperspectral imaging.

In the temporal sensing, we develop and propose, for the first time, the concept of TSPI based on the development of an ultrafast TFO gate. Ultrafast signals at different frequency bands can be compressively measured using exclusively kHz-rate slow detectors without any scanning. The 16.00$\pm$0.01 fs temporal sampling size enables the successful measurement of a 5 fJ THz pulse and two NIR pulses with high fidelity. The robustness of TSPI against temporal distortion is also demonstrated. Lastly, we show that our technique can be used to perform ultrafast THz TDS with the help of ML. Our TSPI system can cover a frequency band including both NIR and THz region with a high sensitivity, efficiency and robustness. This distinctive technique can provide dynamic temporal imaging of ultrafast signals, leading to potential applications including single-pixel hyperspectral imaging, remote sensing, and high-data-rate optical communications.

Since both techniques are based on probe-beam encoding, the most straightforward future direction is combining them together to achieve single-pixel hyperspectral imaging. Two optical SLMs are required in the probe arm: one encodes the spatial degree of freedom while the other one encodes the temporal degree of freedom. After mixing the spatio-temporally modulated probe pulse with the THz pulse in the detection crystal, one can simply use a pair of balanced photodiode to perform the measurement since the photodiode is a 'single-pixel' detector in both spatial and temporal degree of freedom. A smart design is necessary to make sure the system can be operated efficiently so that the advantages of each technique can be inherited by the new single-pixel hyperspectral imaging.

Bibliography

[1] Yiyu Zhou, Jiapeng Zhao, Boris Braverman, Kai Pang, Runzhou Zhang, Alan E Willner, Zhimin Shi, and Robert W Boyd. Multiprobe time reversal for high-fidelity vortex-mode-division multiplexing over a turbulent free-space link. *Physical Review Applied*, 15(3):034011, 2021.

[2] Yiyu Zhou, Boris Braverman, Alexander Fyffe, Runzhou Zhang, Jiapeng Zhao, Alan E Willner, Zhimin Shi, and Robert W Boyd. High-fidelity spatial mode transmission through a 1-km-long multimode fiber via vectorial time reversal. *Nature communications*, 12(1):1–7, 2021.

[3] **Jiapeng Zhao**, Jianming Dai, Boris Braverman, Xi-Cheng Zhang, and Robert W Boyd. Single-pixel temporal imaging. *under review, arXiv preprint arXiv:2009.13693*, 2020.

[4] **Jiapeng Zhao**, Yiyu Zhou, Boris Braverman, Cong Liu, Kai Pang, Nicholas K Steinhoff, Glenn A Tyler, Alan E Willner, and Robert W Boyd. Performance of real-time adaptive optics compensation in a turbulent channel with high-dimensional spatial-mode encoding. *Optics Express*, 28(10):15376–15391, 2020.

[5] Fumin Wang, Pei Zeng, **Jiapeng Zhao**, Boris Braverman, Yiyu Zhou, Mohammad Mirhosseini, Xiaoli Wang, Hong Gao, Fuli Li, Robert W Boyd, et al. High-dimensional quantum key distribution based on mutually partially unbiased bases. *Physical Review A*, 101(3):032340, 2020.

[6] **Jiapeng Zhao**, Mohammad Mirhosseini, Boris Braverman, Yiyu Zhou, Seyed Mohammad Hashemi Rafsanjani, Yongxiong Ren, Nicholas K Steinhoff, Glenn A Tyler, Alan E Willner, and Robert W

Boyd. Performance analysis of d-dimensional quantum cryptography under state-dependent diffraction. *Physical Review A*, 100(3):032319, 2019.

[7] **Jiapeng Zhao**, E Yiwen, Kaia Williams, Xi-Cheng Zhang, and Robert W Boyd. Spatial sampling of terahertz fields with sub-wavelength accuracy via probe-beam encoding. *Light: Science & Applications*, 8(1):1–8, 2019.

[8] Yiyu Zhou, Mohammad Mirhosseini, Stone Oliver, Jiapeng Zhao, Seyed Mohammad Hashemi Rafsanjani, Martin PJ Lavery, Alan E Willner, and Robert W Boyd. Using all transverse degrees of freedom in quantum communications based on a generic mode sorter. *Optics Express*, 27(7):10383–10394, 2019.

[9] Cong Liu, Kai Pang, Zhe Zhao, Peicheng Liao, Runzhou Zhang, Hao-qian Song, Yinwen Cao, Jing Du, Long Li, Hao Song, Yongxiong Ren, Guodong Xie, Yifan Zhao, Jiapeng Zhao, Seyed M. H. Rafsanjani, Ari N. Willner, Jeffrey H. Shapiro, Robert W. Boyd, Moshe Tur, and Alan E. Willner. Single-end adaptive optics compensation for emulated turbulence in a bi-directional 10-Mbit/s per channel free-space quantum communication link using orbital-angular-momentum encoding. *Research*, 2019:8326701, 2019.

[10] Cong Liu, Yongxiong Ren, **Jiapeng Zhao**, Mohammad Mirhosseini, Seyed Mohammad Hashemi Rafsanjani, Guodong Xie, Kai Pang, Hao-qian Song, Zhe Zhao, Zhe Wang, et al. Switchable detector array scheme to reduce the effect of single-photon detector's deadtime in a multi-bit/photon quantum link. *Opitcs Communications*, 441:132–137, 2019.

[11] Yiyu Zhou, **Jiapeng Zhao**, Zhimin Shi, Seyed Mohammad Hashemi Rafsanjani, Mohammad Mirhosseini, Ziyi Zhu, Alan E Willner, and Robert W Boyd. Hermite–gaussian mode sorter. *Optics Letters*, 43(21):5263–5266, 2018.

[12] Dongzhi Fu, Yiyu Zhou, Rui Qi, Stone Oliver, Yunlong Wang, Seyed Mohammad Hashemi Rafsanjani, **Jiapeng Zhao**, Mohammad Mirhosseini, Zhimin Shi, Pei Zhang, et al. Realization of a scalable laguerre–

gaussian mode sorter based on a robust radial mode sorter. *Optics Express*, 26(25):33057–33065, 2018.

[13] Kai Pang, Cong Liu, Guodong Xie, Yongxiong Ren, Zhe Zhao, Runzhou Zhang, Yinwen Cao, **Jiapeng Zhao**, Haoqian Song, Hao Song, et al. Demonstration of a 10 mbit/s quantum communication link by encoding data on two laguerre–gaussian modes with different radial indices. *Optics Letters*, 43(22):5639–5642, 2018.

[14] Yiyu Zhou, Mohammad Mirhosseini, Dongzhi Fu, **Jiapeng Zhao**, Seyed Mohammad Hashemi Rafsanjani, Alan E Willner, and Robert W Boyd. Sorting photons by radial quantum number. *Physical Review Letters*, 119(26):263602, 2017.

[15] Yongxiong Ren, Cong Liu, Kai Pang, Jiapeng Zhao, Yinwen Cao, Guodong Xie, Long Li, Peicheng Liao, Zhe Zhao, Moshe Tur, Robert W. Boyd, and Alan E. Willner. Spatially multiplexed orbital-angular-momentum-encoded single photon and classical channels in a free-space optical communication link. *Optics Letters*, 42(23):4881–4884, 2017.

[16] Lu Gao, Seyed Mohammad Hashemi Rafsanjani, Yiyu Zhou, Zhe Yang, Omar S Magaña-Loaiza, Mohammad Mirhosseini, **Jiapeng Zhao**, Boshen Gao, and Robert W Boyd. Distributed angular double-slit interference with pseudo-thermal light. *Applied Physics Letters*, 110(7):071107, 2017.

[17] **Jiapeng Zhao**, E Yiwen, Kaia Williams, X-C Zhang, and Robert W Boyd. Spatial sampling of terahertz fields with subwavelength accuracy via probe beam encoding. In *Terahertz, RF, Millimeter, and Submillimeter-Wave Technology and Applications XIII*, volume 11279, page 112790I. International Society for Optics and Photonics, 2020.

[18] **Jiapeng Zhao**, Yiyu Zhou, Boris Braverman, Cong Liu, Kai Pang, Nicholas K Steinhoff, Glenn A Tyler, Alan E Willner, and Robert Boyd. Investigate the performance of real-time adaptive optics correction in a turbulent high-dimensional quantum communication channel. In *Free-Space Laser Communications XXXII*, volume 11272, page 112721C. International Society for Optics and Photonics, 2020.

[19] Yiyu Zhou, Boris Braverman, Alexander Fyffe, Runzhou Zhang, **Jiapeng Zhao**, Alan E Willner, Zhimin Shi, and Robert W Boyd. Vectorial phase conjugation for high-fidelity mode transmission through multimode fiber. In *Photonic Networks and Devices*, pages NeW2B–5. Optical Society of America, 2020.

[20] Cong Liu, Kai Pang, **Jiapeng Zhao**, Long Li, Yifan Zhao, Jing Du, Yongxiong Ren, Guodong Xie, Zhe Zhao, Haoqian Song, et al. Demonstration of single-end adaptive optics compensation for emulated turbulence in a bi-directional 10-mbits/s per channel free-space quantum communication link using orbital-angular-momentum encoding. In *CLEO: QELS_Fundamental Science*, pages JTh5B–2. Optical Society of America, 2018.

[21] Yiyu Zhou, Mohammad Mirhosseini, Dongzhi Fu, **Jiapeng Zhao**, Seyed Mohammad Hashemi Rafsanjani, Alan E Willner, and Robert W Boyd. Sorting laguerre-gaussian modes by radial quantum number. In *CLEO: Applications and Technology*, pages JTh2A–4. Optical Society of America, 2018.

[22] **Jiapeng Zhao**, Mohammad Mirhosseini, Yiyu Zhou, Seyed Mohammad Hashemi Rafsanjani, Yongxiong Ren, Nicholas K Steinhoff, Glen A Tyler, Alan E Willner, and Robert W Boyd. Performance analysis of d-dimensional quantum cryptography with mode-dependent diffraction. In *CLEO: Science and Innovations*, pages JTh2A–19. Optical Society of America, 2018.

[23] Kai Pang, Cong Liu, Guodong Xie, Yongxiong Ren, Zhe Zhao, Runzhou Zhang, Yinwen Cao, **Jiapeng Zhao**, Long Li, Haoqian Song, et al. Experimental demonstration of a 10-mbit/s quantum link using data encoding on orthogonal laguerre-gaussian modes. In *CLEO: QELS_Fundamental Science*, pages FTu3G–4. Optical Society of America, 2018.

[24] Cong Liu, Kai Pang, Hao Song, Guodong Xie, **Jiapeng Zhao**, Yongxiong Ren, Haoqian Song, Zhe Zhao, Runzhou Zhang, Long Li, et al. Experimental demonstration of a 20-mbit/s per channel free-space bi-directional quantum communication link using orbital-angular-momentum encoding and multi-port mode converters. In

CLEO: Applications and Technology, pages JTh2A–15. Optical Society of America, 2018.

[25] Cong Liu, Kai Pang, Yongxiong Ren, **Jiapeng Zhao**, Guodong Xie, Yinwen Cao, Hao Song, Zhe Zhao, Haoqian Song, Long Li, et al. Demonstration of adaptive optics compensation for emulated atmospheric turbulence in a two-orbital-angular-momentum encoded free-space quantum link at 10 mbits/s. In *CLEO: QELS_Fundamental Science*, pages FW4F–5. Optical Society of America, 2018.

[26] Yongxiong Ren, Cong Liu, Kai Pang, **Jiapeng Zhao**, Yinwen Cao, Guodong Xie, Long Li, Zhe Zhao, Zhe Wang, Moshe Tur, et al. Experimental demonstration of an orbital-angular-momentum encoded quantum communication link co-propagating with a classical channel. In *CLEO: Science and Innovations*, pages SW4I–4. Optical Society of America, 2017.

[27] Cong Liu, Yongxiong Ren, **Jiapeng Zhao**, Seyed Mohammad Hashemi Rafsanjani, Guodong Xie, Kai Pang, Haoqian Song, Zhe Zhao, Zhe Wang, Long Li, et al. Reduced effect of single-photon-detector deadtime using a switchable detector array in an orbital-angular-momentum (oam) encoded quantum system. In *CLEO: QELS_Fundamental Science*, pages FF1E–4. Optical Society of America, 2017.

[28] Lu Gao, **Jiapeng Zhao**, Omar S Magaña-Loaiza, Seyed Mohammad Hashemi Rafsanjani, Mohammad Mirhosseini, Yiyu Zhou, and RW Boyd. Non-local angular double-slit ghost diffraction with thermal light. In *Laser Science*, pages JTh2A–14. Optical Society of America, 2016.

[29] John Henry Poynting. The wave motion of a revolving shaft, and a suggestion as to the angular momentum in a beam of circularly polarised light. *Proceedings of the Royal Society of London. Series A, Containing Papers of a Mathematical and Physical Character*, 82(557):560–567, 1909.

[30] Greg Gbur. *Singular optics.* CRC Press, 2016.

[31] Alipasha Vaziri, Gregor Weihs, and Anton Zeilinger. Experimental two-photon, three-dimensional entanglement for quantum communication. *Physical Review Letters*, 89(24):240401, 2002.

[32] Alois Mair, Alipasha Vaziri, Gregor Weihs, and Anton Zeilinger. Entanglement of the orbital angular momentum states of photons. *Nature*, 412(6844):313–316, 2001.

[33] Alipasha Vaziri, Jian-Wei Pan, Thomas Jennewein, Gregor Weihs, and Anton Zeilinger. Concentration of higher dimensional entanglement: qutrits of photon orbital angular momentum. *Physical review letters*, 91(22):227902, 2003.

[34] Alison M Yao and Miles J Padgett. Orbital angular momentum: origins, behavior and applications. *Advances in Optics and Photonics*, 3(2):161–204, 2011.

[35] Jian Wang, Jeng-Yuan Yang, Irfan M Fazal, Nisar Ahmed, Yan Yan, Hao Huang, Yongxiong Ren, Yang Yue, Samuel Dolinar, Moshe Tur, and Alan E. Willner. Terabit free-space data transmission employing orbital angular momentum multiplexing. *Nature Photonics*, 6(7):488, 2012.

[36] Mohammad Mirhosseini, Omar S Magaña-Loaiza, Changchen Chen, Seyed Mohammad Hashemi Rafsanjani, and Robert W Boyd. Wigner distribution of twisted photons. *Physical review letters*, 116(13):130402, 2016.

[37] Omar S Magaña-Loaiza, Mohammad Mirhosseini, Robert M Cross, Seyed Mohammad Hashemi Rafsanjani, and Robert W Boyd. Hanbury brown and twiss interferometry with twisted light. *Science advances*, 2(4):e1501143, 2016.

[38] Yongxiong Ren, Zhe Wang, Peicheng Liao, Long Li, Guodong Xie, Hao Huang, Zhe Zhao, Yan Yan, Nisar Ahmed, Asher Willner, Martin P. J. Lavery, Nima Ashrafi, Solyman Ashrafi, Robert Bock, Moshe Tur, Ivan B. Djordjevic, Mark A. Neifeld, and Alan E. Willner. Experimental characterization of a 400 Gbit/s orbital angular momentum multiplexed free-space optical link over 120 m. *Optics Letters*, 41(3):622–625, 2016.

[39] Guodong Xie, Haoqian Song, Zhe Zhao, Giovanni Milione, Yongxiong Ren, Cong Liu, Runzhou Zhang, Changjing Bao, Long Li, Zhe Wang,

et al. Using a complex optical orbital-angular-momentum spectrum to measure object parameters. *Optics letters*, 42(21):4482–4485, 2017.

[40] Daniele Cozzolino, Davide Bacco, Beatrice Da Lio, Kasper Ingerslev, Yunhong Ding, Kjeld Dalgaard, Poul Kristensen, Michael Galili, Karsten Rottwitt, Siddharth Ramachandran, and Leif Katsuo Oxenløwe. Orbital angular momentum states enabling fiber-based high-dimensional quantum communication. *Physical Review Applied*, 11(6):064058, 2019.

[41] Nenad Bozinovic, Yang Yue, Yongxiong Ren, Moshe Tur, Poul Kristensen, Hao Huang, Alan E Willner, and Siddharth Ramachandran. Terabit-scale orbital angular momentum mode division multiplexing in fibers. *science*, 340(6140):1545–1548, 2013.

[42] Siddharth Ramachandran and Poul Kristensen. Optical vortices in fiber. *Nanophotonics*, 2(5-6):455–474, 2013.

[43] P Gregg, P Kristensen, and S Ramachandran. Conservation of orbital angular momentum in air-core optical fibers. *Optica*, 2(3):267–270, 2015.

[44] Dirk E Boonzajer Flaes, Jan Stopka, Sergey Turtaev, Johannes F de Boer, Tomáš Tyc, and Tomáš Čižmár. Robustness of light-transport processes to bending deformations in graded-index multimode waveguides. *Physical Review Letters*, 120(23):233901, 2018.

[45] Claude E Shannon. A mathematical theory of communication. *The Bell system technical journal*, 27(3):379–423, 1948.

[46] Richard P Feynman. Simulating physics with computers. *Int. J. Theor. Phys*, 21(6/7), 1982.

[47] Nicolas Gisin, Grégoire Ribordy, Wolfgang Tittel, and Hugo Zbinden. Quantum cryptography. *Reviews of Modern Physics*, 74(1):145, 2002.

[48] Valerio Scarani, Helle Bechmann-Pasquinucci, Nicolas J Cerf, Miloslav Dušek, Norbert Lütkenhaus, and Momtchil Peev. The security of practical quantum key distribution. *Reviews of Modern Physics*, 81(3):1301, 2009.

[49] Hoi-Kwong Lo, M. Curty, and K. Tamaki. Secure quantum key distribution. *Nature Photonics*, 8(8):595, 2014.

[50] C. H. Bennett and G. Brassard. Quantum cryptography: public key distribution and coin tossing. *Proceedings of the IEEE International, Conference on Computers, Systems and Signal Processing*, pages 175–179, 1984.

[51] William K Wootters and Wojciech H Zurek. A single quantum cannot be cloned. *Nature*, 299(5886):802–803, 1982.

[52] Mohammad Mirhosseini, Omar S Magaña-Loaiza, Malcolm N O'Sullivan, Brandon Rodenburg, Mehul Malik, Martin PJ Lavery, Miles J Padgett, Daniel J Gauthier, and Robert W Boyd. High-dimensional quantum cryptography with twisted light. *New Journal of Physics*, 17(3):033033, 2015.

[53] Lana Sheridan and Valerio Scarani. Security proof for quantum key distribution using qudit systems. *Physical Review A*, 82(3):030301, 2010.

[54] Kamil Brádler, Mohammad Mirhosseini, Robert Fickler, Anne Broadbent, and Robert W. Boyd. Finite-key security analysis for multilevel quantum key distribution. *New Journal of Physics*, 18(7):073030, 2016.

[55] Nicolas J Cerf, Mohamed Bourennane, Anders Karlsson, and Nicolas Gisin. Security of quantum key distribution using d-level systems. *Physical Review Letters*, 88(12):127902, 2002.

[56] Gabriel Molina-Terriza, Juan P Torres, and Lluis Torner. Management of the angular momentum of light: preparation of photons in multidimensional vector states of angular momentum. *Physical review letters*, 88(1):013601, 2001.

[57] Hoi-Kwong Lo, Xiongfeng Ma, and Kai Chen. Decoy state quantum key distribution. *Physical review letters*, 94(23):230504, 2005.

[58] Mohammad Mirhosseini, Omar S Magana-Loaiza, Changchen Chen, Brandon Rodenburg, Mehul Malik, and Robert W Boyd. Rapid generation of light beams carrying orbital angular momentum. *Optics Express*, 21(25):30196–30203, 2013.

[59] Jonathan Leach, Miles J Padgett, Stephen M Barnett, Sonja Franke-Arnold, and Johannes Courtial. Measuring the orbital angular momentum of a single photon. *Physical review letters*, 88(25):257901, 2002.

[60] Gregorius CG Berkhout, Martin PJ Lavery, Johannes Courtial, Marco W Beijersbergen, and Miles J Padgett. Efficient sorting of orbital angular momentum states of light. *Physical review letters*, 105(15):153601, 2010.

[61] Mohammad Mirhosseini, Mehul Malik, Zhimin Shi, and Robert W Boyd. Efficient separation of the orbital angular momentum eigenstates of light. *Nature Communications*, 4:2781, 2013.

[62] Martin PJ Lavery, David J Robertson, Gregorius CG Berkhout, Gordon D Love, Miles J Padgett, and Johannes Courtial. Refractive elements for the measurement of the orbital angular momentum of a single photon. *Optics express*, 20(3):2110–2115, 2012.

[63] Chenhao Wan, Jian Chen, and Qiwen Zhan. Compact and high-resolution optical orbital angular momentum sorter. *APL Photonics*, 2(3):031302, 2017.

[64] Glenn A Tyler. Spatial bandwidth considerations for optical communication through a free space propagation link. *Optics Letters*, 36(23):4650–4652, 2011.

[65] David AB Miller. Communicating with waves between volumes: evaluating orthogonal spatial channels and limits on coupling strengths. *Applied Optics*, 39(11):1681–1699, 2000.

[66] Glenn A Tyler. Adaptive optics compensation for propagation through deep turbulence: a study of some interesting approaches. *Optical Engineering*, 52(2):021011, 2012.

[67] Glenn A Tyler, Paul Merritt, Robert Q Fugate, and Terry J Brennan. Adaptive opitcs: Theory and applications. *The Optical Science Company*, 2006.

[68] Glenn A Tyler, Jeffery L Vaughn, and Nicholas K Steinhoff. High-capacity, free-space quantum key distribution based on spatial and polarization encoding: Atmospheric considerations interim review. *The Optical Science Company*, 2017.

[69] Larry C Andrews and Ronald L Phillips. *Laser beam propagation through random media*, volume 152. SPIE, 2005.

[70] Andrey Nikolaevich Kolmogorov. The local structure of turbulence in incompressible viscous fluid for very large reynolds numbers. *Cr Acad. Sci. URSS*, 30:301–305, 1941.

[71] David L Fried. Statistics of a geometric representation of wavefront distortion. *JOSA*, 55(11):1427–1435, 1965.

[72] Carl Paterson. Atmospheric turbulence and orbital angular momentum of single photons for optical communication. *Physical review letters*, 94(15):153901, 2005.

[73] Glenn A Tyler and Robert W Boyd. Influence of atmospheric turbulence on the propagation of quantum states of light carrying orbital angular momentum. *Optics Letters*, 34(2):142–144, 2009.

[74] Mehul Malik, Malcolm O'Sullivan, Brandon Rodenburg, Mohammad Mirhosseini, Jonathan Leach, Martin PJ Lavery, Miles J Padgett, and Robert W Boyd. Influence of atmospheric turbulence on optical communications using orbital angular momentum for encoding. *Optics express*, 20(12):13195–13200, 2012.

[75] Robert W Boyd, Brandon Rodenburg, Mohammad Mirhosseini, and Stephen M Barnett. Influence of atmospheric turbulence on the propagation of quantum states of light using plane-wave encoding. *Optics express*, 19(19):18310–18317, 2011.

[76] Brandon Rodenburg, Martin PJ Lavery, Mehul Malik, Malcolm N O'Sullivan, Mohammad Mirhosseini, David J Robertson, Miles Padgett, and Robert W Boyd. Influence of atmospheric turbulence on states of light carrying orbital angular momentum. *Optics letters*, 37(17):3735–3737, 2012.

[77] Yongxiong Ren, Hao Huang, Guodong Xie, Nisar Ahmed, Yan Yan, Baris I Erkmen, Nivedita Chandrasekaran, Martin PJ Lavery, Nicholas K Steinhoff, Moshe Tur, Samuel Dolinar, Mark Neifeld, Miles J. Padgett, Robert W. Boyd, Jeffrey H. Shapiro, and Alan E. Willner. Atmospheric turbulence effects on the performance of a free

space optical link employing orbital angular momentum multiplexing. *Optics Letters*, 38(20):4062–4065, 2013.

[78] Brandon Rodenburg, Mohammad Mirhosseini, Mehul Malik, Omar S Magaña-Loaiza, Michael Yanakas, Laura Maher, Nicholas K Steinhoff, Glenn A Tyler, and Robert W Boyd. Simulating thick atmospheric turbulence in the lab with application to orbital angular momentum communication. *New Journal of Physics*, 16(3):033020, 2014.

[79] Mohammad Mirhosseini, Brandon Rodenburg, Mehul Malik, and Robert W Boyd. Free-space communication through turbulence: a comparison of plane-wave and orbital-angular-momentum encodings. *Journal of Modern Optics*, 61(1):43–48, 2014.

[80] Mario Krenn, Johannes Handsteiner, Matthias Fink, Robert Fickler, Rupert Ursin, Mehul Malik, and Anton Zeilinger. Twisted light transmission over 143 km. *Proceedings of the National Academy of Sciences*, 113(48):13648–13653, 2016.

[81] Martin PJ Lavery, Christian Peuntinger, Kevin Günthner, Peter Banzer, Dominique Elser, Robert W Boyd, Miles J Padgett, Christoph Marquardt, and Gerd Leuchs. Free-space propagation of high-dimensional structured optical fields in an urban environment. *Science Advances*, 3(10):e1700552, 2017.

[82] Yongxiong Ren, Guodong Xie, Hao Huang, Nisar Ahmed, Yan Yan, Long Li, Changjing Bao, Martin PJ Lavery, Moshe Tur, Mark A Neifeld, Robert W. Boyd, Jeffrey H. Shapiro, and Alan E. Willner. Adaptive-optics-based simultaneous pre-and post-turbulence compensation of multiple orbital-angular-momentum beams in a bidirectional free-space optical link. *Optica*, 1(6):376–382, 2014.

[83] Long Li, Runzhou Zhang, Zhe Zhao, Guodong Xie, Peicheng Liao, Kai Pang, Haoqian Song, Cong Liu, Yongxiong Ren, Guillaume Labroille, et al. High-capacity free-space optical communications between a ground transmitter and a ground receiver via a uav using multiplexing of multiple orbital-angular-momentum beams. *Scientific reports*, 7(1):1–12, 2017.

[84] Mitchell A Cox, Nokwazi Mphuthi, Isaac Nape, Nikiwe Mashaba, Ling Cheng, and Andrew Forbes. Structured light in turbulence. *IEEE Journal of Selected Topics in Quantum Electronics*, 27(2):1–21, 2020.

[85] Miles J Padgett, Filippo M Miatto, Martin PJ Lavery, Anton Zeilinger, and Robert W Boyd. Divergence of an orbital-angular-momentum-carrying beam upon propagation. *New Journal of Physics*, 17(2):023011, 2015.

[86] Giuseppe Vallone, Vincenzo D'Ambrosio, Anna Sponselli, Sergei Slussarenko, Lorenzo Marrucci, Fabio Sciarrino, and Paolo Villoresi. Free-space quantum key distribution by rotation-invariant twisted photons. *Physical Review Letters*, 113(6):060503, 2014.

[87] Alicia Sit, Frédéric Bouchard, Robert Fickler, Jérémie Gagnon-Bischoff, Hugo Larocque, Khabat Heshami, Dominique Elser, Christian Peuntinger, Kevin Günthner, Bettina Heim, Christoph Marquardt, Gerd Leuchs, Robert W. Boyd, and Ebrahim Karimi. High-dimensional intracity quantum cryptography with structured photons. *Optica*, 4(9):1006–1010, 2017.

[88] Patrick J Coles, Mario Berta, Marco Tomamichel, and Stephanie Wehner. Entropic uncertainty relations and their applications. *Reviews of Modern Physics*, 89(1):015002, 2017.

[89] Lars Lydersen, Carlos Wiechers, Christoffer Wittmann, Dominique Elser, Johannes Skaar, and Vadim Makarov. Hacking commercial quantum cryptography systems by tailored bright illumination. *Nature photonics*, 4(10):686–689, 2010.

[90] Shihan Sajeed, Poompong Chaiwongkhot, Jean-Philippe Bourgoin, Thomas Jennewein, Norbert Lütkenhaus, and Vadim Makarov. Security loophole in free-space quantum key distribution due to spatial-mode detector-efficiency mismatch. *Physical Review A*, 91(6):062301, 2015.

[91] Adam Winick, Norbert Lütkenhaus, and Patrick J Coles. Reliable numerical key rates for quantum key distribution. *Quantum*, 2:77, 2018.

[92] Hoi-Kwong Lo, Marcos Curty, and Bing Qi. Measurement-device-independent quantum key distribution. *Physical review letters*, 108(13):130503, 2012.

[93] Samuel L Braunstein and Stefano Pirandola. Side-channel-free quantum key distribution. *Physical review letters*, 108(13):130502, 2012.

[94] Stefano Pirandola, Carlo Ottaviani, Gaetana Spedalieri, Christian Weedbrook, Samuel L Braunstein, Seth Lloyd, Tobias Gehring, Christian S Jacobsen, and Ulrik L Andersen. High-rate measurement-device-independent quantum cryptography. *Nature Photonics*, 9(6):397–402, 2015.

[95] Tobias Schmitt-Manderbach, Henning Weier, Martin Fürst, Rupert Ursin, Felix Tiefenbacher, Thomas Scheidl, Josep Perdigues, Zoran Sodnik, Christian Kurtsiefer, John G Rarity, et al. Experimental demonstration of free-space decoy-state quantum key distribution over 144 km. *Physical Review Letters*, 98(1):010504, 2007.

[96] Sheng-Kai Liao, Wen-Qi Cai, Wei-Yue Liu, Liang Zhang, Yang Li, Ji-Gang Ren, Juan Yin, Qi Shen, Yuan Cao, Zheng-Ping Li, Feng-Zhi Li, Xia-Wei Chen, Li-Hua Sun, Jian-Jun Jia, Jin-Cai Wu, Xiao-Jun Jiang, Jian-Feng Wang, Yong-Mei Huang, Qiang Wang, Yi-Lin Zhou, Lei Deng, Tao Xi, Lu Ma, Tai Hu, Qiang Zhang, Yu-Ao Chen, Nai-Le Liu, Xiang-Bin Wang, Zhen-Cai Zhu, Chao-Yang Lu, Rong Shu, Cheng-Zhi Peng, Jian-Yu Wang, and Jian-Wei Pan. Satellite-to-ground quantum key distribution. *Nature*, 549(7670):43, 2017.

[97] Yingwen Zhang, Shashi Prabhakar, Alpha Hamadou Ibrahim, Filippus S Roux, Andrew Forbes, and Thomass Konrad. Experimentally observed decay of high-dimensional entanglement through turbulence. *Physical Review A*, 94(3):032310, 2016.

[98] Frédéric Bouchard, Alicia Sit, Felix Hufnagel, Aazad Abbas, Yingwen Zhang, Khabat Heshami, Robert Fickler, Christoph Marquardt, Gerd Leuchs, Robert W. Boyd, and Ebrahim Karimi. Quantum cryptography with twisted photons through an outdoor underwater channel. *Optics Express*, 26(17):22563–22573, 2018.

[99] Nina Leonhard, Giacomo Sorelli, Vyacheslav N Shatokhin, Claudia Reinlein, and Andreas Buchleitner. Protecting the entanglement of twisted photons by adaptive optics. *Physical Review A*, 97(1):012321, 2018.

[100] Giacomo Sorelli, Nina Leonhard, Vyacheslav N Shatokhin, Claudia Reinlein, and Andreas Buchleitner. Entanglement protection of high-dimensional states by adaptive optics. *New Journal of Physics*, 21(2):023003, 2019.

[101] Shicheng Zhao, Wendong Li, Yuan Shen, YongHe Yu, XinHong Han, Hao Zeng, Maoqi Cai, Tian Qian, Shuo Wang, Zhaoming Wang, Ya Xiao, and Yongjian Gu. Experimental investigation of quantum key distribution over a water channel. *Applied Optics*, 58(14):3902–3907, 2019.

[102] Felix Hufnagel, Alicia Sit, Florence Grenapin, Frédéric Bouchard, Khabat Heshami, Duncan England, Yingwen Zhang, Benjamin J Sussman, Robert W Boyd, Gerd Leuchs, and Ebrahim Karimi. Characterization of an underwater channel for quantum communications in the Ottawa river. *Optics Express*, 27(19):26346–26354, 2019.

[103] Long Li, Runzhou Zhang, Peicheng Liao, Yinwen Cao, Haoqian Song, Yifan Zhao, Jing Du, Zhe Zhao, Cong Liu, Kai Pang, Hao Song, Ahmed Almaiman, Dmitry Starodubov, Brittany Lynn, Robert Bock, Moshe Tur, Andreas F. Molisch, and Alan E. Willner. Mitigation for turbulence effects in a 40-gbit/s orbital-angular-momentum-multiplexed free-space optical link between a ground station and a retro-reflecting uav using mimo equalization. *Optics letters*, 44(21):5181–5184, 2019.

[104] Chemist M Mabena and Filippus S Roux. Quantum channel correction with twisted light using compressive sensing. *Physical Review A*, 101(1):013807, 2020.

[105] Antonio Acín, Daniel Cavalcanti, Elsa Passaro, Stefano Pironio, and Paul Skrzypczyk. Necessary detection efficiencies for secure quantum key distribution and bound randomness. *Physical Review A*, 93(1):012319, 2016.

[106] Martin PJ Lavery. Vortex instability in turbulent free-space propagation. *New Journal of Physics*, 20(4):043023, 2018.

[107] NJ Woolf, J Roger P Angel, and JT Williams. Options for a new arizona observatory: Configurations, costs and site. In *International Astronomical Union Colloquium*, volume 79, pages 831–843. Cambridge University, 1984.

[108] Jacques M Beckers. Adaptive optics for astronomy: principles, performance, and applications. *Annual review of astronomy and astrophysics*, 31(1):13–62, 1993.

[109] François Roddier. *Adaptive optics in astronomy*. Cambridge University, 1999.

[110] David L Fried. Optical resolution through a randomly inhomogeneous medium for very long and very short exposures. *JOSA*, 56(10):1372–1379, 1966.

[111] Darryl P Greenwood. Bandwidth specification for adaptive optics systems. *JOSA*, 67(3):390–393, 1977.

[112] David L Fried. Greenwood frequency measurements. *JOSA A*, 7(5):946–947, 1990.

[113] Glenn A Tyler. Bandwidth considerations for tracking through turbulence. *JOSA A*, 11(1):358–367, 1994.

[114] Robert K Tyson and Benjamin W Frazier. *Field guide to adaptive optics*. SPIE, 2012.

[115] Wei Liu, Kainan Yao, Danian Huang, Xudong Lin, Liang Wang, and Yaowen Lv. Performance evaluation of coherent free space optical communications with a double-stage fast-steering-mirror adaptive optics system depending on the greenwood frequency. *Optics Express*, 24(12):13288–13302, 2016.

[116] Radu Ionicioiu. Sorting quantum systems efficiently. *Scientific Reports*, 6:25356, 2016.

[117] Nicolas K Fontaine, Roland Ryf, Haoshuo Chen, David T Neilson, Kwangwoong Kim, and Joel Carpenter. Laguerre-Gaussian mode sorter. *Nature communications*, 10(1):1865, 2019.

[118] Bienvenu Ndagano, Isaac Nape, Benjamin Perez-Garcia, Stirling Scholes, Raul I Hernandez-Aranda, Thomas Konrad, Martin PJ Lavery, and Andrew Forbes. A deterministic detector for vector vortex states. *Scientific reports*, 7(1):1–8, 2017.

[119] Fabio Alves, Dragoslav Grbovic, Brian Kearney, and Gamani Karunasiri. Microelectromechanical systems bimaterial terahertz sensor with integrated metamaterial absorber. *Optics letters*, 37(11):1886–1888, 2012.

[120] Fabio Alves, Dragoslav Grbovic, Brian Kearney, Nickolay V Lavrik, and Gamani Karunasiri. Bi-material terahertz sensors using metamaterial structures. *Optics express*, 21(11):13256–13271, 2013.

[121] Qi Wu and X-C Zhang. Free-space electro-optic sampling of terahertz beams. *Applied Physics Letters*, 67(24):3523–3525, 1995.

[122] Xi-Cheng Zhang and Jingzhou Xu. *Introduction to THz wave photonics*, volume 29. Springer, 2010.

[123] Yun-Shik Lee. *Principles of terahertz science and technology*, volume 170. Springer Science & Business Media, 2009.

[124] Robert W Boyd. *Nonlinear optics*. Academic press, 2020.

[125] Zhiping Jiang and X-C Zhang. 2d measurement and spatio-temporal coupling of few-cycle thz pulses. *Optics express*, 5(11):243–248, 1999.

[126] F Blanchard, A Doi, T Tanaka, and K Tanaka. Real-time, subwavelength terahertz imaging. *Annual Review of Materials Research*, 43:237–259, 2013.

[127] Jeremy Pearce, Hyeokho Choi, Daniel M Mittleman, Jeff White, and David Zimdars. Terahertz wide aperture reflection tomography. *Optics letters*, 30(13):1653–1655, 2005.

[128] Aparajita Bandyopadhyay, Andrei Stepanov, Brian Schulkin, Michael D Federici, Amartya Sengupta, Dale Gary, John F Federici, Robert Barat, Zoi-Heleni Michalopoulou, and David Zimdars. Terahertz interferometric and synthetic aperture imaging. *JOSA A*, 23(5):1168–1178, 2006.

[129] Jingzhou Xu and X-C Zhang. Terahertz wave reciprocal imaging. *Applied physics letters*, 88(15):151107, 2006.

[130] Stephanie M Teo, Benjamin K Ofori-Okai, Christopher A Werley, and Keith A Nelson. Invited article: Single-shot thz detection techniques optimized for multidimensional thz spectroscopy. *Review of Scientific Instruments*, 86(5):051301, 2015.

[131] Takeshi Yasui, Eisuke Saneyoshi, and Tsutomu Araki. Asynchronous optical sampling terahertz time-domain spectroscopy for ultrahigh spectral resolution and rapid data acquisition. *Applied Physics Letters*, 87(6):061101, 2005.

[132] A. Bartels, R. Cerna, C. Kistner, A. Thoma, F. Hudert, C. Janke, and T. Dekorsy. Ultrafast time-domain spectroscopy based on high-speed asynchronous optical sampling. *Review of Scientific Instruments*, 78(3):035107, 2007.

[133] Todd B Pittman, YH Shih, DV Strekalov, and Alexander V Sergienko. Optical imaging by means of two-photon quantum entanglement. *Physical Review A*, 52(5):R3429, 1995.

[134] DV Strekalov, AV Sergienko, DN Klyshko, and YH Shih. Observation of two-photon "ghost" interference and diffraction. *Physical review letters*, 74(18):3600, 1995.

[135] Ryan S Bennink, Sean J Bentley, and Robert W Boyd. "two-photon" coincidence imaging with a classical source. *Physical review letters*, 89(11):113601, 2002.

[136] Jeffrey H Shapiro. Computational ghost imaging. *Physical Review A*, 78(6):061802, 2008.

[137] Yaron Bromberg, Ori Katz, and Yaron Silberberg. Ghost imaging with a single detector. *Physical Review A*, 79(5):053840, 2009.

[138] Matthew P Edgar, Graham M Gibson, and Miles J Padgett. Principles and prospects for single-pixel imaging. *Nature Photonics*, 13(1):13–20, 2019.

[139] Graham M Gibson, Steven D Johnson, and Miles J Padgett. Single-pixel imaging 12 years on: a review. *Optics Express*, 28(19):28190–28208, 2020.

[140] Baoqing Sun, Matthew P Edgar, Richard Bowman, Liberty E Vittert, Stuart Welsh, A Bowman, and MJ Padgett. 3d computational imaging with single-pixel detectors. *Science*, 340(6134):844–847, 2013.

[141] Nam Huynh, Edward Zhang, Marta Betcke, Simon Arridge, Paul Beard, and Ben Cox. Single-pixel optical camera for video rate ultrasonic imaging. *Optica*, 3(1):26–29, 2016.

[142] Emmanuel J Candès and Michael B Wakin. An introduction to compressive sampling. *IEEE Signal Processing Magazine*, 25(2):21–30, 2008.

[143] Justin Romberg. Imaging via compressive sampling [introduction to compressive sampling and recovery via convex programming]. *IEEE Signal Processing Magazine*, 25(2):14–20, 2008.

[144] Emmanuel Candes and Justin Romberg. Sparsity and incoherence in compressive sampling. *Inverse problems*, 23(3):969, 2007.

[145] Martin Harwit. *Hadamard transform optics*. Elsevier, 2012.

[146] Wai Lam Chan, Kriti Charan, Dharmpal Takhar, Kevin F Kelly, Richard G Baraniuk, and Daniel M Mittleman. A single-pixel terahertz imaging system based on compressed sensing. *Applied Physics Letters*, 93(12):121105, 2008.

[147] Wai Lam Chan, Hou-Tong Chen, Antoinette J Taylor, Igal Brener, Michael J Cich, and Daniel M Mittleman. A spatial light modulator for terahertz beams. *Applied Physics Letters*, 94(21):213511, 2009.

[148] Claire M Watts, David Shrekenhamer, John Montoya, Guy Lipworth, John Hunt, Timothy Sleasman, Sanjay Krishna, David R Smith, and Willie J Padilla. Terahertz compressive imaging with metamaterial spatial light modulators. *Nature Photonics*, 8(8):605, 2014.

[149] David Shrekenhamer, Claire M Watts, and Willie J Padilla. Terahertz single pixel imaging with an optically controlled dynamic spatial light modulator. *Optics express*, 21(10):12507–12518, 2013.

[150] Rayko Ivanov Stantchev, Baoqing Sun, Sam M Hornett, Peter A Hobson, Graham M Gibson, Miles J Padgett, and Euan Hendry. Noninvasive, near-field terahertz imaging of hidden objects using a single-pixel detector. *Science advances*, 2(6):e1600190, 2016.

[151] Rayko Ivanov Stantchev, Xiao Yu, Thierry Blu, and Emma Pickwell-MacPherson. Real-time terahertz imaging with a single-pixel detector. *Nature Communications*, 11(1):1–8, 2020.

[152] Luana Olivieri, Juan S Totero Gongora, Alessia Pasquazi, and Marco Peccianti. Time-resolved nonlinear ghost imaging. *ACS Photonics*, 5(8):3379–3388, 2018.

[153] Xu Xie, Jingzhou Xu, and X-C Zhang. Terahertz wave generation and detection from a cdte crystal characterized by different excitation wavelengths. *Optics letters*, 31(7):978–980, 2006.

[154] Marek W Kowarz. Homogeneous and evanescent contributions in scalar near-field diffraction. *Applied Optics*, 34(17):3055–3063, 1995.

[155] Oleg Mitrofanov. Tetrahertz near-field electro-optic probe based on a microresonator. *Applied physics letters*, 88(9):091118, 2006.

[156] Tom Seifert, S Jaiswal, U Martens, J Hannegan, Lukas Braun, Pablo Maldonado, F Freimuth, A Kronenberg, J Henrizi, I Radu, et al. Efficient metallic spintronic emitters of ultrabroadband terahertz radiation. *Nature photonics*, 10(7):483–488, 2016.

[157] Matthew P Edgar, Graham M Gibson, Richard W Bowman, Baoqing Sun, Neal Radwell, Kevin J Mitchell, Stephen S Welsh, and Miles J Padgett. Simultaneous real-time visible and infrared video with single-pixel detectors. *Scientific reports*, 5:10669, 2015.

[158] Rayko I Stantchev, David B Phillips, Peter Hobson, Samuel M Hornett, Miles J Padgett, and Euan Hendry. Compressed sensing with near-field thz radiation. *Optica*, 4(8):989–992, 2017.

[159] Rayko I Stantchev, Jessica C Mansfield, Ryan S Edginton, Peter Hobson, Francesca Palombo, and Euan Hendry. Subwavelength hyperspectral thz studies of articular cartilage. *Scientific reports*, 8(1):6924, 2018.

[160] Q Chen, Z Jiang, and X-C Zhang. Electro-optic-based two-dimensional thz near-field imaging. In *Conference on Lasers and Electro-Optics*, page CThR3. Optical Society of America, 2000.

[161] Xinke Wang, Ye Cui, Wenfeng Sun, JiaSheng Ye, and Yan Zhang. Terahertz real-time imaging with balanced electro-optic detection. *Optics Communications*, 283(23):4626–4632, 2010.

[162] Daniel M Mittleman. Twenty years of terahertz imaging. *Optics express*, 26(8):9417–9431, 2018.

[163] Yoann Altmann, Stephen McLaughlin, Miles J Padgett, Vivek K Goyal, Alfred O Hero, and Daniele Faccio. Quantum-inspired computational imaging. *Science*, 361(6403):eaat2298, 2018.

[164] Si-Chao Chen, Liang-Hui Du, Kun Meng, Jiang Li, Zhao-Hui Zhai, Qi-Wu Shi, Ze-Ren Li, and Li-Guo Zhu. Terahertz wave near-field compressive imaging with a spatial resolution of over $\lambda/100$. *Optics Letters*, 44(1):21–24, 2019.

[165] Rick Trebino and Daniel J Kane. Using phase retrieval to measure the intensity and phase of ultrashort pulses: frequency-resolved optical gating. *Journal of the Optical Society of America A*, 10(5):1101–1111, 1993.

[166] Patrick O'shea, Mark Kimmel, Xun Gu, and Rick Trebino. Highly simplified device for ultrashort-pulse measurement. *Optics letters*, 26(12):932–934, 2001.

[167] Chris Iaconis and Ian A Walmsley. Spectral phase interferometry for direct electric-field reconstruction of ultrashort optical pulses. *Optics Letters*, 23(10):792–794, 1998.

[168] Brian H Kolner and Moshe Nazarathy. Temporal imaging with a time lens. *Optics Letters*, 14(12):630–632, 1989.

[169] Reza Salem, Mark A Foster, Amy C Turner, David F Geraghty, Michal Lipson, and Alexander L Gaeta. Optical time lens based on four-wave mixing on a silicon chip. *Optics Letters*, 33(10):1047–1049, 2008.

[170] Mark A Foster, Reza Salem, Yoshitomo Okawachi, Amy C Turner-Foster, Michal Lipson, and Alexander L Gaeta. Ultrafast waveform compression using a time-domain telescope. *Nature Photonics*, 3(10):581–585, 2009.

[171] H Dammann and K Görtler. High-efficiency in-line multiple imaging by means of multiple phase holograms. *Optics Communications*, 3(5):312–315, 1971.

[172] Damien Prongué, Hans-Peter Herzig, René Dändliker, and Michael T Gale. Optimized kinoform structures for highly efficient fan-out elements. *Applied Optics*, 31(26):5706–5711, 1992.

[173] Louis A Romero and Fred M Dickey. Theory of optimal beam splitting by phase gratings. i. one-dimensional gratings. *Journal of the Optical Society of America A*, 24(8):2280–2295, 2007.

[174] Chengbo Li. *Compressive sensing for 3D data processing tasks: applications, models and algorithms*. PhD thesis, Rice University, 2011.

[175] Tomohiro Shirai, Tero Setälä, and Ari T Friberg. Temporal ghost imaging with classical non-stationary pulsed light. *Journal of the Optical Society of America B*, 27(12):2549–2555, 2010.

[176] Piotr Ryczkowski, Margaux Barbier, Ari T Friberg, John M Dudley, and Goëry Genty. Ghost imaging in the time domain. *Nature Photonics*, 10(3):167–170, 2016.

[177] Fabrice Devaux, Paul-Antoine Moreau, Séverine Denis, and Eric Lantz. Computational temporal ghost imaging. *Optica*, 3(7):698–701, 2016.

[178] Yoshiki O-oka and Susumu Fukatsu. Differential ghost imaging in time domain. *Applied Physics Letters*, 111(6):061106, 2017.

[179] Piotr Ryczkowski, Margaux Barbier, Ari T Friberg, John M Dudley, and Goëry Genty. Magnified time-domain ghost imaging. *APL Photonics*, 2(4):046102, 2017.

[180] Yao-Kun Xu, Shi-Hai Sun, Wei-Tao Liu, Guang-Zhao Tang, Ji-Ying Liu, and Ping-Xing Chen. Detecting fast signals beyond bandwidth of detectors based on computational temporal ghost imaging. *Optics Express*, 26(1):99–107, 2018.

[181] Han Wu, Piotr Ryczkowski, Ari T Friberg, John M Dudley, and Goëry Genty. Temporal ghost imaging using wavelength conversion and two-color detection. *Optica*, 6(7):902–906, 2019.

[182] Yuan Tian, Hao Ge, Xiu-Juan Zhang, Xiang-Yuan Xu, Ming-Hui Lu, Yun Jing, and Yan-Feng Chen. Acoustic ghost imaging in the time domain. *Physical Review Applied*, 13(6):064044, 2020.

[183] Kosuke Murate, Mehraveh Javan Roshtkhari, Xavier Ropagnol, and François Blanchard. Adaptive spatiotemporal optical pulse front tilt using a digital micromirror deviceand its terahertz application. *Optics letters*, 43(9):2090–2093, 2018.

[184] Brian H Kolner. Space-time duality and the theory of temporal imaging. *IEEE Journal of Quantum Electronics*, 30(8):1951–1963, 1994.

[185] CV Bennett and BH Kolner. Upconversion time microscope demonstrating 103× magnification of femtosecond waveforms. *Optics Letters*, 24(11):783–785, 1999.

[186] Mark A Foster, Reza Salem, David F Geraghty, Amy C Turner-Foster, Michal Lipson, and Alexander L Gaeta. Silicon-chip-based ultrafast optical oscilloscope. *Nature*, 456(7218):81–84, 2008.

[187] Yoshitomo Okawachi, Reza Salem, Adrea R Johnson, Kasturi Saha, Jacob S Levy, Michal Lipson, and Alexander L Gaeta. Asynchronous single-shot characterization of high-repetition-rate ultrafast waveforms using a time-lens-based temporal magnifier. *Optics Letters*, 37(23):4892–4894, 2012.

[188] Alexey Tikan, Serge Bielawski, Christophe Szwaj, Stéphane Randoux, and Pierre Suret. Single-shot measurement of phase and amplitude by using a heterodyne time-lens system and ultrafast digital time-holography. *Nature Photonics*, 12(4):228–234, 2018.

[189] Ming-Jie Sun, Ling-Tong Meng, Matthew P Edgar, Miles J Padgett, and Neal Radwell. A russian dolls ordering of the hadamard basis for compressive single-pixel imaging. *Scientific reports*, 7(1):3464, 2017.

[190] Zhiping Jiang and X-C Zhang. Single-shot spatiotemporal terahertz field imaging. *Optics Letters*, 23(14):1114–1116, 1998.

[191] Jie Shan, Aniruddha S Weling, Ernst Knoesel, Ludwig Bartels, Mischa Bonn, Ajay Nahata, Georg A Reider, and Tony F Heinz. Single-shot measurement of terahertz electromagnetic pulses by use of electro-optic sampling. *Optics Letters*, 25(6):426–428, 2000.

[192] KY Kim, B Yellampalle, G Rodriguez, RD Averitt, AJ Taylor, and JH Glownia. Single-shot, interferometric, high-resolution, terahertz field diagnostic. *Applied Physics Letters*, 88(4):041123, 2006.

[193] KY Kim, B Yellampalle, AJ Taylor, G Rodriguez, and JH Glownia. Single-shot terahertz pulse characterization via two-dimensional electro-optic imaging with dual echelons. *Optics Letters*, 32(14):1968–1970, 2007.

[194] Yoichi Kawada, Takashi Yasuda, Atsushi Nakanishi, Koichiro Akiyama, and Hironori Takahashi. Single-shot terahertz spectroscopy using pulse-front tilting of an ultra-short probe pulse. *Optics Express*, 19(12):11228–11235, 2011.

[195] Shuiqin Zheng, Xinjian Pan, Yi Cai, Qinggang Lin, Ying Li, Shixiang Xu, Jingzhen Li, and Dianyuan Fan. Common-path spectral interferometry for single-shot terahertz electro-optics detection. *Optics Letters*, 42(21):4263–4266, 2017.